INVESTIGATION OF GENERATION MECHANISMS OF THE POST-MIDNIGHT F-REGION IRREGULARITIES

A synopsis submitted

in partial fulfillment for the award of the degree of

Doctor of Philosophy

by

Meenakshi S

SC19D022

Department of Physics
Indian Institute of Space Science and Technology
Thiruvananthapuram, India

January 2023

ii

Declaration

I declare that the thesis entitled "**INVESTIGATION OF GENERATION MECHANISMS OF THE POST-MIDNIGHT F-REGION IRREGULARITIES**" submitted in partial fulfillment of the degree of Doctor of Philosophy is a record of original work carried out by me under the supervision of Dr. S Sridharan and Dr. J Solomon Ivan, has not formed the basis for the award of any other degree or diploma, in this or any other Institution or University. In keeping with the ethical practice in reporting scientific information, due acknowledgments have been made wherever the findings of others have been cited.

Thiruvananthapuram-695547
19-12-2022

Meenakshi S
(SC19D022)

Acknowledgements

First and foremost I would like to thank my supervisors Dr. S Sridharan and Dr. J Solon Ivan for their guidance and support throughout my PhD tenure. Their immense experience and knowledge have encouraged me during my research life. I am fortunate to be part of NARL and I would like to thank Dr. Amit Kumar Patra, the Director of National Atmospheric Research Laboratory (NARL) for this opportunity. I am thankful to the NARL administration and other staffs for their support I have received throughout my tenure. I would like to thank Dr. S Unnikrishnan Nair, the Director of Indian Institute of Space Science and Technology (IIST) for the opportunity to pursue PhD in the institute.

The TIMED-SABER temperature and ozone volume mixing ratio data have been obtained from the website http://saber.gats-inc.com. ICON is supported by NASA's Explorers Program through contracts NNG12FA45C and NNG12FA421 ICON data are processed in the ICON Science Data Center at UCB and available at https://icon.ssl.berkeley.edu/Data. I would like to acknowledge the above data providers for making the data available in the public domain for the scientific community.

I would like to appreciate the love and support I received from all my family and friends. I have enjoyed the journey with my friends Dr. Arpita Munsi, Kavita Patnaik, Dr. Swetha Singh and Sritam Hajra who have made my NARL life fun-filled and cheerful. My batch mates Arun Kumar Panda, Akash Biswal, Donali Gogoi, Subhrajith Rath and Renju Nandan have made my PhD tenure colourful. Reetambhara Dutta had turned my conference trips into memorable ones. Moreover, I would like to extend my thanks to NARL staffs: security, housekeeping and canteen.

I am grateful to my parents Bindu P R and K N Sasikumar for their constant love and prayers. My sisters and brothers have cheered me on and celebrated every one of my accomplishments.

Finally, thanks to God for being there with me always.

Abstract

F-region irregularities develop under unique conditions of low magnetic inclination, eastward zonal electric field and vertical transport of plasma. These ionospheric irregularities are vastly studied for better prediction of the ionosphere. The F-region irregularities are usually observed during post-sunset hours. However, in solar minimum years, these irregularities are observed during delayed hours or around midnight hours and they are traditionally called the post-midnight F-region irregularities (PMF). The Rayleigh Taylor Instability (RTI) is considered to be the mechanism behind these irregularities. Studies have been conducted in this dissertation to determine the lower atmospheric forcing as well as the impact of the thermospheric winds on the post-midnight F-region irregularities.

The Equatorial Atmosphere Radar (EAR) observations at Kototabang (0.2°S, 100.3°E) are used to study the possible semidiurnal tidal influence on the occurrence of post-midnight F-region Field-Aligned Irregularities (FAI) echoes. It is found that the post-midnight FAI echoes show high percentage of occurrence (PO) during June–July and low PO in December–January of low solar activity years. As solar activity approaches minimum, the PO increase is extended to May, August, and September. The space-time Fourier analysis on the temperature information obtained from the Sounding of Atmosphere by Broadband Emission Radiometry (SABER) instrument onboard Thermosphere Ionosphere Mesosphere Energetics and Dynamics (TIMED) satellite reveals that at the low-latitude upper mesospheric heights, though the migrating diurnal tide propagating westward with zonal wavenumber (k) 1 (DW1) dominates the migrating semidiurnal tide propagating westward with k = 2 (SW2) during the equinox months, the SW2 tidal amplitudes are larger than DW1 during June–July. This indicates that the SW2 have a major role to play in the generation of the PMF.

The post-midnight F-region irregularities have low PO during boreal winter months. The ionosonde observations from Gadanki (13.4593° N, 79.1684° E) have shown that there is an increase in the PO of post-midnight spread-F (PMSF) during boreal sudden stratospheric warming (SSW) which occurred in December 2018- January 2019. The EAR observations also showed high PO of the post-midnight F-region FAI echoes during December 2018-January 2019. From the analysis of the tidal amplitudes from SABER temperature, the SW2 amplitude is found to be enhanced compared to the DW1 during boreal SSW of 2018-19. The hmF_2 (peak electron density height of F-region) and hpF (virtual height of the bottomside F-

region) is also found to have increased around midnight hours. The SW2 enhancement and the F layer uplift around midnight hours could have created conditions favouring the growth of the PMF.

From 2011-2019 EAR observations, an anomalous increase in the PO of post-midnight F-region FAI echoes is found in the equinox month of September 2019 which is investigated further. Inter-annual variability in PO for September also shows maximum PO in 2019 compared to other years even after removing geomagnetically disturbed days indicating the lower atmospheric dynamical forcing. Coincidently, an austral polar sudden stratospheric warming (SSW) event has occurred during September 2019, which precedes large planetary wave activity. Due to the circulation changes associated with the SSW, though the enhancement of ozone over the equatorial stratosphere is inferred from the space-borne SABER measurements, the expected increase in the amplitude of the upper mesospheric migrating semi-diurnal tide (SW2) is not observed in SABER temperature. But there is a drastic decrease in the amplitude of the DW1. The enhancement of stationary diurnal tide (DS0) suggests that the DW1 may have interacted with the planetary wave of zonal wavenumber 1 to generate DS0 at the expense of the DW1 tide.

Longitudinal variability in the PO of post-midnight F-region irregularities during Austral SSW of 2019 is determined using ionosonde measurements. The analysis of digisonde ionograms of Ascension Island (7.9°S, 14.4°W geographic; dip latitude: 16°S) for the geomagnetically quiet days shows a high percentage of occurrence (PO) of post-midnight spread F (PMSF) in September 2019. However, Jicamarca (11.95°S, 76.87°W, dip latitude: 1.10°N) digisonde observations do not show any significant increase in the PO. Besides, the wavelet spectrum of the hmF_2 shows a strong semi-diurnal (12 h) variation over Ascension Island, whereas diurnal (24 h) variation is dominant in Jicamarca. The high PO of PMSF and the semi-diurnal variation indicates the lower atmospheric tidal forcing. The two-dimensional spectral analysis of the space-borne SABER temperature measurements shows that the SW2 tidal amplitude exceeds the DW1 tidal amplitude at 10°N, which is close to the dip equator in the Ascension Island longitude, whereas the DW1 dominates at 10°S over the dip equatorial station, Jicamarca. The SW2 dominated tidal spectrum can drive semi-diurnal variation in the zonal electric field. The dominant semi-diurnal variation of the zonal electric field can become eastward at midnight hours and lift the F-layer to higher heights creating favourable conditions for the growth of the RTI to generate the F-region irregularities around midnight.

The winds and plasma drifts measured by the Michelson Interferometer Global High-resolution Imaging (MIGHTI) and Ion Velocity Meter (IVM) respectively onboard the Ionosphere Connection Explorer (ICON) satellite are used to investigate the seasonal and inter-annual variations of the thermospheric winds and F-region plasma drifts in the solar minimum years 2020-21. It is observed that the daytime vertical plasma drifts are upward, irrespective of season and longitude. Except in the fall equinox of 2020, the nighttime vertical plasma drifts are downward during winter and equinox. Over northern geomagnetic low latitudes, the meridional winds are equatorward during summer and poleward in winter. The meridional winds during nighttime (after 21:00 LST) are weakly poleward or equatorward in the equinox months of 2020, while they are poleward in 2021. Zonal drifts are similar to zonal wind variations with daytime westward and nighttime eastward drifts. While semi-diurnal variation is present in the vertical plasma drifts in summer, diurnal variation predominates in winter. Regardless of the season, diurnal variation is dominant in zonal winds and zonal plasma drifts. From these results, we can infer that the nighttime plasma drifts are upward when equatorward winds are present and downward when strong poleward winds are present. We can deduce that meridional winds may play a role in inducing upward plasma drifts, which may in turn create favourable conditions for the RTI and result in the occurrence of F-region irregularities, given that post-midnight F-region irregularities tend to occur in summer when equatorward winds and upward drifts are present.

Table of Contents

Chapter 1:
Introduction

Chapter 2:
Data and Methodology

Chapter 3:

Seasonal and solar activity variation in the percentage of occurrence of post-midnight F-region Irregularities

Chapter 4:

Tidal influence on the generation of post-midnight F-region irregularities

Chapter 5:

Boreal Sudden Stratospheric Warming (SSW) impact on the post-midnight F-region irregularities

Chapter 6:

Austral Sudden Stratospheric Warming impact on the post-midnight F-region irregularities

Chapter 7:

Longitudinal variation in the post-midnight F-region irregularities during Austral SSW of 2019

Chapter 8:

Role of thermospheric winds in the generation of post-midnight F-region irregularities

Chapter 9:
Summary and Scope for future work

List of Figures

xxiii

List of Tables

List of Acronyms

C/NOFS	:	Communications/Navigation Outage Forecasting System
CHAMP	:	Challenging Minisatellite Payload
DE3	:	Eastward propagating non-migrating diurnal tide with zonal wavenumber 3
DS0	:	Diurnal Stationary tide
DW1	:	Westward propagating migrating diurnal tide with zonal wavenumber 1
EAR	:	Equatorial Atmosphere Radar
EEJ	:	Equatorial Electrojet
EIA	:	Equatorial Ionisation Anomaly
EPBs	:	Equatorial Plasma Bubbles
ESF	:	Equatorial Spread-F
EUV	:	Extreme-Ultra Violet
FAI	:	Field Aligned Irregularities
foF2	:	Critical frequency of F_2 layer
GPS	:	Global Positioning System
hmF$_2$	:	Virtual height of peak electron density of F layer
hpF	:	Virtual height of bottomside F layer
ICON	:	Ionosphere Connection explorer
IDM	:	Ion Drift Meter
IR	:	Infra-Red
IVM	:	Ion Velocity Meter
LST	:	Local Solar Time
MDM	:	Midnight Density Maximum

MIGHTI	:	Michelson Interferometer for Global High-resolution Thermosphere Imaging
MLT	:	Mesosphere Lower Thermosphere
MSTIDs	:	Medium Scale Travelling Ionospheric Disturbances
MTM	:	Midnight Temperature Maximum
PMF	:	Post-Midnight F-region irregularities
PMSF	:	Post-Midnight Spread-F
PO	:	Percentage of Occurrence
PRE	:	Pre-Reversal Enhancement
PSF	:	Post-Sunset F-region irregularities
PSSF	:	Post-Sunset Spread-F
PW	:	Planetary Wave
RPA	:	Retarding Potential Analyser
RTI	:	Rayleigh Taylor Instability
RTI plots	:	Range Time Intensity plots
SABER	:	Sounding of the Atmosphere by Broadband Emission Radiometry
SFU	:	Solar Flux Unit
SNR	:	Signal Noise Ratio
SSW	:	Sudden Stratospheric Warming
SW2	:	Westward propagating migrating semi-diurnal tide with zonal wavenumber 2
TEC	:	Total Electron Content
TGCM	:	Thermosphere General Circulation Model
TIDs	:	Travelling Ionospheric Disturbances
TIEGCM	:	Thermosphere-Ionosphere Electrodynamics General Circulation Model

TIMED	:	Thermosphere Ionosphere and Mesosphere Energetics and Dynamics
UML	:	University of Massachusetts Lowell
UV	:	Ultra-Violet
VHF	:	Very High Frequency
VMR	:	Volume Mixing Ratio
PSSF-JIC	:	Post-Sunset Spread-F over Jicamarca
PSSF-ASC	:	Post-Sunset Spread-F over Ascension Island
PMSF-JIC	:	Post-Midnight Spread-D over Jicamarca
PMSF-ASC	:	Post-Midnight Spread-F over Ascension Island
GIRI	:	Gadanki Ionospheric Radar Interferometer
PSD	:	Physical Sciences Division
DPS	:	Digisonde Portable Sounder
HF	:	High Frequency
NICT	:	National Institute of Information and Communications Technology
ESRL	:	Earth System Research Laboratory
GSWM	:	Global Scale Wave Model
NmF_2	:	Peak electron density of F_2 layer
WAM	:	Wave Model

xxx

List of Publications

1. Sridharan, S., & Meenakshi, S. (2020). Semidiurnal tidal influence on the occurrence of postmidnight F region FAI radar echoes. Journal of Geophysical Research: Space Physics, 125(8), e2019JA027700.

2. Meenakshi, S., Sridharan, S., Solomon Ivan, J., Hozumi, K., Yatini, C., Yokoyama, T., & Hashiguchi, H. (2021). Anomalous Increase in the Occurrence of Post-Midnight FAI Radar Echoes in September 2019 and Its Relation with the Austral Sudden Stratospheric Warming. Journal of Geophysical Research: Space Physics, 126(6), e2020JA028902.

3. Meenakshi, S., Sridharan, S., & Ivan, J. S. (2022). Tidal influence on the longitudinal variabilities of the post-midnight spread F during September 2019. Advances in Space Research, 69(1), 111–120.

4. Meenakshi, S., Sridharan, S., & Ivan, J. S. (2022). Migrating and non-migrating tidal influences on the high occurrence of post-midnight spread F over Ascension Island during solar minimum. Advances in Space Research, 69(9), 3398–3416.

Other collaborative research work:

1. Dutta, R., Sridharan, S., Meenakshi, S., Ojha, S., Hozumi, K., & Yatini, C. (2022). On the high percentage of occurrence of type-B 150-km echoes during the year 2019 and its relationship with mesospheric semi-diurnal tide and stratospheric ozone. Advances in Space Research, 69(1), 80–95.

Publications not related to thesis:

1. Meenakshi, S., & Sridharan, S. (2023). Remarkable changes in F region winds and plasma drifts during the stratospheric QBO disruption of 2019–2020. Advances in Space Research, 71(11), 4568–4575.

Conferences /Workshops/Symposiums attended

1. Presented at 2022 8th IAGA/ICMA/SCOSTEP Workshop on Vertical Coupling in the Atmosphere-Ionosphere System held from 11-15 July 2022, Sopron, Hungary

2. Delivered a talk in the Plenary Session 2: Middle atmosphere, atmospheric coupling, dynamics and climate change of the 21st National Space Science Symposium (NSSS) held from 31 January to 22 February 2022

3. Presented in the commission G: Ionospheric Radio and Propagation of the 2022 URSI Regional Conference on Radio Science (URSI-RCRS 2022) held from 1 December -4 December 2022, IIT Indore

4. Presented at ICTP-SCOSTEP-ISWI Workshop on the Predictability of the Solar-Terrestrial Coupling-PRSETO held from 30 May 2023-02 June 2023 at ICTP, Trieste, Italy

Chapter 1:

Introduction

1.1 Ionosphere

Ionosphere is the partially ionised part of the atmosphere which extends approximately from 60 to 1000 km in altitude. The number density of the electrons in the ionosphere is large enough to reflect the radio waves (Kelley, 1989, Hargreaves, 1992, Rishbeth, 2002). The neutrals of the atmosphere are ionised mainly by the solar X-rays and UV radiation by the process of photoionisation and at higher latitudes by the precipitation of energetic charged particles.

$$a + h\nu \longrightarrow a^+ + e$$

where 'a' is a neutral particle. The interaction between solar radiation and neutrals are considered to be particle–particle interaction.

The rate of electron density of the ionosphere is determined by the production processes, loss mechanisms and transport. The ion production depends on many factors like the intensity of radiation (I), the number density (n) of the neutral particles, and absorption cross section (σ) of the neutrals.

$$q = \sigma n I$$

Loss mechanism is mainly through recombination reactions.

$$a^+ + e \longrightarrow a + h\nu$$
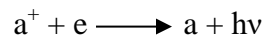
Transport is dominant in the upper part of the ionosphere. As intensity of solar radiation and neutral density varies with altitude, so does the plasma density of the ionosphere. Different chemical constituents react differently with the solar radiation which results in more than one electron density maximum. The electron density profile of the ionosphere varies over altitude, time of day, seasons and geomagnetic conditions (shown in Figure 1.1)

Ionosphere is divided into different layers D, E, F_1 and F_2 layers. D region found between ~60-90 km is ionised by Lyman-α radiation (121.6 nm), XUV, X-rays and cosmic rays. Electron density of D layer is between 10^8-10^9 el/m^3. Recombination rate is very high in the D region hence, it disappears during nighttime. Ionisation in the E-region (90-150 km) is mainly due to soft X-rays (1-10 nm) and UV radiation. Mainly molecular ions (O_2^+ and NO^+) are present in the lower part of the ionosphere. Both the D and E-region act as attenuator for the radio waves. Increasing the radio frequency can decrease the attenuation due to these layers. The F-region is the uppermost region of the ionosphere which is further divided into F_1 (150-180 km) and F_2 (above 180 km) layers. F_1 layer exists only during day time whereas the F_2 layer exists during both daytime and nighttime. The F-region above of F_2 peak is called topside and below as bottom-side of F-region. In D, E and F_1 layers, photochemical processes are dominant whereas F_2 is a transport regime.
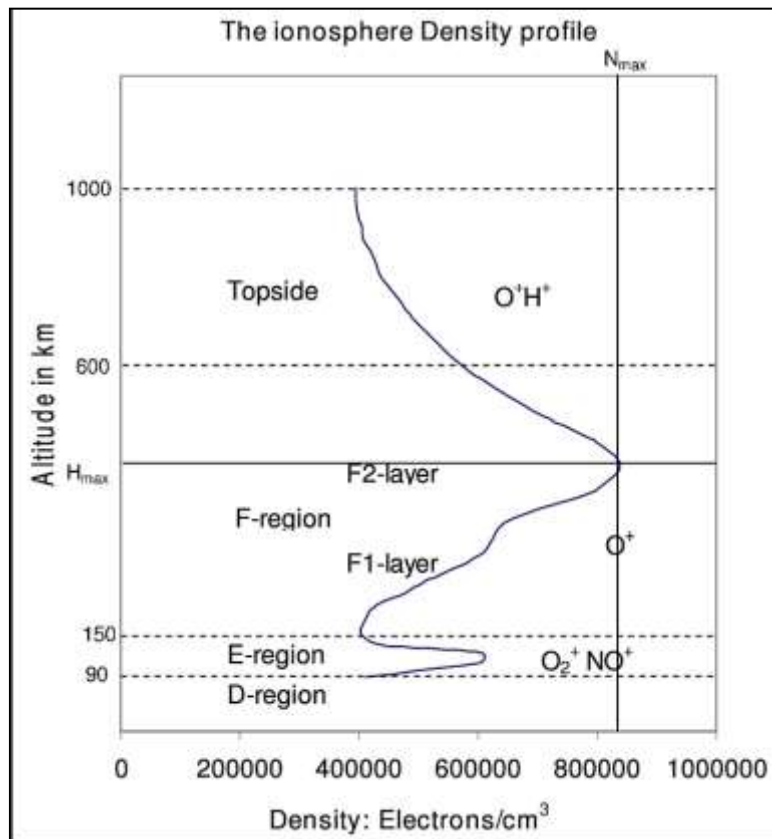
Figure 1.1: Electron density profile of ionosphere (Sibanda, 2006)

1.2 Chapman function

Sydney Chapman tried to explain formation of ionospheric layers mathematically. Chapman function could explain variations observed in different layers of the ionosphere (Chapman, 1931). After making a few assumptions like only one chemical constituent is present, atmosphere is plane stratified, photoionization is the only production process, loss is through recombination and scale height is constant, an expression showing variation of the plasma density with solar zenith angle and altitude is established.

$$q = q_0 e^{[1-z-\sec\chi(e^{-z})]}$$

where q is the production rate; z is altitude and χ is solar zenith angle. Maximum production rate is q_0 when χ is 0. The chapman layer, where the production rate is directly proportional to square of electron density is called alpha-chapman layer and in beta-chapman layer, the electron density is directly proportional to the production rate. Seasonal and daily variations of layers of ionosphere can be determined by these equations. Highest production rate is when the Sun is highest in the sky. D, E and F_1 are chapman layers whereas F_2 is non-chapman layer.
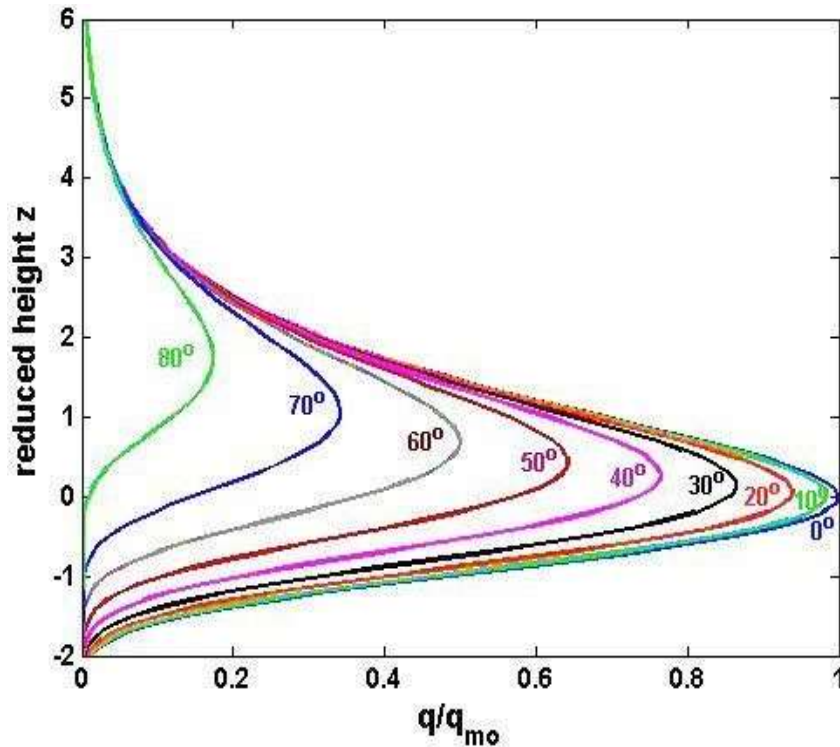
Figure 1.2: Chapman production function (Tesema, 2010)

1.3 Electrical conductivity of ionosphere

As the ionosphere contains free electrons and ions it has electrical conductivity larger than the lower atmosphere. But the conductivity is anisotropic because the Earth's magnetic field restricts the charged particles' motion in direction perpendicular to the magnetic field (Hirono, 1952; Baker and Martyn, 1952, 1953; Fejer, 1953; Maeda, 1955; Kato, 1956). Variation of the conductivity over altitude results in generation of polarization charges.

$$\sigma = \frac{J}{E}$$

where $\boldsymbol{\sigma}$, $\mathbf{J}$ and $\mathbf{E}$ are conductivity, current density and electric field respectively. There are three types of conductivities existing in the ionosphere. They are direct or longitudinal conductivity $(\boldsymbol{\sigma_0})$, Pedersen conductivity $(\boldsymbol{\sigma_p})$ and Hall conductivity $(\boldsymbol{\sigma_h})$. The direct conductivity is along magnetic field $(\mathbf{B})$ and electric field $(\mathbf{E})$. The conductivity which is perpendicular to magnetic field and parallel to electric field is the Pedersen conductivity whereas conductivity perpendicular to both $\mathbf{E}$ and $\mathbf{B}$ is the Hall conductivity.

$$\sigma_0 = \left[\frac{Ne}{meve} + \frac{Ni}{mivi}\right]|e^2|$$

$$\sigma_p = \left[\frac{Ne}{me}\left(\frac{ve}{ve^2+\omega e^2}\right) + \frac{Ni}{mi}\left(\frac{vi}{vi^2+\omega i^2}\right)\right]|e^2|$$

$$\sigma_h = \left[\frac{Ne}{me}\left(\frac{\omega e}{ve^2+\omega e^2}\right) - \frac{Ni}{mi}\left(\frac{\omega i}{vi^2+\omega i^2}\right)\right]|e^2|$$

where ω, v denote gyro-frequency and collision frequency with subscript e and i for electrons and ions respectively. The height profile of the different conductivities is shown in Figure 1.3.

Direct conductivity increases exponentially with altitude as the collision frequency decreases with altitude. Both the Hall and Pedersen conductivity peaks in the E-region. $\boldsymbol{\sigma_h}$ is confined to E-region and follows electron density profile.

4
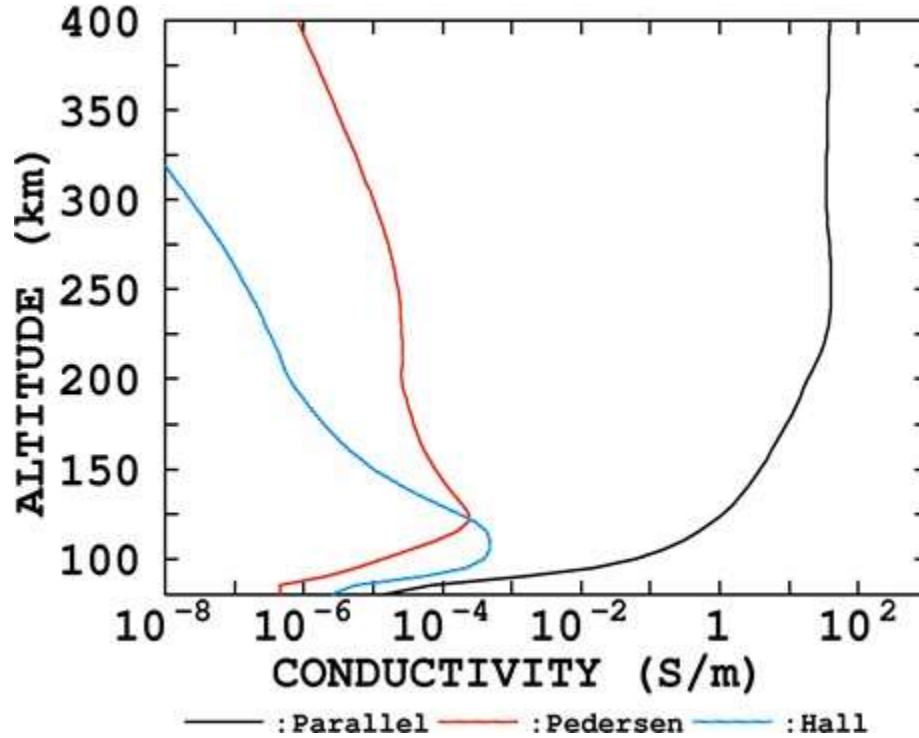
Figure 1.3: An example of the altitude profile of ionospheric conductivity (Yamazaki and Maute, 2017)

1.4 Ionosphere dynamo

Mechanism of converting kinetic energy of the winds into electrical energy by collisions between charged particles and neutrals is called ionosphere dynamo. Charged particles in E and F-region of ionosphere are affected by the Earth's magnetic field. In D region (below 90 km) collisions between neutrals and charged particles are dominant. The Dynamo region exists between 90 km and 160 km where considerable current flows. In F-region (~above 130 km) both ions and electrons are controlled by magnetic field and collisions with neutrals become unimportant. In E-region, between ~90 km and 120 km ions are controlled by collisions with neutrals whereas electrons will be restricted by magnetic field. The differential motion between ions and electrons result in electric current flow. E-region dynamo and F-region dynamo behave as voltage and current generators respectively (Rishbeth, 1971, 1997; Heelis et al., 1974).

1.4.1 E-region dynamo

Tidal oscillations drive the E-region dynamo (Baker and Martyn, 1953; Chapman, 1956). Tides are mainly driven by solar heating. Majority of the tides are either diurnal or semi-diurnal and are mainly generated by absorption of solar radiation by ozone and water vapour in the lower atmosphere. The amplitude of the tides increases with altitude. Those tides which remain in phase over ionospheric dynamo region (~90-120 km) can only produce significant currents and hence establish the dynamo process (Baker and Martyn, 1953; Chapman, 1956; Richmond et al., 1976; Rishbeth and Garriot, 1969).

Neutral winds (**U**) blowing across magnetic field lines exerts Lorentz force on charges. The extent to which the electrons get affected depends on the ratio of their collision frequency (ν) to the gyro frequency (ω). Above ~90 km the ions drift under the action of winds since $\nu_i >> \omega_i$ whereas electrons have $\nu_e << \omega_e$. These ions accumulate at a rate given by $\mathbf{\nabla}.\mathbf{N_e q V_i}$ where $\mathbf{V_i}$ is ion drift velocity and polarization electric field is set up. Electrons will undergo gyration under the magnetic field lines to adjust this charge distribution. The electric field $\mathbf{E_p}$ thus generated causes the ions and electrons to drift across the magnetic field lines such that current is divergence free.

$$\mathbf{\nabla}.\mathbf{J} = \mathbf{\nabla}.\mathbf{N_e q}(\mathbf{V_i} - \mathbf{V_e}) = \mathbf{0}$$

where $\mathbf{V_e}$ is electron drift velocity. The current $\mathbf{J} = \mathbf{\sigma}.\mathbf{E`}$ where $\mathbf{E`}$ consists of induced component $\mathbf{U} \times \mathbf{B}$ due to winds and polarization component $\mathbf{E_p}$. The polarization electric field $\mathbf{E_p}$, is produced by the potential due to charge distribution

$$\mathbf{E`} = \mathbf{E_p} + \mathbf{U} \times \mathbf{B}$$

where $\mathbf{E_p} = - \mathbf{\nabla}\varphi$

The potential φ depends on global distribution of winds and conductivity. E layer is responsible for current system known as Sq current system. Intensity variation of these currents can be measured using magnetometers. Sq current flow is anti-clockwise in the northern hemisphere and clockwise in the southern hemisphere. Near the equator there will be an intense eastward

Pedersen current i.e. from dawn side to dusk side due to contribution from both the hemispheres. The resultant eastward electric field is called dynamo electric field.

1.4.2 F-region dynamo

Thermospheric winds generated by pressure gradient due to solar EUV heating are the main driving force for the F-region dynamo (Rishbeth, 1971). It develops after sunset when the E-region conductivity decreases. The F-region can be approximated into slab geometry with a well-defined lower boundary (Figure 1.4).

Inside the slab the F-region has finite Pedersen conductivity (σ_P) whereas the conductivity is zero outside. Eastward zonal wind (**U**) is constant inside as well as outside the slab. An upward current flows inside the slab. Since the current (**J**) cannot flow outside the slab there will be piling up of charges at the boundaries giving rise to a polarisation electric field (**E$_p$**) in the vertical direction.

The vertical electric field along with the northward magnetic field results in zonal drift (**V$_d$**) of the plasma in the same direction as the zonal wind i.e. eastward during the nighttime (Rishbeth, 1971; Heelis et al., 1974).
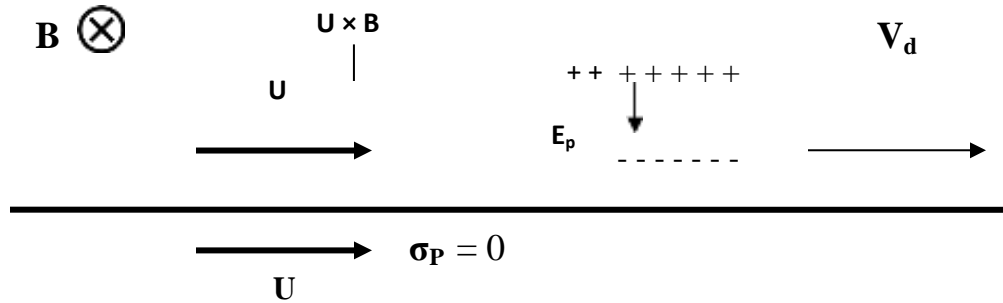
Figure 1.4: Schematic diagram explaining F-region dynamo

For a perfect F-region dynamo

$$\mathbf{E} + \mathbf{U} \times \mathbf{B} = 0$$

This means that the electromagnetic force on the plasma vanishes and the thermospheric wind blows freely without ion drag. Observations of zonal plasma drift and neutral winds velocities during nighttime have shown that they have nearly same magnitude. During daytime, the E-region conductivity is comparable or more than the F-region conductivity hence, the F-region charges cannot pile up during daytime and the ion drag remain high.

Equatorial ionosphere has horizontal magnetic field lines and hosts many complex as well as peculiar phenomenon. These are Equatorial Electrojet (EEJ), Appleton Anomaly / Equatorial Ionisation Anomaly (EIA), Pre-Reversal Enhancement (PRE) and Equatorial Spread-F (ESF). They depend on latitude, longitude, season, solar activity and the geomagnetic conditions.

1.5 Equatorial Electrojet (EEJ)

An intense eastward current in the dynamo region (90-130 km) over latitudinal belt $\pm 3°$ centered at the dip equator is called Equatorial Electrojet (EEJ) (Forbes, 1981). Pedersen conductivity peaks at 140 km and Hall conductivity at 120 km. Their value decreases rapidly both above and below these heights. This results in a slab model current. In both D and F-region, the current is negligible whereas, current is present in the E-region. The eastward dynamo electric field will lead to an eastward Pedersen current ($\mathbf{J_x}$) and downward Hall current ($\mathbf{J_z}$). The flow of Hall current is disrupted due to low conductivity both above and below the slab. This result in the buildup of polarization charges which results in an upward Pedersen current given by $\boldsymbol{\sigma_p E_Z}$
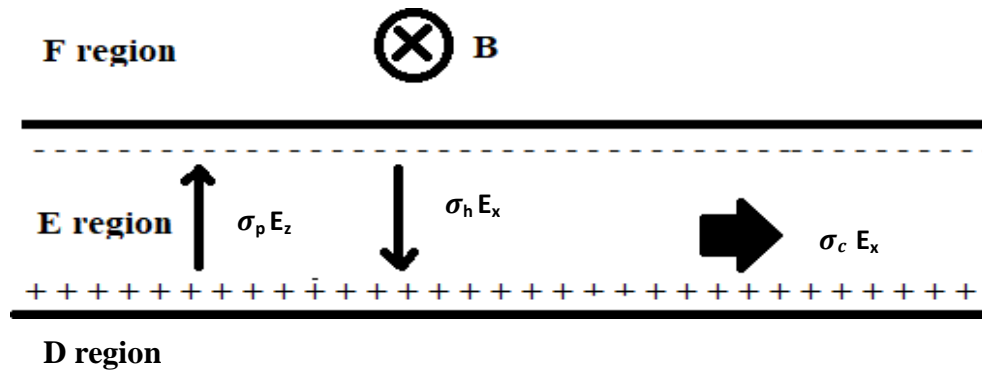
Figure 1.5: Schematic diagram describing equatorial electrojet (EEJ)

The vertical current should be zero inside the slab

$$\sigma_p E_z = \sigma_h E_x$$

The polarization electric field drives an eastward Hall current. Current density is given by

$$Jx = \left[\sigma_p + \frac{\sigma_h^2}{\sigma_p}\right] E_x = \sigma_c \, E_x$$

where σ_c is called cowling conductivity. In lower E-region, σ_p values are small and hence the ratio of $\frac{\sigma_h^2}{\sigma_p}$ will be a large value leading to large eastward current.

1.6 Equatorial Ionisation Anomaly (EIA)
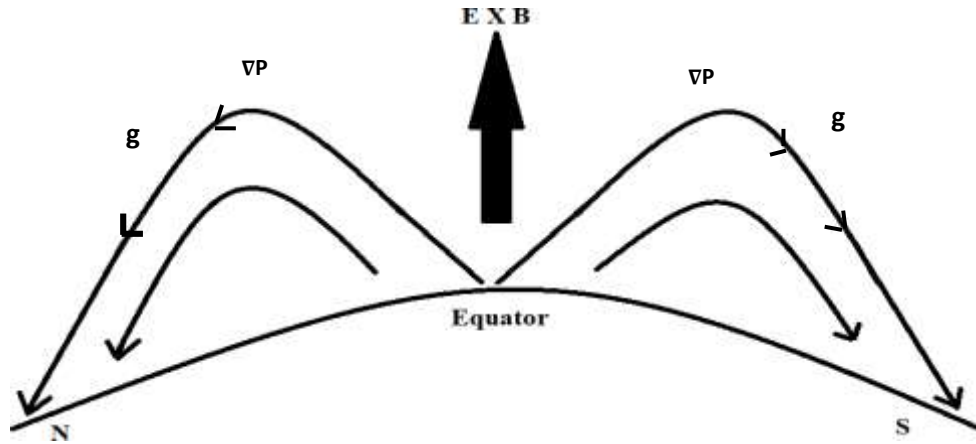
Figure 1.6: Electron drifts motion over the dip equator and formation of Equatorial Ionisation Anomaly (EIA)

Under $\mathbf{E} \times \mathbf{B}$ drift over the dip equator the F-region plasma is lifted to higher heights. Once it reaches the topside of the F-region, the plasma loses its momentum and flows out by diffusion along the magnetic field lines due to pressure gradient or by gravity to off-equatorial latitudes i.e. 15°-18° on either side of the dip equator. This result in a latitudinal structure in ionisation distribution characterised by two crests on either side of the dip equator and a trough over the dip equator. This is known as Equatorial Ionisation Anomaly (EIA). EIA is extended throughout the F-region.

Ionosonde and TEC observations have shown that the EIA has day to day as well as longitudinal variability. The daytime EEJ and EIA are driven by the zonal eastward electric field hence their intensities are related. An intense EEJ can be associated with a well-developed EIA.

1.7 Pre-reversal Enhancement (PRE)

During daytime the zonal electric field is eastward and in the presence of horizontal magnetic field the plasma drift will be upward. However, during nighttime, the electric field is westward. Before this reversal there is a brief enhancement in the eastward electric field called the Pre-Reversal Enhancement (PRE). The parameters that drive the PRE are important since it holds the key for the irregularities that develop after the sunset in the F-region. Three mechanisms are discussed here.
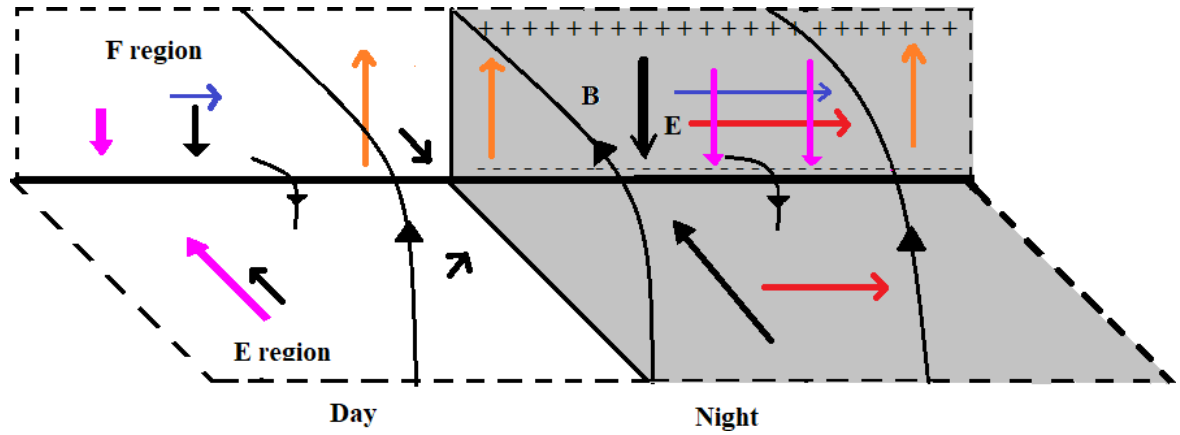
Figure 1.7: Schematic diagram showing mechanism producing PRE (Rishbeth, 1971)

1. Rishbeth (1971a, 1971b) proposed a mechanism for the PRE. The zonal neutral wind (blue arrows) drives a vertical dynamo current (orange arrows). Current divergence result in build-up of polarisation charges in the F-region. The F-region is electro-dynamically coupled to the E-region. The F-region dynamo electric fields will be short out by the daytime Pedersen currents (pink arrows) in the E-region. However, after sunset the E-region conductivity drops and hence the downward electric field cause the plasma to drift (red arrows) with the neutral winds. The rapid change in the E-region downward polarisation electric field generates a small horizontal electric field as an edge effect and the vertical plasma drift due to PRE.

10

Eccles (1998a) demonstrated that the PRE magnitude is proportional to the zonal gradient of the downward polarisation **E** due to the F-region dynamo.

2. This was given by Farley et al. (1986) based on a simulation study. In this study they injected a 200 m/s eastward wind after suppressing the E-region dynamo although its conductivity and loading effect on F-region are retained. This produced PRE well. Sketch showing the mechanism is given in Figure 1.8. The eastward neutral wind in the F-region causes downward electric field on both sides of the terminator. On the dayside, the electric field is smaller but non-zero because of the E-region conductivity to which the F-region is connected by magnetic field lines. This electric field which is mapped to the E-region drives a westward Hall current in the E-region on both sides of the terminator. The longitudinal gradient in the conductivity results in the buildup of negative charges near the terminator. The collection of negative charges near the terminator creates a localised zonal eastward electric field on dayside terminator maps to F-region
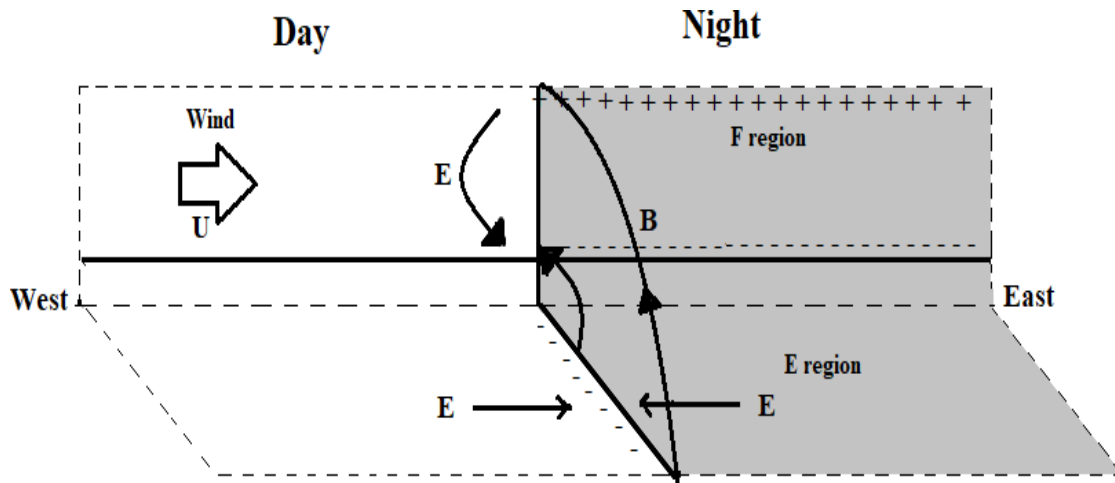
Figure 1.8: Schematic diagram showing mechanism producing PRE (Farley et al., 1986)

3. In this mechanism, the F-region dynamo (Rishbeth, 1981) is recognised to be driving the vertical Pedersen current and the electrojet supplies the current demanded by the F-region dynamo. The rapid drop of conductivity in the Equatorial Electrojet at sunset coupled with increased current of the F-region dynamo on the night side requires an additional enhanced electric field. The PRE draws the electrojet current zonally to meet the current demands of the F-region dynamo on the night side (Haerendel et al., 1992).

This enhancement of the zonal electric field during post-sunset hours due to the PRE shows day to day variability. This enhanced electric field can lift the F layer plasma to higher heights during the post-sunset hours.

1.8 Equatorial F-region irregularities

The thermosphere and equatorial ionosphere constitute a coupled system and possess many peculiar characteristics which are unique to this region compared to the other latitudes. It is due to the horizontal magnetic field and the large solar radiant energy absorbed as compared to other latitudes. During night, the tropical ionosphere which includes both equatorial and low latitude ionosphere develops plasma instabilities leading to plasma density irregularities which are distributed in a wide spectral band. These variabilities can be due to the vertical coupling from the lower atmosphere through atmosphere waves and tides as well as magnetosphere-ionosphere coupling. The horizontal magnetic field favours the vertical plasma transport process that controls the major phenomenology of this region by dynamo electric fields and winds (Abdu, 2005).

Equatorial nighttime ionosphere is unstable to density perturbations which depend upon the ambient ionosphere-thermosphere conditions arising from sunset electrodynamic processes. The pre-reversal enhancement (PRE) of the zonal electric field which lifts the F layer to higher altitudes will result in steepening of the bottom side density gradient and this sets the condition for the instabilities to develop. The instability is believed to be driven by gravitational Rayleigh Taylor Instability (RTI) mechanism (shown in fig 1.9). This is similar to the condition when a heavy fluid is resting on lighter fluid.

F layer bottom-side density n_1 above and vanishing below ($n_2=0$) will provide a similar condition. The magnetic field **B** is horizontal and gravity **g** downward. Gravity driven current **J** will be in x direction depending on the electron number density 'N' so that any change or perturbation in N could cause divergence and charges will pile up at the edges of the perturbation. The perturbation electric field developed due to the charge pile up can drift the ions and electrons in upward direction in charge depleted region and downward in charge enhanced region thereby increasing the perturbation leading to the growth of instability. The plasma depletion regions are called Equatorial Plasma Bubbles (EPBs). The F-region

irregularities are considered to be related to these EPBs. The system will be stable if the direction of **g** and **∇n** are parallel, which is the case of top side F- region where, the instability does not develop.
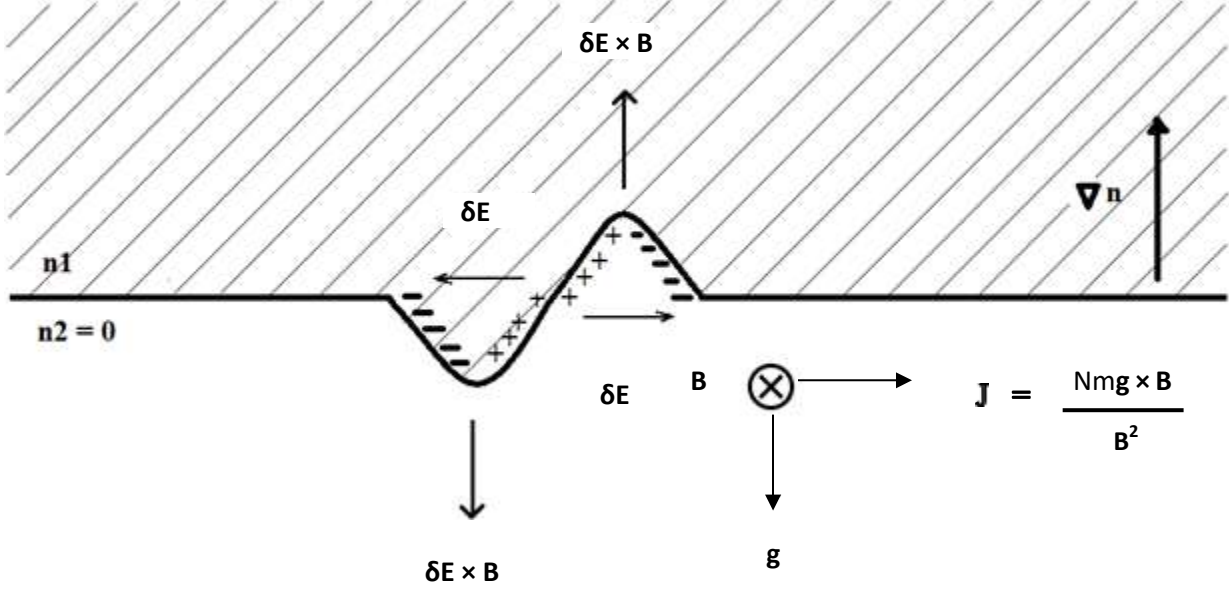
Figure 1.9: Schematic showing Rayleigh Taylor Instability (RTI) mechanism
(Kelley, The Earth's Ionosphere, 1989)

Growth rate of RTI (γ) is given by the equation:

$$\gamma = \frac{\Sigma_P^F}{\Sigma_P^E + \Sigma_P^F} \left[\frac{E}{B} + \frac{g}{v_{in}} \right] \frac{\nabla n}{n} - \alpha N_e$$

where **E** is the eastward electric field, **B** magnetic field, v_{in} is ion-neutral collision frequency, **g** is acceleration due to gravity, **∇n** is density gradient, α is recombination coefficient and N_e is electron density, Σ_P^E and Σ_P^F is flux integrated Pedersen conductivity for the E and F region

1. Spread-F irregularities are generated when the growth rate is positive and sufficiently large and $\gamma \gg \alpha N_e$.

2. Irregularities develop at the bottomside of the F-region where **∇n** and **g** are anti-parallel to each other.

3. The ν_{in}, the ion-neutral collision frequency, has an inverse relationship with the growth rate of RTI, which means lower the value of ν_{in}, more likely is that the instability will grow (Woodman and LaHoz, 1976; Abdu, 2001; Abdu et.al., 1982).

1.8.1 Post-sunset F-region irregularities

Equatorial plasma bubbles (EPBs) are regions where plasma density will be lower than its environment and aligned along the magnetic field lines. Equatorial F-region irregularities are considered to be due to the EPBs and can take different forms like spread in the F layer traces in ionograms called Equatorial Spread-F (ESF), plasma depletions observed by the satellite, bite outs in Total Electron Content (TEC) and backscattered echoes from Field Aligned Irregularities (FAI echoes) in VHF radar maps (e.g., Woodman and LaHoz., 1976; Abdu et al., 1981; Sripathi et al., 2008).
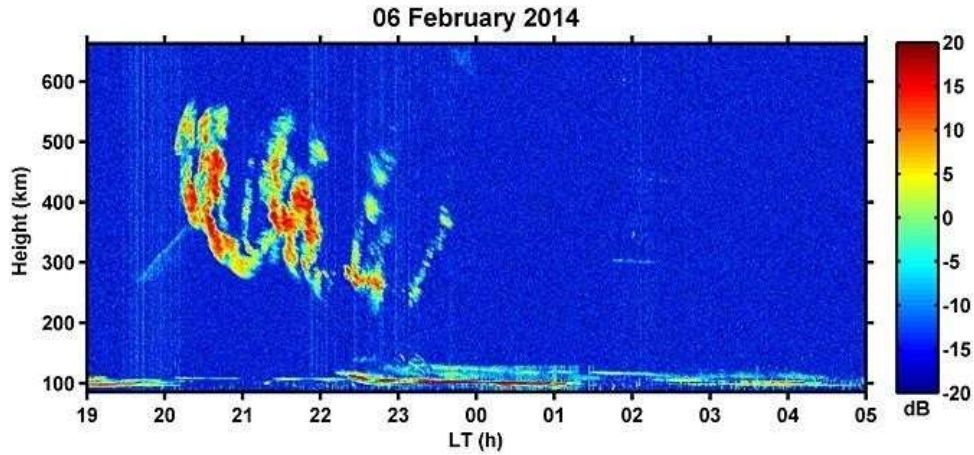
Figure 1.10: Height-time variations of SNR of the F-region FAI echoes observed by GIRI on 6 February 2014 (Patra et al., 2014)

Although the ESF was discovered by Booker and Wells (1938) it still attracts attention because of its influence on radio waves of ionospheric communication as well as navigation. Their morphology, seasonal variations, latitude, longitude variations and the dynamic aspects have been studied reasonably well. Subbarao and Krishnamurthy (1994) investigated the occurrence of ESF over the Indian sector and it was found that their occurrence rate increases with solar

activity after sunset and are more common during equinox months. Studies have found that they are usually generated after 18:00 LST. Their occurrence is maximum during equinox months of solar maximum years (Fejer and Kelley, 1980; Abdu, 2001) when the solar terminator will be parallel to the geomagnetic filed lines enhancing the PRE over the longitudes where declination is almost zero. The F layer altitude also plays a key role in the generation of the F-region irregularities as at higher altitudes the ion-neutral collision frequency is very low which in turn will favour the growth of the RTI. The enhancement of the eastward electric field due to PRE after the sunset hours and $\mathbf{E} \times \mathbf{B}$ drift velocity are important factors influencing the post-sunset F-region irregularities.

1.8.2 Post-midnight F-region irregularities

The F-region irregularities are usually generated during the post-sunset hours however, they are observed during delayed hours or midnight hours in the ionograms over the Indian sector by Sastri (1999). These irregularities are customarily called the post-midnight F-region irregularities. They are recently observed as Field Aligned Irregularities echoes (FAI) in VHF radar over geomagnetic low latitudes around midnight hours (after 22:00 LST) by Patra et al. (2009) and Otsuka et al. (2009).

They have occurrence characteristics different from that of the post-sunset F-region irregularities. The post-midnight F-region irregularities maximises during June solstice of solar minimum years. Its maximum occurrence is found to be over the African sector during June solstice by Yizengaw et al. (2013) using C/NOFS, indicating their occurrence have longitudinal dependence. The post-midnight F-region irregularities are not accompanied by GPS scintillations as the amplitude of these plasma perturbations are very small. Otsuka et al. (2012) have noted that the zonal drift velocity of the post-midnight FAI echoes are different from the ambient F-region plasma as observed from incoherent scatter radar and satellite measurements (Fejer et al., 1993). Their generation mechanisms are still extensively debated. The occurrence of these post-midnight F-region irregularities during solar minimum years indicates that they can be due to vertical coupling between the lower atmosphere and ionosphere. Day to day variability in the occurrence of the F-region irregularities can be attributed towards the probability of seeding mechanism for the instability.
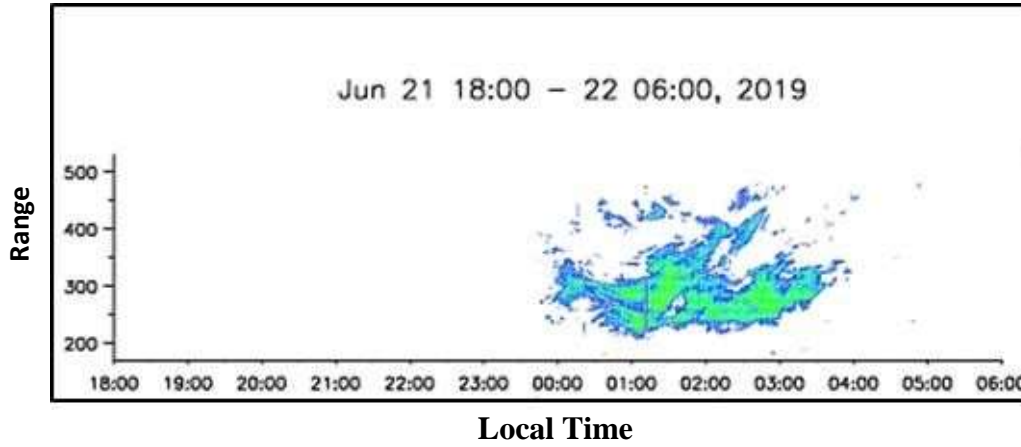
Figure 1.11: An example of EAR F-region observations showing post-midnight F-region FAI echoes on June 2019 (https://www.rish.kyoto-u.ac.jp)

Gravity waves are considered to be one of the seeding mechanisms. They are usually generated from severe convection sites (eg. Inter Tropical Convergence Zone) in troposphere. Medium Scale Travelling Ionospheric Disturbances (MSTIDs) are also considered to be one of the candidates for seeding the instability for post- midnight plasma bubbles (Miller et al., 2009). The nighttime MSTIDs at middle latitudes could be generated by Perkins instability and propagate southwestward (northwestward) in the northern (southern) hemisphere. They could be accompanied by polarization electric field to maintain divergence free current (e.g., Shiokawa et al., 2003; Otsuka et al., 2004). MSTIDs are common at mid-latitudes. By using airglow imager and ionosonde observations Candido et al. (2011) presented the seasonal as well as local time variations in spread-F over Cachoeira Paulista (22.7°S, 45.0°W; dip latitude: 16°S) and suggested MSTIDs as one of the main sources of post-midnight spread-F. However, MSTIDs never really reach dip equator as the equatorial anomaly crests can serve as a boundary for their propagation. Moreover, Shiokawa et al. (2006) have ascertained that the poleward propagating MSTIDs are not accompanied by polarisation electric field. To maintain current continuity the direction of the polarisation electric field should be in the meridional direction because the phase front of the plasma density perturbations is elongated along the zonal direction. The polarisation electric fields in the meridional direction can only results in drift of plasma in the zonal direction and thus do not form plasma density perturbations (MSTIDs). Further investigation is required towards MSTIDs as the seeding mechanism for the post-midnight F-region irregularities.

From the observations from Ion Velocity Meter (IVM) from C/NOFS Coley et al. (2014) observed that the zonal plasma velocities largely depend on solar activity and it is largely westward during the midnight and post-midnight period of low solar activity years. During nighttime the electric field is westward which means **E/B** in the growth rate of the RTI is negative. But during nighttime ion-neutral collision frequency (ν_{in}) is found to be low which can compensate for the negative value of **E/B** and thereby make the growth rate positive. The value of ν_{in} can again decrease when the F layer is shifted to higher heights. Moreover, ν_{in} is smaller during nighttime than daytime and further, it increases during low solar activity years because ν_{in} is proportional to the neutral density, which is smaller at night than during the day and decreases with decreasing solar activity (Picone et al. 2002). Uplift of the F layer around midnight has been observed by Nicolls et al. (2006) using ionosonde observations in Brazil.

What can be the possible mechanisms behind the lifting of the F layer during midnight hours in the absence of PRE like feature?

1. The decreasing westward electric field along with sufficient recombination during nighttime can favour the lift in the F layer during delayed hours (after 22:00 LST). The weak westward electric field can be due to enhanced equatorward winds or abatement in the poleward winds.
2. The component of the wind along the magnetic field can alter the local conductivity due to collisional drag. The equatorward winds can push the plasma to higher heights and thereby decrease the Pedersen conductivity. The decrease in Pedersen conductivity increases the growth rate of RTI as the conductivity term of the E and F-region is in the denominator of growth rate.
3. The equatorward winds can be due to Midnight Temperature Maximum (MTM), a phenomenon where the neutral temperature in the thermosphere attains local maxima around midnight. The MTMs more frequently occur during low solar activity conditions which are consistent with the post-midnight F-region irregularities (Niranjan et al., 2006).

Akmaev et al. (2010) revealed that MTM could be due to the tides. The ter-diurnal tide propagating upward can increase neutral temperature around midnight. The MTM can be

accompanied by Midnight Density Maximum (MDM). The convergence of thermospheric winds over the dip equator could result in MDM and MTM by adiabatic heating (Herrero, 1982). Hence the tides can play a role in the generation of the post-midnight F-region irregularities.

1.9 Atmospheric tides

Oscillations of the atmosphere can be due to the gravitational pull of the Sun or the Moon as well as due to thermal action of the Sun (Siebert, M. 1961; Forbes, 1982). Atmospheric tides are the oscillations of the atmosphere due to both of them. The solar energy in the atmosphere entirely does not go into excitation of tides. The region of mesosphere and lower thermosphere (MLT) is characterised by the presence of tides, atmosphere gravity waves and planetary waves. Only a small part of electromagnetic radiation is absorbed above 100 km. Hence the thermal tides are excited mostly in the middle as well as lower atmosphere from where they propagate upwards. Thermal tides play an important role in the global atmospheric dynamics and coupling between thermosphere and ionosphere.

Atmospheric pressure, density, temperature and wind are subjected to variations of 24 hrs, 12 hrs and 8 hrs. These variations in atmospheric parameters with diurnal, semi-diurnal and ter-diurnal periods are caused due to the heating of atmosphere by water vapour (troposphere) and ozone (stratosphere and mesosphere). Particular patterns are generated with latitudes, altitudes and longitudes by heating (Reddy, 1991). The diurnal tidal amplitudes from the Indian MST radar wind measurements over Gadanki in solstice and equinox months have maxima between 3 km and 20 km and the vertical profile of the amplitude suggests that they are generated by diurnal heat sources like solar heating of water vapour, planetary boundary layer heat flux and latent heat release from deep convective clouds and radiation absorption by clouds (Sasi et al., 2001).

Atmospheric tides are generally of two types: migrating and non-migrating tides. Migrating tides moves westward with the apparent motion of the Sun. Non-migrating tides propagate eastward or westward or can be stationary with respect to ground (Miyahara and Miyoshi, 1997; Pancheva and Muktharov, 2011; Smith, 2012). Migrating solar tides are generated via absorption of infrared radiation (IR) by water vapour, ultraviolet radiation (UV) by ozone (O_3) and oxygen (O_2). Latent heat release from deep convective systems can also generate tides. The longitudinal

differences in the heat sources and interaction between the planetary waves and migrating tides are considered to the sources of non-migrating tides (Forbes 1982a, 1982b; Hagan and Forbes, 2003; Oberheide et al., 2002). Lindzen (1978) hypothesized that the latent heat release could be significant for the excitation of atmospheric diurnal tide. Hamilton (1981) provided experimental evidence for the same. The diurnal tides over the tropics show equinoctial maxima with larger amplitudes during boreal vernal equinox (Vincent et al., 1988, 1998). The short term variability of the diurnal tides can be attributed to its interaction with planetary scale waves in the MLT region. Solar semi-diurnal tides are as large as the diurnal tides in the lower thermosphere at middle as well as higher latitudes whereas diurnal tides largest at low latitudes (Forbes, 1982a, b).

Tides are normally presented in harmonic components. Tides vary largely with altitude and latitude but very little with longitude. Any tidal oscillation can be expressed as

$$q = q^{\sigma,s}(\theta, z)e^{i(\sigma t + s\varphi)}$$

where $\frac{\partial}{\partial t} = i\sigma$ and $\frac{\partial}{\partial \varphi} = is$, φ is longitude, z is height corresponding to chosen value of σ and s $\frac{2\pi}{\sigma}$ is whole or some suitable fraction of solar or lunar day. For diurnal, semi-diurnal and ter-diurnal $\frac{2\pi}{\sigma}$ = 24, 12 and 8 respectively and σ takes values 1, 2 and 3 respectively. 's' is the zonal wavenumber and can be = 0, ±1, ±2, ±3… Negative values indicate that it is westward travelling waves whereas positive values for eastward travelling waves. 's' = 0 refers to standing waves. For example s = ±1 is migrating diurnal tide and s = ±2 is migrating semi-diurnal tide. 'θ' is the colatitude.

Atmospheric tides can affect the chemistry, dynamics of the MLT by transporting energy and momentum from the lower atmosphere. They can also modulate the gravity waves by critical level filtering. The tides play a key role in atmosphere and ionosphere coupling (Immel et al., 2006; Pedatella et al., 2012; Vineeth et al., 2011). Modelling studies have shown that tides can reach significant amplitudes under solar minimum conditions influencing the zonal electric fields at E-region altitudes and the low latitude F-region electron density (Hagan et al., 2007). According to numerical simulations by Liu et al. (2010) the planetary waves can cause variations in the migrating and non-migrating tides through non-linear interactions which can be observed

at 100 to 250 km altitude and even extended to upper thermosphere. Moreover, planetary wave activity related to the lower atmospheric processes like the sudden stratospheric warming events (SSW) can modulate the tides.

1.10 Sudden stratosphere warming (SSW)

During the winter season of every year strong westerlies circle around the poles high in the stratosphere. These westerlies are called the stratospheric polar vortex which circulates around the cold polar air. They are formed due to radiative cooling and characterised by a band of strong winds from middle to high latitudes.
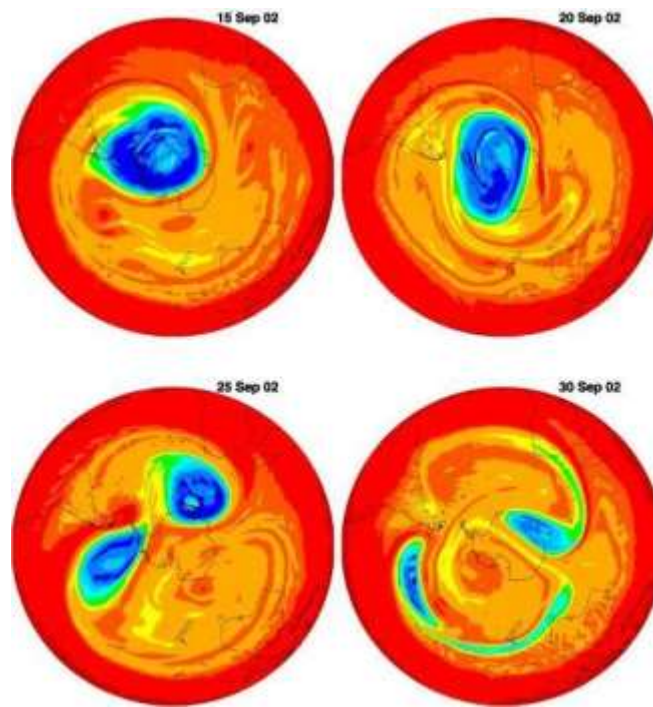
Figure 1.12: Potential vorticity on the 850 K isentropic surface for the southern hemisphere shown during September 2002 (Baldwin et al., 2003)

During SSW, these westerlies break down in few days due to their interaction with the planetary waves and are replaced by weak easterlies. The temperature of the polar stratosphere also gets increased up to around 50°C. The SSWs happen very rapidly i.e. within a few days and lasts longer in the lower stratosphere and troposphere than upper stratosphere. This could be due to faster radiative time scale in upper stratosphere (Baldwin et al., 2020).

Theses sudden changes in the polar stratosphere have its impact extended downward to the Earth's surface and upwards beyond the mesosphere. The amplitude of the planetary waves and climatology of the mean flow determines the likelihood of the occurrence of SSW during the winters. Prediction of SSW is possible prior to 10-15 days in advance (Tripathi et al., 2015; Domeisen et al., 2020a). Most of the SSWs have occurred in the northern hemisphere. The years 2002 and 2019 witnessed austral SSW although 2019 event cannot be categorized as a major one. The dramatic splitting followed by breakdown of the polar vortex during major austral SSW of 2002 is shown in Figure 1.12

SSWs are classified as major and minor depending on the reversal of the zonal winds from westerlies to easterlies and increase in the zonal mean temperature at 10 hPa at 60° latitude (Labitzke, 1981; McInturff, 1978). Quasi-stationary planetary scale waves cannot propagate into easterlies and hence the dynamical distinction between a major and a minor SSW is that the vertical wave propagation from the troposphere is restricted beyond middle stratosphere in case of a major event.

Apart from major and minor event there is classification based on the morphology of the event. During SSWs polar vortex can either be displaced off the pole or split into two pieces. Recent boreal SSW was observed in December 2020 – January 2021 which is shown in Figure 1.13.
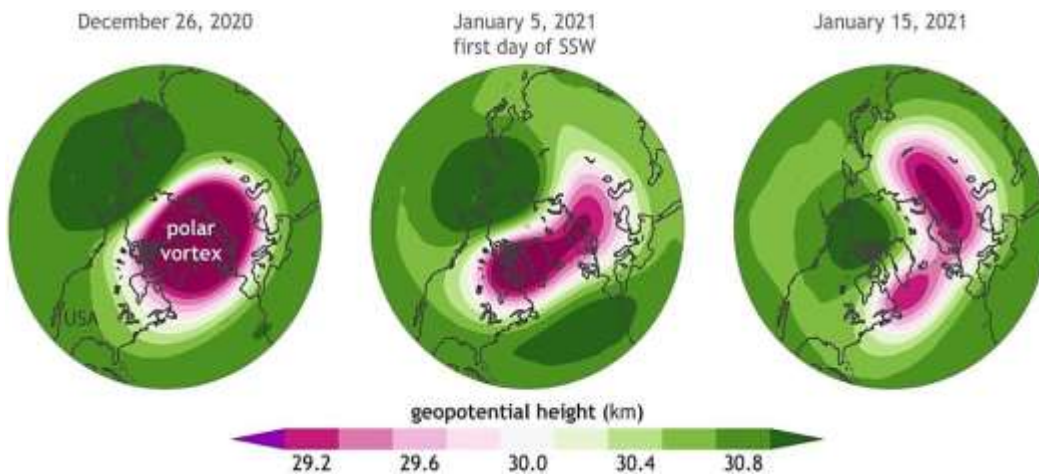
Figure 1.13: Disruption of the stratospheric polar vortex during boreal SSW of 2020-21 (L'Heureux, 2021)

Further, SSWs are also classified by the zonal wavenumber of the tropospheric precursor patterns leading to the same. Predominantly wave 1 and wave 2 patterns lead to the SSWs (Cohen and Jones, 2011). Mainly displacement of the vortex is always preceded by wave number 1 forcing and splitting of the vortex can be due to forcing by either wave number 1 or 2 (Bancala et al., 2012; Barriopedro and Calvo, 2014) and proceeded by wave number 1 increase with subsequent increase in wave number 2.

In northern hemisphere, the polar stratosphere variability peaks in January to March whereas; in southern hemisphere the variability peaks in September to November. In southern hemisphere, the warming inhibits strong heterogeneous ozone depletion and these events can affect jet streams, precipitation, especially across Australia (eg. Lim et al., 2019; Thompson et al., 2005).
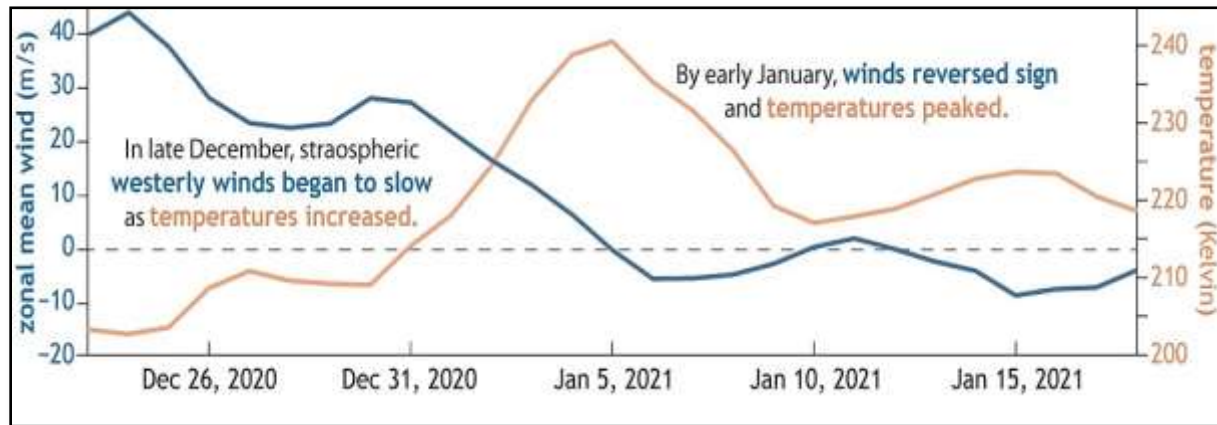
Figure 1.14: Evolution of zonal winds at 60°N and polar temperature difference (90°N-60°N) (L'Heureux, 2021)

They have impacts on the thermospheric chemistry, winds, electron densities and electric fields across both hemispheres (Chau et al., 2012). The boreal SSWs can be identified from zonal mean temperature difference between the latitudes (90°N-60°N) and zonal wind at 60° latitude. Recently the SSW has occurred in 2020-2021 (Lu et al., 2021) (shown in Figure 1.14).

1.11 Scope of the thesis

Ionospheric irregularities especially the F-region irregularities are widely studied since their discovery. They are usually observed during the post-sunset hours of solar maximum years. However, during June solstice of solar minimum years, the F-region irregularities are observed during delayed hours (around midnight hours) and are traditionally called the post-midnight F-region irregularities (PMF). The generation mechanisms of the post-midnight F-region irregularities are still not identified.

Gravity waves, Medium Scale Ionospheric Disturbances (MSTIDs) etc are considered to be the candidates for seeding the RTI. The uplifting of the F layer around midnight hours can aid in the growth rate of the RTI. At higher altitudes, the low ion-neutral collision frequency can increase the growth rate of the RTI. However what causes the lifting of the F layer during midnight hours needs to be addressed. Since the occurrence of PMF maximises during low solar activity years the lower atmospheric forcing on the F layer needs to be investigated for better prediction of the ionospheric conditions.

The objectives of the thesis are:

1. To study the occurrence characteristics of the post-midnight F-region irregularities over different longitudes
2. To investigate the lower atmospheric forcing through atmospheric tides on the post-midnight F-region irregularities (PMF)
3. To determine the impact of boreal and austral sudden stratospheric warming (SSW) events on the occurrence of the PMF
4. To understand the thermospheric conditions like the winds and vertical plasma drifts which could be favouring the generation of PMF

Chapter 2:

Data and methodology

2.1 Ionosonde

Ionosonde is high frequency (HF) radar which broadcasts a sweep of frequencies from 0.1 to 30 MHz vertically upwards and receives the reflected signal. The reflected signal is used to determine the electron density profile of the ionosphere. The refractive index of the ionosphere is proportional to the electron density and inversely proportional to the frequency of the radio wave. As ionisation varies with height so does the refractive index. Therefore, by broadcasting a band of frequencies and measuring the time taken by the signal to be reflected, the virtual height of the ionospheric layers can be determined. The signal is reflected when its frequency will match the plasma frequency which in turn is a function of electron density. The frequency at which the signal is reflected is called the critical frequency (f_c) of that layer.

$$f_c = 8.98\sqrt{N_e}$$

where f_c in Hz and N_e is number density of electrons in m^{-3}. All frequencies above the f_c will pass through the layer without reflection. Ionosphere is birefringent i.e. it has two refractive indices. Because of the geomagnetic field there will be two modes of reflection. The ordinary reflection will occur at the plasma frequency and for the extra-ordinary mode, the reflection will occur at a frequency which is higher than the normal plasma frequency by $\frac{1}{2}\times$ gyro frequency.

$$f_c = 8.98\sqrt{N_e} + 0.5 \times \left(\frac{eB}{m}\right)$$

The height we obtain from the time taken by the signal to be reflected is virtual height which will be higher than the real height of the ionosphere. The real height can be retrieved from the virtual height through true height analysis. The difference between the virtual height and the real height will be determined by the electron concentration through which the wave passes. The plot produced by the ionosonde is the ionogram with frequency on x axis and virtual height on y axis. From the ionogram, the critical frequencies and virtual height of each ionospheric layer can be manually scaled or SAO explorer software can be utilised for the same. Ionosonde observations

over Gadanki, Kototabang, Kwajalein Island, Ascension Island and Jicamarca are used for the study.

2.2 Equatorial Atmosphere Radar (EAR), Kototabang

EAR is a Doppler radar built for atmospheric observations in Indonesia. It was built in collaboration between the Research Institute for Sustainable Humanosphere (RISH), Kyoto University and the National institute of Aeronautics and Space of Indonesia (LAPAN). The radar have circular antenna with an approximate diameter of 110 m which consists of 560 three-element Yagi antennas. The EAR transmits radio signals at 47 MHz with output power of 100 kW and average power of 5 kW. It can observe winds and turbulence from 1.5 km to 20 km. Along with that, EAR is also designed to receive echoes from ~3 m (i.e. half radar wavelength) scale ionospheric irregularities (FAI echoes) in the E and F-region. The EAR has active phased array system which can steer the antennas electrically on a pulse-to-pulse basis. It can be operated in F-region mode with two set of eight beams that can scan pulse to pulse basis (Fukao et al., 2003) and have a single pulse range resolution of 75 m. The radar has the ability to steer the beam to 9 directions between ±54° in azimuth around geographic south (125°- 234°). Zenith angle lies between 20° and 35°. Here we have used F-region mode observations.

The presence of field aligned irregularities (FAI) can be identified from signal to noise ratio (SNR) > 0 dB extended for more than 50 km. The range time intensity (RTI) plots of the F-region are manually screened to check for the presence of the field aligned irregularities (FAIs). The radar beam steering capability will help in establishing the temporal and spatial evolution of the FAI echoes. The post-sunset F-region irregularities are identified as the FAI echoes observed between 18:00 LST and 22:00 LST. Sometimes these echoes can start between 18:00 LST and 22:00 LST and can be extended till early morning hours. The echoes which started to be observed after 22:00 LST and which are not extension of post-sunset echoes are considered as post-midnight F-region FAI echoes. The radar echoes are used to determine the percentage of occurrence (PO) of the post-sunset and post-midnight F-region irregularities. PO is calculated as number of quiet days (Ap < 12) when post-midnight F-region FAI echoes are observed divided by the number of quiet days when radar observations are available.

Figure 2.1: Equatorial Atmospheric Radar (EAR), Kototabang (https://www.rish.kyoto-u.ac.jp)

System specifications of the EAR radar are given in table 2.1 (Fukao et al., 2003, Otsuka et al, 2009).

Geographic latitude and longitude	0.2°S, 100.32°E, 865 m above sea level
Radar Operating Frequency	47 MHz
Antenna	Quasi-circular antenna array of 560 elements Yagi antennas
Aperture	110m in diameter
Beam Width	3.4°
Beam direction in azimuth	0-360° in 0.1°
Beam zenith angle	0-30° in 0.1°
Gain	33 dBi
Transmitter:	
Average Power	5 kW

Number of TR modules	560 units
Single TR module's power	180 W/unit
Pulse width	0.5 - 256 µs
IPP	200 µs - 10 ms
Receiver	
Type	Single super heterodyne
Noise Figure	5 dB
Typical F-region mode specifications:	
Inter pulse period	4 ms
No. of FFT points	128
No. of spectral average	3
No. of coherent integration	4

Table 2.1: Specifications of Equatorial Atmosphere Radar (EAR) Kototabang

2.3. Sounding of the Atmosphere by Broadband Emission Radiometry (SABER)

SABER is a space born radiometer onboard Thermosphere Ionosphere Mesosphere Energetics and Dynamics (TIMED) satellite launched on 7th December 2007 at an altitude of 625 km with an inclination of 74.1° and mean orbit period of 97 minutes (Dawkins et al., 2018). SABER can measure temperature and volume mixing ratio (VMRs) of ozone (O_3), carbon dioxide (CO_2) and water vapour (H_2O) from ~20 km to 150 km. Earth limb radiances at 15 µm and 4.3 µm of CO_2 are used to retrieve kinetic temperature. SABER temperature errors are in the range of 3.3-5.4 K in the height region of 80-100 km.

To extract the migrating and non-migrating tidal amplitudes the temperature data acquired by the SABER is used. The SABER gives temperature in the height region of 80 km–100 km. The temperature data are binned for every 10°. For example, temperature data are binned for 5°N – 15°N to obtain temperature at 10°N. The TIMED satellite covers all local time in 60 days. Hence, the temperature data for the 60 days are arranged in local time for the longitudes 0–30° E, 30–60° E, and 330–360°E to obtain 24 hourly values centered on 12 longitudes (15° E, 30° E, …, 345° E). It is subjected to space-time spectral analysis to obtain diurnal (24 hr), semidiurnal (12 hr), and ter-diurnal (8 hr) tides with zonal wavenumbers (s) −4, −3, −2, −1, 0, 1, 2, 3, and so forth by fitting the following expression:

$$\mathbf{A_{n,s}\,Cos(n\Omega t + (s - n)\lambda - \Phi_{n,s})}$$

where t is local time; n = 1, 2, 3 corresponds to subharmonics of tides with periods 24, 12, and 8 hr; s < 0 (s > 0) correspond to eastward (westward) propagating tides; and ϕ, λ, and Ω are phase, longitude, and angular frequency of Earth's rotation (Jones et al., 2013). The tides are referred to as migrating when s = n and non-migrating when s ≠ n. The 60 day window is moved further by successive days, and the procedure is repeated to get the variations of amplitudes of the migrating and non-migrating tidal components.

2.4. Michelson Interferometer for Global High-resolution Thermosphere Imaging (MIGHTI)

MIGHTI, an instrument onboard Ionosphere Connection Explorer (ICON) satellite gives the altitude profile of thermospheric winds and temperature. MIGHTI makes two perpendicular line of sight (LOS) measurements using Doppler shifts of two emission lines of oxygen – green (557.7 nm) and red (630 nm) from an inclination of ~27° at 600 km altitude covering 12°S to 42°N. The forbidden transitions from metastable states ^{1}D of excited O atoms are sources of these emission lines. The excitations of these atoms are due to dissociative recombination of the O_2^{+} to yield O^{+} and O (^{1}D) atoms (Bates, 1982; Link and Cogger, 1988). The Doppler Asymmetric Spatial Heterodyne (DASH) technique (Englert et al., 2017) is used to measure the Doppler shift in MIGHTI.

Measurements are available from 90 to 300 km except at ~109 km and ~209 km where there is a data gap at night time because air glow is dim or non-existent there. There are two orthogonal sensors: MIGHTI-A with 45° and MIGHTI-B with 135° in azimuth from the spacecraft velocity vector (Makela et al., 2021). MIGHTI-B observes the same region of the atmosphere 5-8 min after MIGHTI-A has observed it. It is assumed that the winds have not changed much during this short time. Each interferometer makes observations using both red and green oxygen emission lines day and night.   The daytime observations of the red line (630 nm) cover the altitude range of ~180 - 300 km whereas the green line (557.7 nm) observations cover an altitude of 90 to ~190 km. During night-time, the red line emission can span ~210 to 300 km altitude range and the green line can span 90 to ~109 km. The data from both sensors are combined to get the altitude profiles of zonal and meridional winds. Observations of the daytime and night-time are provided at a 30-s and a 60-s cadence respectively. Between 90 km and 170 km the MIGHTI wind measurements are available with vertical height resolution of 5 km and from 170 km to 300 km the height resolution increases to 30 km. The MIGHTI wind accuracy is found to be better than 5.8 m/s (green) and 3.5 m/s (red) (Harding et al., 2017). The vertical sampling of MIGHTI is 2.2 km at 300 km altitude.

The MIGHTI level 2.1 data products include the Line of Sight (LOS) thermospheric winds from each interferometer MIGHTI-A and MIGHTI-B. The level 2.2 data products of the MIGHTI combine the line of sight winds from both MIGHTI-A and MIGHTI-B and provide neutral wind vectors in both geographic and geomagnetic coordinate system (Makela et al., 2020).

2.5 Ion velocity meter (IVM)

IVM is an Ion Velocity Meter onboard ICON satellite which measures ion drift motions, ion density and temperature at 575 km. The IVM uses Retarding Potential Analyser (RPA) and Ion Drift Meter (IDM) (Heelis et al., 2017) with an accuracy of ~5 m/s.

The RPA has a sequence of grids which is stepped through sequence of potentials to determine the energy of the incoming ions. The current collected for single ion species is determined from equation:

$$I(\Phi) = qA_{eff} \frac{N_i}{2} V_r \left[1 + \text{erf}(\beta f) + \frac{1}{\sqrt{\pi}\beta V_r} \exp(-\beta^2 f^2)\right]$$

where A_{eff} is effective area of the collector, q is electron charge, **f** is average velocity of the ions reaching the collector, β is $\left(\frac{2KT}{m}\right)^{-(1/2)}$, V_r is the total velocity of the ions which will be sum of ambient ion drift (V_d) and spacecraft velocity (V_s) . φ is the potential of the grid as seen by the plasma and it is the sum of retarding potential with respect of ground R_v and sensor ground potential with respect to plasma ψ_s. The current measured will be the contribution from all the constituent ions. The current corresponding to the zero retarding potential will give the plasma density and least square fitting to the current–voltage characteristics will yield the bulk ion velocity as well as temperature.
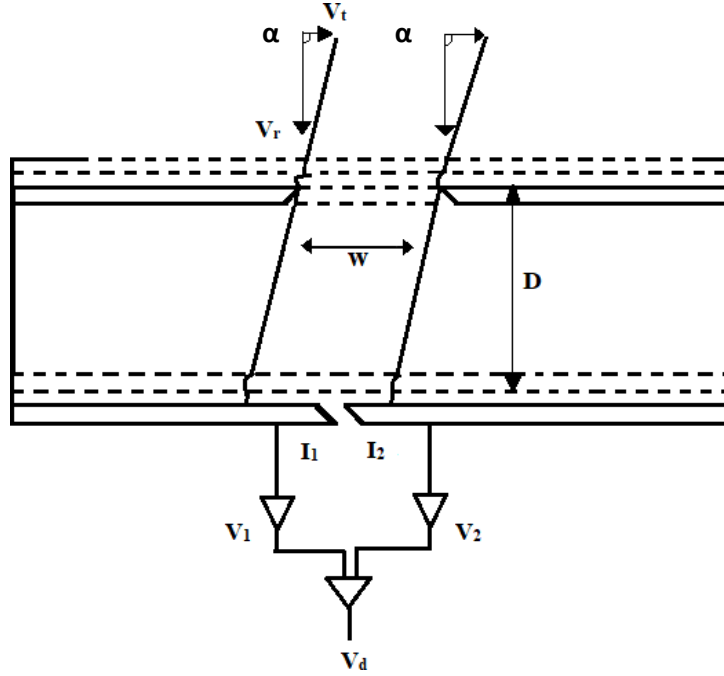
Figure 2.2: Ion beam trajectories and electronic configuration of IDM
(https://icon.ssl.berkeley.edu/Observatory/Instruments/IVM)

The IDM is a planar sensor that presents a square aperture to the incoming plasma that is intersected by a number of planar semi-transparent conducting grids and a solid segmented

collector (Figure 2.3). The IDM uses geometric relationship between the angle of arrival of the ion beam and the area illuminated and the current collected. The ratio of collector currents is proportional to the area illuminated which is given by the sensor dimensions and angle of arrival.

$$\frac{I_1}{I_2} = \frac{(w/2) + D\tan\alpha}{(w/2) - D\tan\alpha}$$

where W is the length of the square aperture, D is the depth from the external aperture face to the collector and α is the arrival angle of the plasma in one of these planes (Heelis et al., 2017). Hence, we can measure the arrival angle of ions from the ratio of currents. The corresponding drift velocity can be determined from the equation.

$$(\mathbf{Vd} + \mathbf{V\hat{s}}).\mathbf{t} = \sqrt{V_r^2 - \frac{2q\psi_s}{m}} \tan(\alpha)$$

 where t is the unit vector along the selected transverse direction.

The 'parallel' component of the ion drift velocity is parallel to the geomagnetic field, both 'meridional' and 'zonal' components are perpendicular to it. The meridional component of the drifts can be called as the vertical drifts. In magnetic meridian plane, the positive meridional component points to the zenith. The 'zonal' direction points towards magnetic east. Positive meridional direction mean upward vertical drifts and negative represents downward drifts. Similarly positive zonal drifts are eastward and negative drifts are westward.

2.6 NCEP Reanalysis winds and temperature

The NCEP/NCAR Reanalysis 1 project is using a state-of-the-art analysis/forecast system to perform data assimilation using past data from 1948 to the present (Kalnay et al., 1996). These data sets are available at the website of the Physical Sciences Division (PSD) of Earth System Research Laboratory (ESRL) in its original 4 times daily format and as daily averages at 17 pressure levels from 1000 hPa to 10 hPa. The present studies these data sets are used to identify the SSW events.
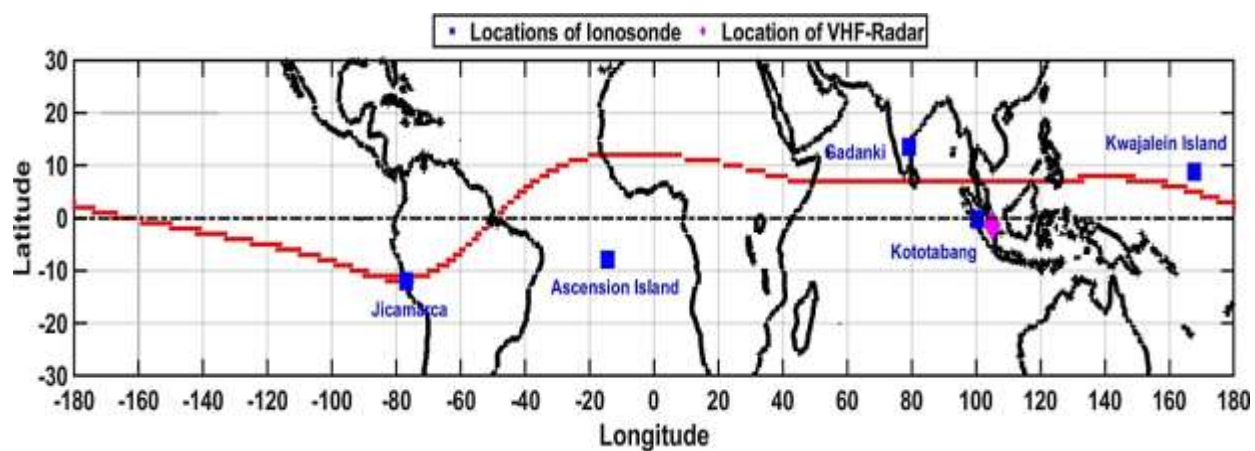
Figure 2.3: Map showing locations of Ionosondes and VHF radar which we have used for the study

Chapter 3:

Seasonal and solar activity variation in the percentage of occurrence of post-midnight F-region irregularities

3.1 Introduction

The low-latitude navigation and communication systems operating at low latitudes can be significantly affected by the plasma instabilities occurring in the F-region of the equatorial and low latitudes. These instabilities lead to the formation of plasma irregularities, also known as the equatorial plasma bubbles (EPBs). Plasma bubbles can exceed over 2000 km in altitude. Since their discovery by Booker and Wells (1938), these irregularities have been studied by various radio and optical techniques (see the review by Abdu, 2012, and references therein), as the presence of these irregularities can be identified in the VHF (Very High Frequency) radar echoes from the F-region field-aligned irregularities (FAIs) (e.g., Woodman and LaHoz, 1976) , in the airglow intensity variations (Sobral et al., 1980) and spread in the echoes of ionosonde (Spread-F). The density irregularities within the plasma bubbles have scale sizes between 10^{-2} to 10^{5} m (Tsunoda, 1980). These irregularities normally occur during post-sunset time. The well-accepted mechanism responsible for the generation of these plasma bubbles is the Raleigh-Taylor instability (RTI) over the dip equator after the sunset due to an increase in the eastward electric field called the pre-reversal enhancement (PRE). The PRE in the presence of horizontal magnetic field lifts the F-region to higher altitudes by **E×B** drift creating conditions favourable for the development of RTI. The magnitude of the PRE plays a key role in the generation of the plasma bubbles. The post-sunset F-region irregularities are common feature of equinox months of solar maximum years. The magnitude of the PRE maximises during equinox months of solar maximum years over longitudes with declination ~0⁰.

However, in recent solar minimum conditions, these irregularities have been observed in VHF radar observations during post-midnight hours (Otsuka, 2018; Otsuka et al., 2009; Patra et al., 2009) and also subsequently in Communications/Navigation Outage Forecasting System (C/NOFS) satellite observations (Li et al., 2011; Yizengaw et al., 2013). The occurrence

characteristics of post-sunset and post-midnight irregularities are different. The seasonal as well as solar activity variation of the post-midnight F-region FAI irregularities are determined from the backscattered echoes from Equatorial Atmosphere Radar (EAR) and spread–F from ionograms of ionosonde in Ascension Island and Jicamarca.

3.2 Data and Methodology

3.2.1 EAR F-region FAI echoes

The 47 MHz Equatorial Atmosphere Radar (EAR) in Kototabang, Indonesia (0.20°S, 100.32°E, dip latitude: 10.36°S; Declination ~0.18°W) is operated to study the F-region FAIs at ~3 m scale size during night-time (18:00–06:00 LST). The echoes observed after 22:00 LST is identified as post-midnight echoes (Review by Otsuka, 2012). The echoes that begin to occur just before midnight and continue beyond midnight are customarily identified as the post-midnight F-region FAI echoes. The FAI echoes are observed when the SNR is found to be > than 0 dB. The percentage of occurrence (PO) of post-midnight F-region FAI echoes are calculated as number of days when these echoes are observed divided by number of days when radar observations are available. Only geomagnetically quiet days ($A_p < 12$) are considered while calculating PO of post-midnight F-region FAI echoes.

3.2.2 Digisonde observations from Ascension Island and Jicamarca

The advanced digisonde portable sounder (DPS-4) at Ascension Island (Geographic: 8°S, 14°W; dip latitude 16°S; Declination ~14°W) and Jicamarca (11.95°S, 76.87°W, dip latitude: 1.10°N; Declination ~3°W) provides ionograms normally for every 15 minutes (Reinisch, 1996). These ionograms have been archived along with the scaled data (Reinisch and Huang, 1983) at the University of Massachusetts Lowell (UML) Digital Ionosonde Data Base. The scaled SAO and RSF data can be easily edited and analysed using the UML software system SAO. In the present work, the ionograms (.RSF format files) are screened manually to check for the presence of post-midnight spread-F in each day. When there is spread in the traces of ionograms after 22:00 LST it is considered to be post-midnight spread-F. The PO of post-midnight spread-F is calculated for geomagnetically quiet days ($A_p < 12$).

3.3 Results and discussions

3.3.1PO of post-midnight F-region FAI echoes over Kototabang

In order to see the seasonal variation exhibited by the post-midnight FAI echoes, the EAR F-region observations for the years 2011–2019 are used. The years are divided into solar minimum and solar maximum years based on the F10.7 cm solar flux. Figure 3.1a shows PO of post-midnight FAI echoes for years with annual solar flux unit (sfu = 10^{-22} Wm^{-2} Hz^{-1}) above 100, and this includes years from 2011 to 2015.
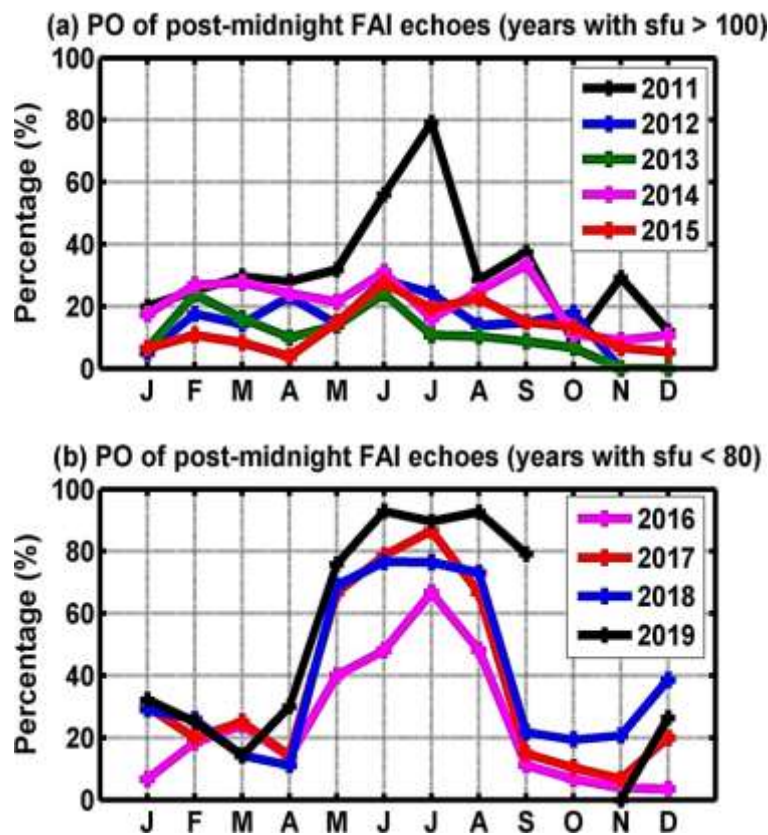
Figure 3.1: Percentage of occurrence of post-midnight F-region FAI echoes as observed by Equatorial Atmosphere Radar (EAR), Kototabang for years with (a) solar flux unit > 100 and (b) solar flux unit < 100

The year 2011 is a transition year from solar minimum to solar maximum with annual mean solar flux of 103 sfu. The PO of post-midnight FAI echoes in the year 2011 shows a large peak (79%) in the months of June and July. The pronounced maximum in June–July is absent in the years

2012–2015, when the solar activity is greater than 106 sfu. The PO in these years is less than 35% throughout the year.

The monthly variations of PO of the post-midnight FAI echoes for years with annual F10.7 cm solar flux below 80 sfu (2016–2019) are shown in Figure 3.1b. The years 2016, 2017, 2018, and 2019 have F10.7 cm solar flux values of 79.97, 69.81, 62.95, and 62.67 sfu, respectively. In the year 2016, the PO greater than 60% is observed only in July. However, in the years 2017–2019, high PO (>60%) is observed in the months of May–August. The high PO is extended to September in the year 2019, when it is 80%. September 2019 records a high PO, whereas it is less than 40% in the September month of other years. From both the Figures, it is evident that with decreasing solar activity, the maximum PO of the post-midnight F-region FAI echoes extends to nearby months (May, August, and September).

The PO of post-midnight F-region FAI echoes increases with decrease in solar activity during June solstice months (boreal summer months) over Kototabang which is a geomagnetically low latitude station. Moreover, the maximum PO of post-midnight FAI echoes gets extended from May to August with decreasing annual year solar flux. During nighttime of solar minimum years the ion-neutral collision frequency is found to decrease which can result in a positive growth in the RTI. The occurrence of the post-midnight F-region irregularities during quiet time solar minimum conditions ensures that the forcing can be of lower atmospheric origin which needs to be investigated further.

3.3.2. PO of post-midnight spread-F over Jicamarca

The monthly variations of the number of quiet days ($A_p < 12$) for which ionosonde observations are available over Jicamarca in the year 2019 are shown in Figure 3.2a. The Jicamarca ionograms are available for all the months. As the post-midnight spread-F (PMSF) normally evolves around midnight 22:00–03:00 Local Solar time, LST (Ajith et al., 2016), the spread-F is considered as post-midnight if it is formed after 22:00 LST and it should not be the continuation of the post-sunset spread-F (PSSF). Monthly variations of the percentage of occurrence (PO) of post-sunset spread-F (18:00–22:00 LST) over Jicamarca (PSSF-JIC) and post-midnight spread-F (22:00–06:00 LST) over Jicamarca (PMSF-JIC) in the year 2019 are shown in Figure 3.2b. The

PO of PSSF-JIC is found to be more as compared to PMSF-JIC during the months of January-March and August-December. The maximum PO of PMSF (56%) is found in July. The PO of the PSSF is observed to be above 80% in January, September, November and December. Minimum PO of PMSF (3.7%) is found in March. Jicamarca is a dip equatorial station where the PO of post-midnight F-region irregularities maximises during June solstice months of solar minimum years and PO of post-sunset F-region irregularities maximises in equinox months.
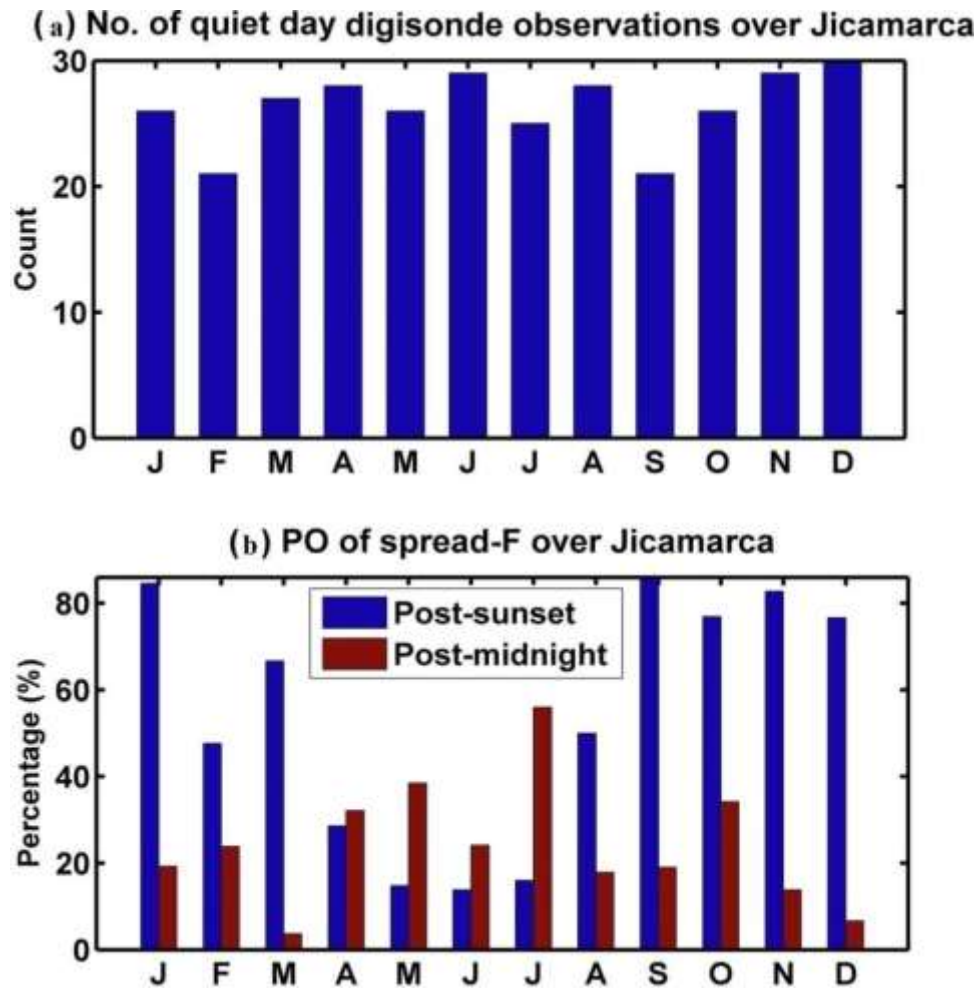
Figure 3.2: (a) No. of quiet days (Ap < 12) for which the digisonde observations over Jicamarca are available; (b) The percentage of occurrence (PO) of the Post-Sunset (18:00–22:00 LST) and Post-Midnight (22:00–06:00 LST) spread F over Jicamarca respectively for the year 2019.

3.3.3 PO of post-midnight spread-F over Ascension Island

The ionograms are manually screened to determine the occurrence of post-midnight spread-F during quiet days ($A_p < 12$) of the solar minimum years 2008, 2010, 2019 and 2020 with annual mean solar flux units (sfu) 62.003, 71.8291, 62.73 and 66.355 respectively. Ionosonde observations over Ascension Island are available only for these years.
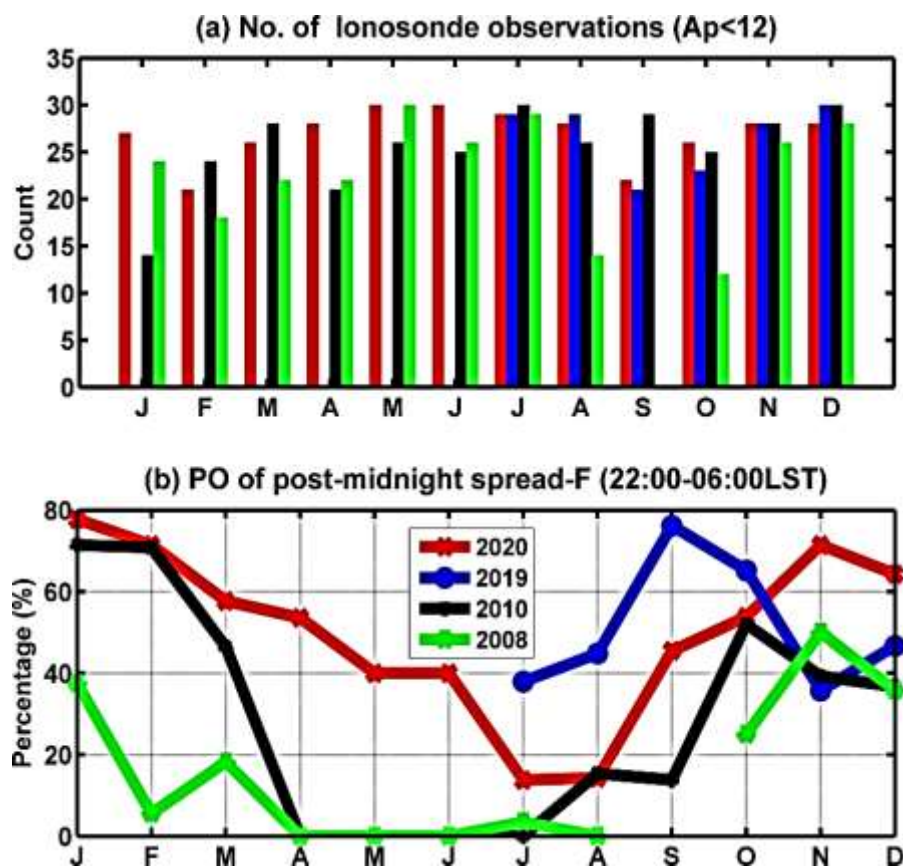
Figure 3.3: (a) Monthly variation of the number of quiet days ionosonde observations available over Ascension Island (8°S, 14°W, dip latitude: 16°S) for each month of the years 2008, 2010, 2019, 2020 and (b) Monthly variation of the Percentage of occurrence of post-midnight spread-F

Figure 3.3a shows the number of quiet days ($A_p < 12$) in each month for which the digisonde observations are available for the low solar active years 2008, 2010, 2019 and 2020. The observations are available for most of the months of 2020 and 2010. Almost all the months have

more than 50% of observation days except during August-October of 2008. There is no RSF data available during January-June, 2019. Fig. 3.3b shows PO of post-midnight spread-F. During all the years, the PO is found to be more during January-March and October-December which include local summer months (since Ascension Island is located in the southern hemisphere). Among them, the PO is a maximum of 77.5% in January and 71% in February and November 2020. The years 2008 and 2010 record the lowest PO (0%) in April-August. Besides, in the years 2008 and 2010, the PO is the lowest from April to September compared to other months of the respective years. The highest PO in the year 2010 is in January (71%) but the number of observations available is only for 14 days.

From these results, we can infer that the post-midnight spread F consistently shows maximum PO over Ascension Island during local summer (November to February) and fall equinox. Particularly, it is higher (>70%) during November-December 2020. For the years 2008 and 2010 shown in the Figure 3.3b, the PO is found to be less than 35%. In 2019, maximum PO (76%) is observed in September and another maximum of 65.22% is found in November. The PO in November and December 2019 is 35% and 46% respectively. In the year 2008, the PO is 40% and 39.28% in November and December respectively. In 2010, the PO is 40% and 39.28% in November and December respectively. However, it is found that the occurrence of the post-sunset spread F is less over Ascension Island and it does not show any clear seasonal variation. Ascension Island has negative declination hence, PO of the F-region Irregularities maximises during December solstice months when the solar terminator is parallel to the geomagnetic field lines.

In the northern and southern hemisphere over the dip equator and geomagnetically low latitudes the post-midnight F-region irregularities have their maximum occurrence during June solstice of solar minimum years. It is already reported that over Jicamarca (11.9515° S, 76.8744° W, 0.6°S dip), Kototabang (0.20°S, 100.32°E, dip latitude:10.36°S) and Gadanki (13.4593°N, 79.1684°E, dip latitude: 6.3°N) the PO of post-midnight F-region irregularities are maximum in June solstice months of solar minimum years.

3.4 Summary and Conclusions

1 Seasonal variation of the post-midnight F-region FAI echoes observed by EAR shows that their maximum occurrence rate is in June solstice months (boreal summer months).

2 Solar activity has indirect relationship with the post-midnight F-region FAI echoes. Solar minimum years (sfu < 103) have large PO of post-midnight F-region FAI echoes compared to the years with solar flux unit greater than 103.

3 Over Jicamarca, a dip equatorial station, the PO of post-midnight spread-F maximises during June solstice months and post-sunset spread-F maximises during equinox months.

4 Over Ascension Island, a station with westward magnetic declination, ionosonde observations have shown that the PO of post-midnight spread-F is maximum during November to February months (austral summer months).

Chapter 4:

Tidal influence on the generation of post-midnight F-region irregularities

4.1 Introduction

The F-region Irregularities are manifestations of Equatorial Plasma Bubbles (EPBs). These irregularities are aligned in the direction of the magnetic field line extending from hundreds to thousands of kilometers. As these field aligned irregularities (FAIs) can strongly backscatter radio waves and cause variations in the airglow intensities (Sobral et al., 1980 and Woodman and LaHoz, 1976), their characteristics and variabilities have been studied by both radio and optical techniques. These studies reveal that the occurrence of these irregularities is normally during the post-sunset time. The Rayleigh-Taylor Instability (RTI), generated over the magnetic equator after sunset, due to the intense eastward electric field (PRE) is the generally accepted mechanism for the generation of the post-midnight F-region irregularities. They also show seasonal variation with their preferential occurrence during equinox months and further their occurrence increases during highsolar activity years.

These irregularities have recently been observed during the post-midnight hours in the VHF radar (Patra et al., 2009; Otsuka et al., 2009) and C/NOFS satellite observations (Li et al., 2011; Yizengaw et al., 2013) with characteristics quite different from the post-sunset irregularities. Unlike the post-sunset irregularities, the occurrence rate of these post-midnight irregularities maximises during May-August of solar minimum years over equatorial and low latitude regions (shown in Chapter 1). Longitudinal variation of these irregularities shows maximum occurrence over the African sector (Yizengaw et al., 2013). These echoes normally evolve around midnight 22:00–03:00 Local Solar time (LST) (Ajith et al., 2016).

Several causative mechanisms have been proposed for the occurrence of this post-midnight F-region FAI echoes. Atmospheric gravity waves can act as a seed for the instability. They can

cause ion-neutral collisions and eventually generates polarization electric field in the F-region which can initiate the RTI (Huang and Kelley, 1996). South-westward traveling ionospheric disturbances (TIDs) generated by Perkins instability are accompanied by polarization electric fields to maintain the divergence free currents and these polarization electric fields can also provide necessary seeding perturbations for the RTI to develop (Miller et al., 2009; Takahashi et al., 2018). However, these electrified TIDs do not always reach the dip equator as their equatorward boundary is crest anomaly latitudes. Poleward moving TIDs have often been observed over Kototabang but these TIDs could not accompany polarization electric fields (Shiokawa et al., 2006). The day to day variability in the post-midnight F-region irregularities can be attributed to the seeding mechanisms.

During night-time of solar minimum years the ion-neutral collision frequency (v_{in}) is low which can lead to positive growth of the RTI. The v_{in} value also decreases with increasing height of the F layer. Hence, the altitude of the F layer plays a key role in their generation. The updrift of the F layer can be caused by the magnetically equatorward winds associated with midnight temperature maxima (MTM) in thermosphere resulting from atmospheric tides (Candido et al., 2019; Maruyama, 1996). The occurrence of these PMF during solar minimum years suggests that the lower atmosphere play a significant role in their generation.

The ionospheric variabilities during geomagnetically quiet time conditions can be attributed to the perturbations originating from the lower atmosphere (Chen, 1992, Rishbeth and Mendillo, 2001). These perturbations can be planetary waves, atmospheric tides and gravity waves. The vertical propagation of tides into the upper atmosphere can cause significant variabilities in the ionosphere (Lastovicka, 2006). The tides are the major driving forces behind the E-region dynamo mechanism as well (Richmond, 1983). Immel et al. (2006) have shown that longitudinal variations in the F-region electron density exhibit wave number 4 structure which is signature of diurnal eastward propagating wave number 3 non-migrating tide (Hagan et al., 2009) .

To study the impact of atmospheric tides on the F-region irregularities particularly, the post-midnight F-region irregularities, the tidal variabilities of solar minimum year and corresponding PO of post-midnight F-region FAI echoes are investigated.

4.2 Data and Methodology

4.2.1 F-region observations from EAR Kototabang

The F-region FAI radar echoes from 47 MHz Equatorial Atmosphere Radar (EAR) in Kototabang, Indonesia (0.20°S, 100.32°E, dip latitude: 10.36°S) are used to determine PO of the F-region Irregularities. The PO of post-midnight F-region irregularities are calculated only for quiet days ($A_p < 12$) in similar way as mentioned in Chapter 3.

4.2.2 TIMED-SABER temperature

SABER temperature observations of the year 2011 are utilised to extract the tidal amplitudes by method specified in section 2.3.

4.2.3 Digisonde observations from Kwajalein Island

In this study, the digisonde observations over Kwajalein Island (9°N, 167.2°E, 3.8°N dip) for the year 2011 obtained from the ftp site: ftp.ngdc.noaa.gov are used. The advanced DPS-4 operated at Kwajalein is programmed to make one ionogram in every 15 min. The scaling is done by using SAO explorer software package (http://umlcar.um.edu), which provides the vertical electron density profile, and various ionospheric characteristics like the peak plasma frequency (foF_2) and peak height (hmF_2) of the ionospheric F_2 layer (Reinisch et al., 2005). The Kwajalein Island data are selected, because the site is an equatorial station close to Kototabang, where continuous observations for the year 2011 and for the solar minimum year 2009 are available.

4.3 Results and Discussions

4.3.1 F-region FAI radar echo occurrence over Kototabang during 2011

Figure 4.1 shows the number of days for each month when the F-region observations by the EAR are available and the percentage of occurrence (PO) of post-sunset and post-midnight F-region FAI radar echoes.
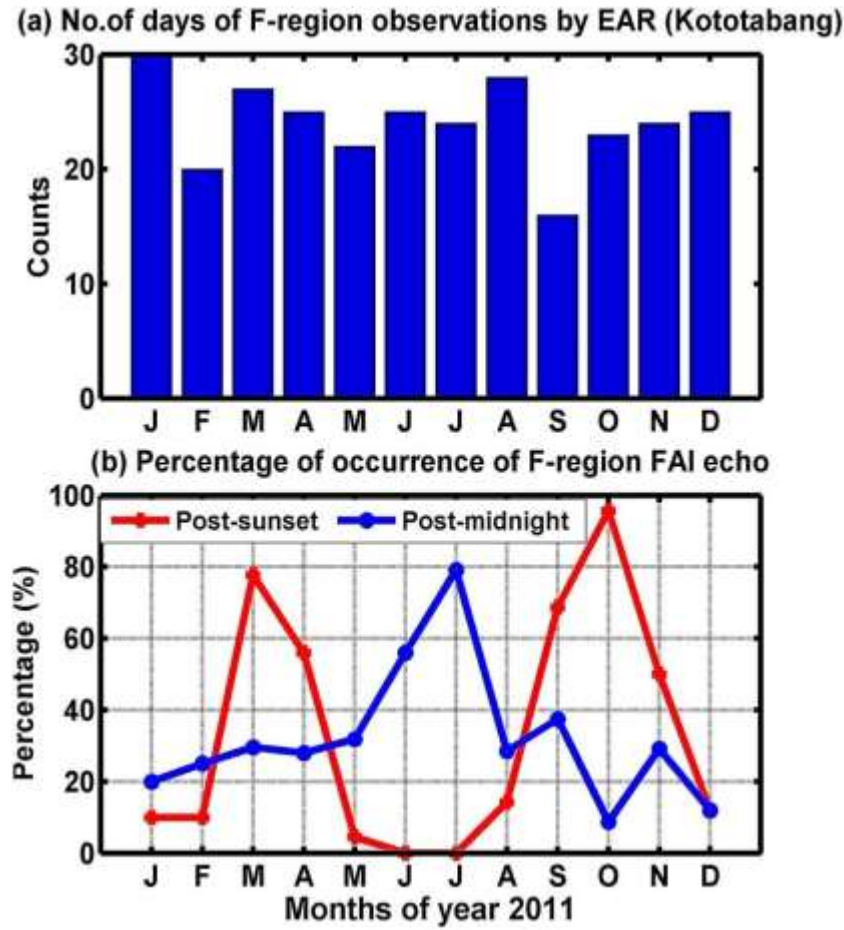
Figure 4.1: Percentage of Occurrence (PO) of post-sunset and post-midnight F-region FAI echoes as observed from EAR Kototabang

The year 2011 is selected, as the EAR F-region observations are available for all the months and it is close to the 24th cycle of the solar minimum year 2008. The Range Time Intensity (RTI) plots of the EAR observations are manually screened to check for the presence of the F-region irregularities.

The PO of the post-sunset echoes is the highest in March (78%) and October (96%). More than 50% occurrence is observed in April (56%) and September (65%). The post-midnight F-region radar echoes maximizes in June and July with PO of 56% and 79%, respectively. Its occurrence rate reduces to 28% in August. However, it increases again to 43% in September. Unlike the post-sunset echoes which are confined mostly to equinox months, the PO of post-midnight echoes is greater than 25% in most of the months (February–September and November). Low

46

PO of post-midnight echoes is noted in December and January. From the Figure, we can infer that the post-sunset echoes have semi-annual variation with maxima in equinox months and the post-midnight echoes have maximum occurrence during June solstice months of 2011.

4.3.2 Tidal variations during the year 2011
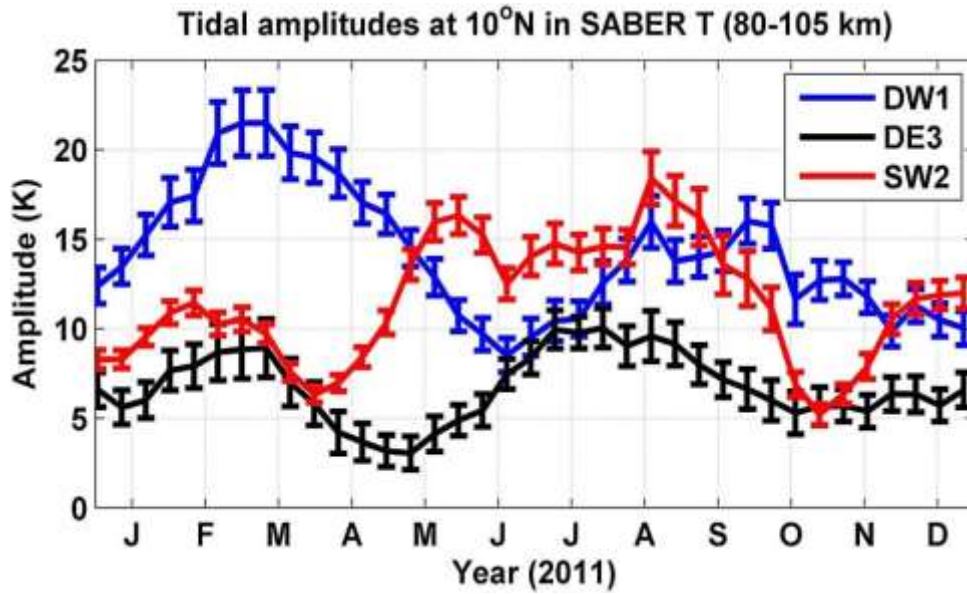
Figure 4.2: Time variations of DW1, DE3, and SW2 tidal amplitudes averaged for the heights 80–105 km at 10°N in TIMED-SABER temperature at the intervals of 10 days. The ticks in the *x* axis represent the center of the particular month

Figure 4.2 shows daily variations of westward propagating migrating diurnal tide with zonal wavenumber k = 1 (DW1), eastward propagating non-migrating diurnal tide with k = 3 (DE3), and westward propagating migrating semidiurnal tide with k = 2 (SW2) in TIMED-SABER temperature at 10°N (dip equator passes at 10°N over Kototabang) averaged for 80–105 km.

The diurnal tide shows semi-annual variation with maximum amplitudes of 22 K in February–March and 14–16 K in August–September months. The SW2 tidal amplitude shows a broad maximum during summer months from May to mid-September, and it is larger than DW1 in these months. The DE3 amplitude is comparable to DW1, particularly in July.

4.3.3 The hmF$_2$ variations during the year 2011
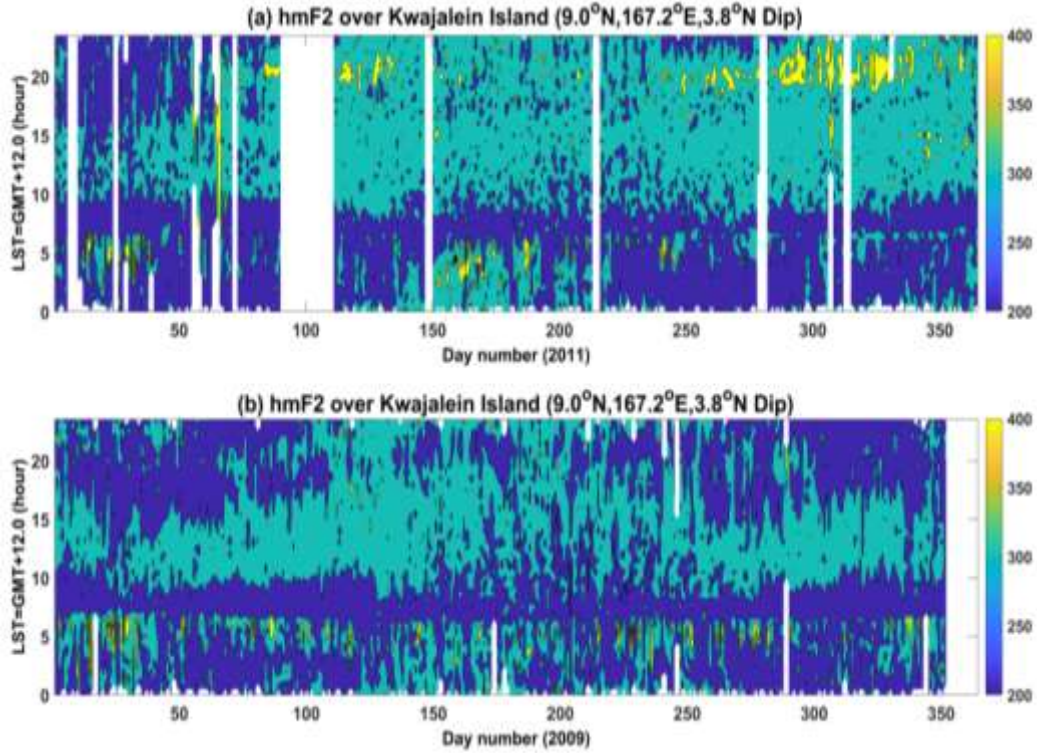
Figure 4.3: Local time variation of hmF$_2$ over Kwajalein Island for the years 2011 (a) and (b) 2009

The local time variation of daily peak F-region height (hmF$_2$) over Kwajalein for the year 2011 is shown in Figure 4.3a. From the figure, we can infer that the hmF$_2$ is at higher heights (greater than 350 km) during days 80–130 and 250–334 at 20:00 LST. There are data gaps around days 90–110. However, the hmF$_2$ is found to be at heights greater than 300 km during midnight and early morning hours during days ~120–240 (May–August).

In most of the days during equinox and winter months, hmF$_2$ is at heights around 200–250 km only after midnight. In order to check the consistency, the hmF$_2$ for the solar minimum year 2009 is shown in Figure 4.3b. Unlike the moderate solar active year 2011, the higher hmF$_2$ during evening hours in the equinox months is absent in the year 2009. The hmF$_2$ is at higher heights during midnight and early morning hours during May–August.

48

Figure 4.4 shows the seasonal variation of the hmF_2 at midnight hours. Each dot in the figure represents hmF_2 over Kwajalein Island, and the red curve shows the 30 day running average of the hmF_2. The 30 day mean hmF_2 shows values higher than 300 km during days 118–238 with a maximum around day 170. At 01:00 LST, it is reduced to days 138–209. However, during solar minimum year shown in Figures 4.4c and 4.4d, the hmF_2 is at heights greater than 300 km for an extended period (days 109–259) at 23:00 LST and days 109–268 at 00:00 LST.
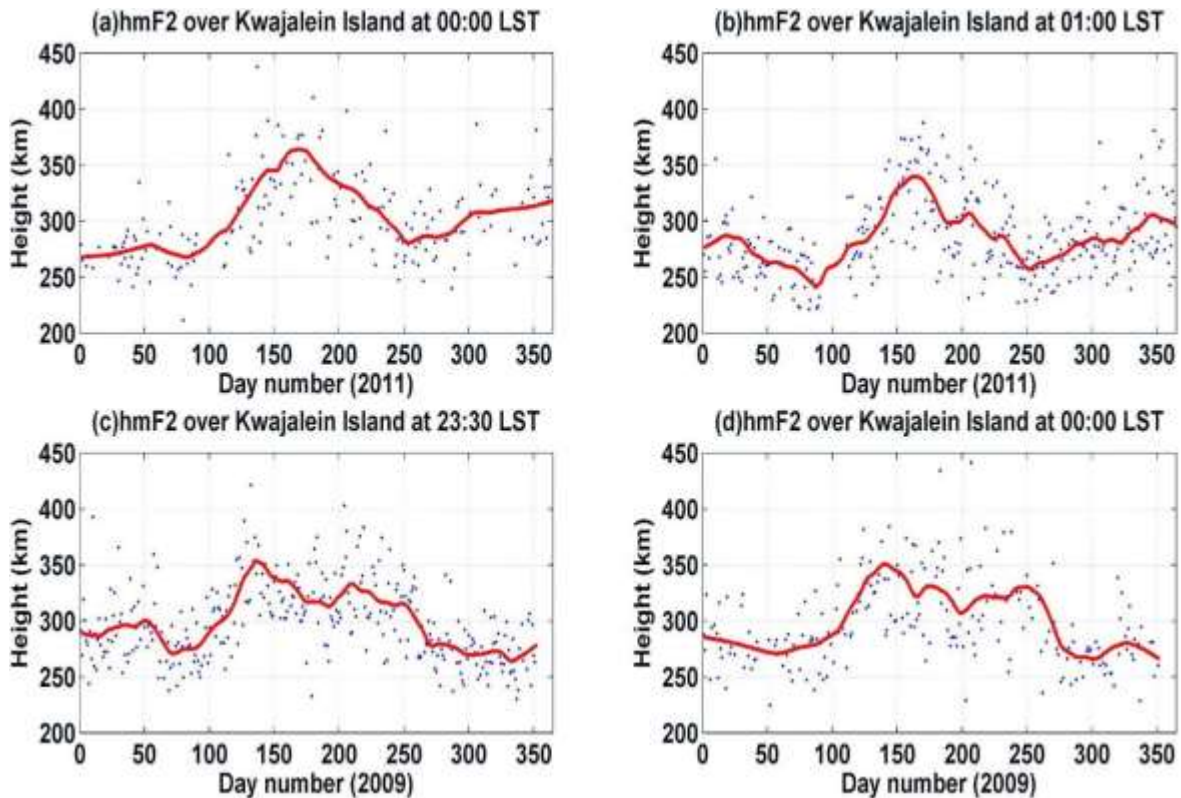
Figure 4.4: Seasonal variation of hmF_2 over Kwajalein Island at midnight hours for the years 2011 and 2009. Each dot in the Figure represents the hmF_2 variation, and the red curve shows the 30 day running mean of hmF_2

Figure 4.5 depicts the seasonal variation of the hmF_2 at evening hours 18:30 and 19:30 LST for the years 2011 and 2009. In the year 2011, the hmF_2 at both 18:30 and 19:30 LST shows semi-annual variation with higher values around days 67–134 and 112–149, whereas in the year 2009, the semi-annual variation of hmF_2 is not prominent. In the year 2009, the 30 day running mean of hmF_2 is slightly larger than 300 but less than 350 during days 100–300.

The EAR observations over Kototabang are used to study the possible migrating semidiurnal tidal influence on the post-midnight F-region FAI radar echoes. It is found that the post-midnight echoes show a high PO during June–July of low solar activity years. Patra et al. (2009) first observed the post-midnight FAI echoes in the VHF radar observations at Gadanki (13.5°N, 79.2°E) in June.
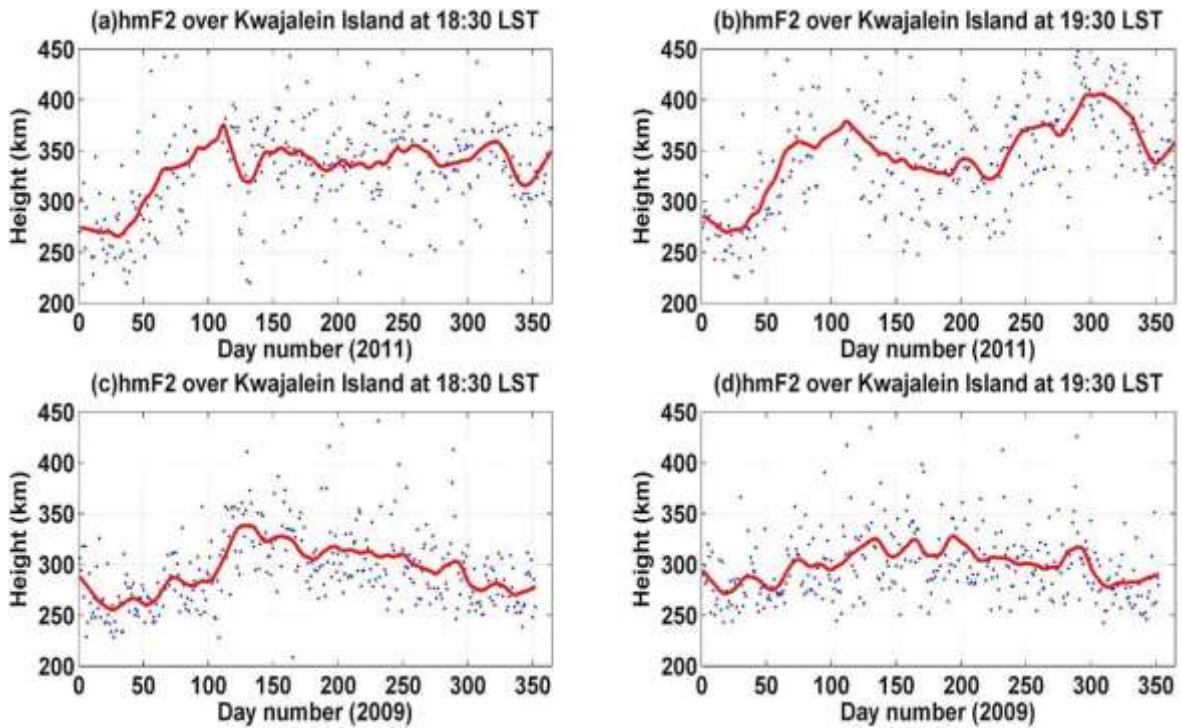
Figure 4.5: Seasonal variation of hmF$_2$ over Kwajalein Island at evening hours for the years 2011 and 2009. Each dot in the Figure represents the hmF$_2$ variation, and the red curve shows the 30 day running mean of hmF$_2$

Subsequently, the post-midnight echoes have been reported by Otsuka et al. (2009) over Kototabang. Li et al. (2012) observed post-midnight FAIs by VHF radar at Hainan, China, in June of 2009–2010. Nishioka et al. (2012) reported that both post-midnight FAIs and uplift of the F layer frequently occur around midnight between May and August over the dip equatorial station Chumpon, Thailand. They also clearly showed that the peak altitude of F$_2$ layer from ionosonde measurements, reaches higher heights after post-sunset during the equinox months and after post-midnight hours in May–August, which is consistent with the maximum occurrence of post-sunset spread F during equinox and post-midnight FAI echoes in May–August.

The present study also shows that the hmF_2 shows semi-annual variation with higher heights during equinox months at post-sunset hours and they show annual variation with higher heights during June solstice. The tidal variabilities show that the westward propagating migrating semidiurnal tide with zonal wavenumber(k) 2 (SW2) exhibits larger amplitudes during June–July and it has larger amplitudes than westward propagating migrating diurnal tide of zonal wavenumber 1 (DW1).

This indicates that the migrating semidiurnal tide plays a major role in the occurrence of post-midnight spread F. Stoneback et al. (2011), using C/NOFS observations during December 2008 to January 2009, found strong semidiurnal variation in the average $\mathbf{E} \times \mathbf{B}$ drift and concluded that such a variation could be responsible for upward drift near midnight, consistent with the post-midnight occurrence of F-region irregularities reported.

The dependence of solar cycle and seasonal variations of post-midnight spread F reveals its possible relationship with the MTM, which exhibits similar characteristics (Niranjan et al., 2006; Yizengaw et al., 2013). Akmaev et al. (2010) suggested that the MTM could be due to tides. Herrero and Spencer (1982) indicated that the thermospheric tidal winds converging around the equator can cause MTM through adiabatic heating. Fesen (1996) pointed out that the maximum occurrence of MTM during summer can be due to the interaction of semi-diurnal tidal modes (2, 2) and (2, 3). These results suggest that the semi-diurnal tides can play a vital role in the formation of the post-midnight FAI echoes as well as MTM.

As the semi-diurnal tide has a larger vertical wavelength, it can reach thermosphere without much attenuation (Truskowski et al., 2014) and can cause semi-diurnal variation in the electric field through dynamo mechanism thereby making conditions favourable for the lifting of F layer to higher heights, which may lead to PMF around midnight hours.

4.4 Summary and Conclusions

It can be summarized that:

1   The migrating semidiurnal tidal amplitudes (SW2) are larger than the migrating diurnal tide (DW1) during June–July when the PO of the post-midnight F-region FAI echoes is maximum.

2   The ionosonde observations over Kwajalein Island (9°N, 167.2°E, dip latitude: 3.8°N) reveal that the F-region is lifted to higher heights during midnight and early morning hours in May–August months.

3   This study clearly reveals the dominant role of migrating semidiurnal tide in causing the post-midnight FAI echoes. It is suggested that the dominant semidiurnal variation of the zonal electric field can become eastward at delayed hours (midnight hours) and lift the F layer to the higher heights creating favourable conditions for the growth of the RTI at a later time causing delayed F-region irregularities around midnight.

Chapter 5:

Boreal Sudden Stratosphere Warming (SSW) impact on the post-midnight F-region irregularities

5.1 Introduction

In Chapter 3 and Chapter 4, the occurrence characteristics of the post-midnight and post-sunset echoes over Kototabang are presented and related them with the equinoctial and local summer maximum exhibited by the migrating diurnal and semi-diurnal tides respectively. Furthermore, the peak height of the F_2 layer (hmF_2) exhibits equinoctial maxima during the post-sunset hours and summer maxima during the post-midnight hours, which coincide with the occurrence characteristics of the PSSF and PMSF (Nishioka et al., 2012).

The occurrence rate of post-midnight echoes due to spread F is normally less during the boreal winter (December-January). However, Patra et al. (2014) observed frequent occurrence during the boreal sudden stratospheric warming (SSW) of 2009 and suggested it could be due to the semi-diurnal variation in the electric field. The SSWs are dynamic processes characterized by rapid temperature increases in the winter high-latitude stratosphere, disruptions to the polar vortex, and decelerations or reversals of the stratospheric zonal winds (Goncharenko et al., 2021). The current state of understanding about the mechanisms driving SSWs is discussed in review by Baldwin et al. 2021. The SSW event usually occurs on an average about 6 to 7 times in a decade (Liu et al., 2019, Rao et al., 2019) in the northern hemisphere. Studies have been conducted to understand the equatorial and low latitude ionospheric effects during SSW. The equatorial electric fields, total electron content (TEC) and electron density profiles are observed to be modified during SSW. The semi-diurnal (SW2) tidal enhancement is observed during SSW which can be due to increase in the ozone concentration (Sridharan et al., 2009).

In Chapter 4, the increase in the amplitude of the SW2 and maximum percentage of occurrence (PO) of the post-midnight F-region irregularities are observed to be coinciding in June solstice months of solar minimum years. The impacts of mesospheric tidal variabilities related to boreal SSW on the occurrence of PMSF are presented in this chapter.

The digisonde observations over Gadanki, EAR F-region observations and SABER temperature observations during boreal SSW are utilised for determining the impact of boreal SSW on the tides and the F-region irregularities.

5.2 Data and Methodology

5.2.1 EAR Kototabang F-region FAI echoes

In the present study, the occurrence of F-region FAI is inferred from the backscattered signal-to-noise ratio (SNR) measured by the EAR. PO of the post-midnight F-region FAI echoes are determined from EAR observations similar to Chapter 3 and 4. It may be noted that the dip equator is passing $\sim10°N$ (geographic) over the Southeast Asian sector.

5.2.2 Digisonde observations from Gadanki

Digisonde observations from Gadanki (13.5°N, 79.2°E geographic; dip latitude of ~6.5°N) are utilised during December 2018–January 2019 when a boreal SSW has occurred. Ionograms are available for every 3 min intervals. The hmF_2 and hpF are analysed during this duration. The ionograms are manually screened to check for the presence of spread-F.

5.2.3 TIMED-SABER temperature

The global temperature data acquired by the SABER instrument on board the polar orbiting TIMED satellite have been used to obtain the amplitudes of both migrating and non-migrating tides (Russell et al., 1999). The methodology to determine the tidal amplitudes is described in the section 2.2.2. Semi-diurnal tide (SW2) and diurnal tidal (DW1 and DE3) amplitudes are extracted from the SABER temperature.

5.2.4 NCEP Reanalysis winds and temperature

In the present work, the reanalysis winds and temperature are used to infer the state of polar stratosphere particularly to identify SSW events.

5.3 Results and Discussions

5.3.1 Post-midnight F-region FAI radar echoes during boreal SSW 2018–2019
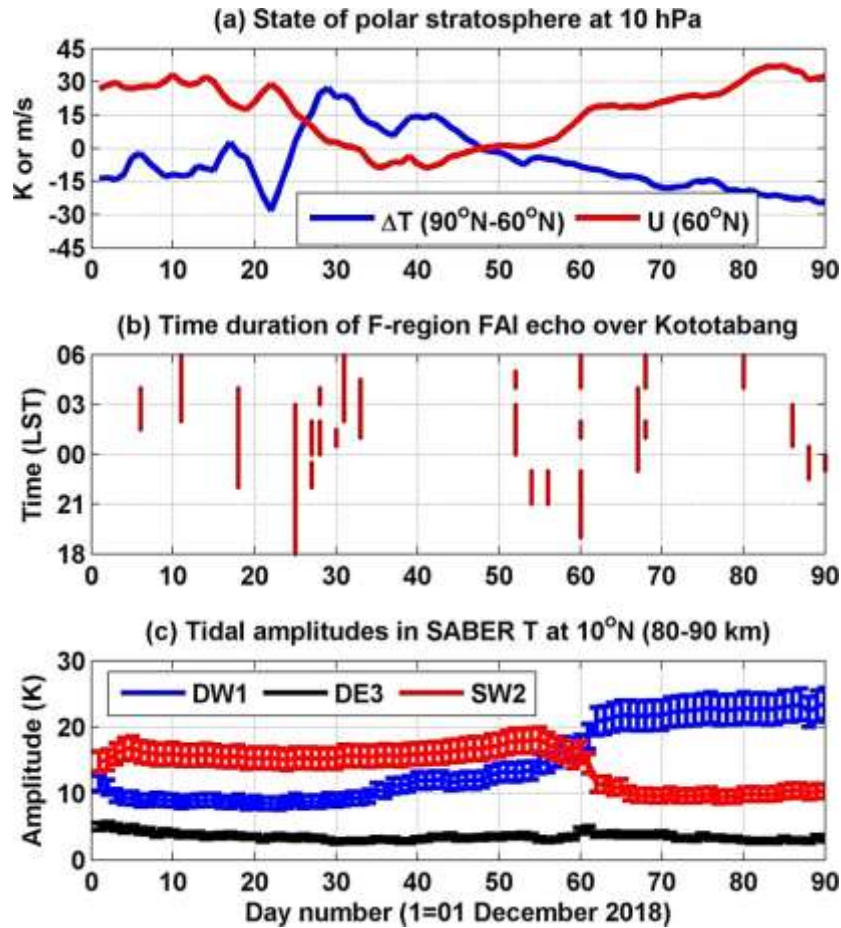
Figure 5.1: (a) State of polar stratosphere at 10 hPa to identify the SSW event from the positive polar temperature difference between 90°N and 60°N and from the westward winds, (b) time duration of F-region FAI echo occurrence over Kototabang, and (c) daily variation of DW1, SW2, and DE3 tidal amplitudes in TIMED-SABER temperature at 10°N averaged for the heights 80–90 km for 90 days starting from 1 December 2018.

Figure 5.1a shows the daily variation of zonal mean temperature difference between the pole and 60°N, zonal mean temperature, and zonal wind at 60°N for the period 1 December 2018 to 28 February 2019. The occurrence of the SSW event during 25 December 2018 to 16 January 2019 (days 25–47) can be inferred from the positive temperature difference between 90°N and 60°N and the deceleration of zonal mean zonal wind on 25 December 2018 and its subsequent reversal to westward flow (major SSW event) that lasts till 16 January 2019. The peak positive

temperature difference of 27 K and the peak westward wind (−10 m/s) are observed on days 27 and 41, respectively. Figure 5.1b shows the duration of the occurrence of F-region FAI radar echoes over Kototabang from 1 January 2018 to 28 February 2019. It reveals that the post-midnight echoes occur on 6, 11, and 18 of December 2018. The echoes occur nearly continuously on 25, 27, 28, 30, and 31 December 2018 and 2 January 2019. After this, the echo occurrence is observed only on 21 January 2019 (day 52).

Figure 5.1c shows the daily variation of tidal amplitudes at 10°N averaged for the heights 80–90 km in TIMED-SABER temperature. The SW2 tide shows larger amplitudes than diurnal tide until day 35. After day 35, though SW2 shows larger amplitudes, the DW1 amplitudes are also comparable. After day 56, the DW1 amplitudes become larger than those of SW2. The DE3 tidal amplitudes are much smaller than both SW2 and DW1 throughout the period shown in the Figure 5.1c. Note that the daily tidal amplitudes are estimated from the 60 day temperature data at 10°N arranged in local time centered on each day, and hence, it gives only a broad picture of variation of tides, and it does not represent day to day tidal variabilities.

5.3.2 Tidal variabilities during the 2008 and 2009 SSW events

The unprecedented SSW of January 2009 and a minor SSW event of 2007 are considered to check the consistency of the tidal variabilities. Figure 5.2 shows the state of the polar stratosphere and the tidal variabilities (DW1, SW2, and DE3) for the winters 2008–2009 and 2007–2008. During 2008–2009, the occurrence of SSW event is noticed during days 54–58. The deceleration of the wind has started much earlier from day 43 with eastward wind velocity of 63 m/s to westward wind velocity of 25 m/s on day 61, and hence, it is a major SSW event. The westward winds have prevailed for a longer time and slowly returned to eastward around day 84. In this case, the SW2 tidal amplitudes are larger than DW1 during days 20–70. The DE3 tide does not show any notable enhancement during this period.

In 2007–2008 winter, a minor SSW event is observed during days 54–58. After the day 35 though there is a deceleration associated with fluctuations of the eastward winds, it does not reverse to westward winds. In fact, after day 58, it becomes more eastward, and hence, this SSW event is a minor one. The minor SSW event is followed by two other minor SSW events during

days 67–71 and 76–80 and a major or final SSW during days 83–88. The maximum westward wind of 14 m/s is observed, and the westward winds prevail during days 85–89. The DW1 tidal amplitudes continue to be dominant during the entire observation period shown in the Figure. However, the enhancement of semidiurnal tide is noted during the days 45 and 75.
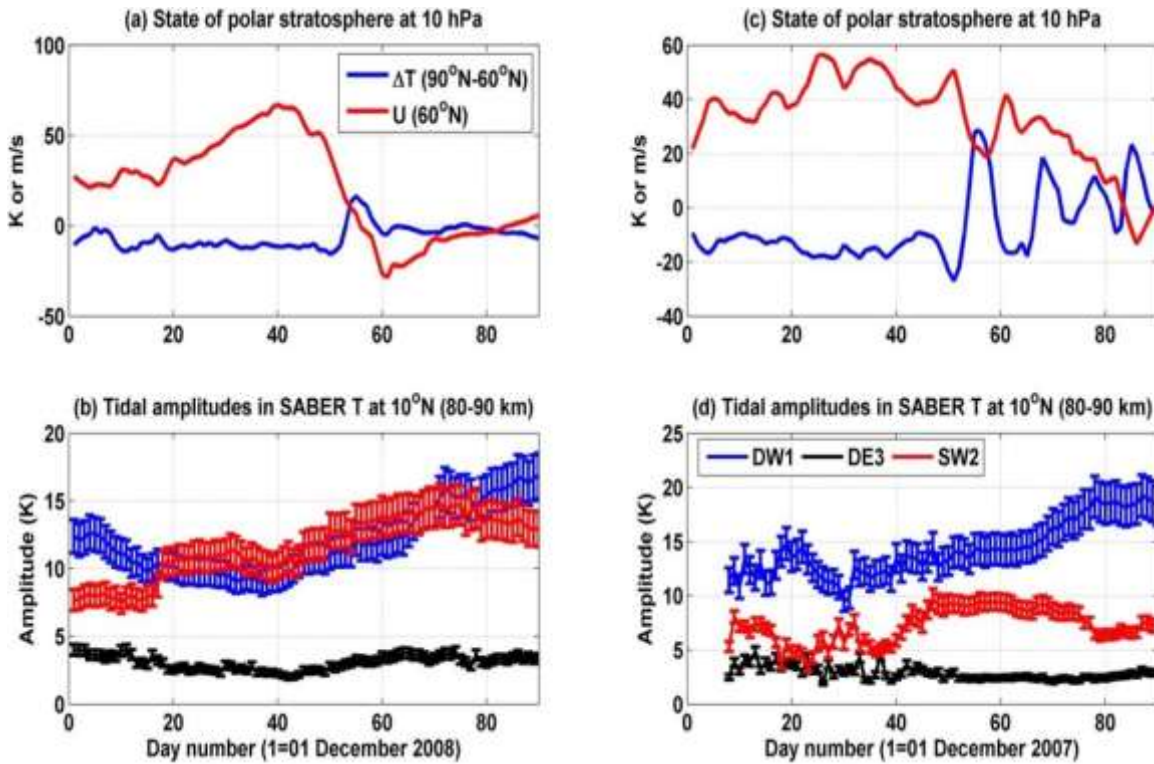
Figure 5.2: State of polar stratosphere at 10 hPa and tidal amplitudes in TIMED-SABER temperature at 10°N averaged for the heights 80–90 km for the 90 days starting from (a, b) 1 December 2008 and (c, d) 1 December 2007

From the above results it is clear that the semi-diurnal tidal enhancement is a common feature during SSW days. The diurnal tidal (DW1) amplitude gets decreased as they interact with the increasing planetary activity during SSW which can be seen in figure 5.1c and figure 5.2b. The enhancement of the SW2 can be attributed the increase in the ozone (O_3) concentration during SSW (Sridharan et al., 2012).

5.3.3 Duration of spread-F over Gadanki during boreal SSW of 2018-19

Boreal SSW occurred in December 2018-January 2019. Duration of spread-F over Gadanki during boreal SSW of December 2018 to January 2019 is shown in Figure 5.3. Red lines indicate geo-magnetically disturbed days with $A_p >= 12$. From 1 December 2018-31 January 2019 only five days are geomagnetically disturbed days. Most of the days spread-F is observed after 22:00 LST. Especially between 15th December 2018 and 7th January 2019 spread-F is observed almost daily when the SSW has occurred. Post-sunset spread F (spread-F before 22:00 LST) is observed only on 8 days.
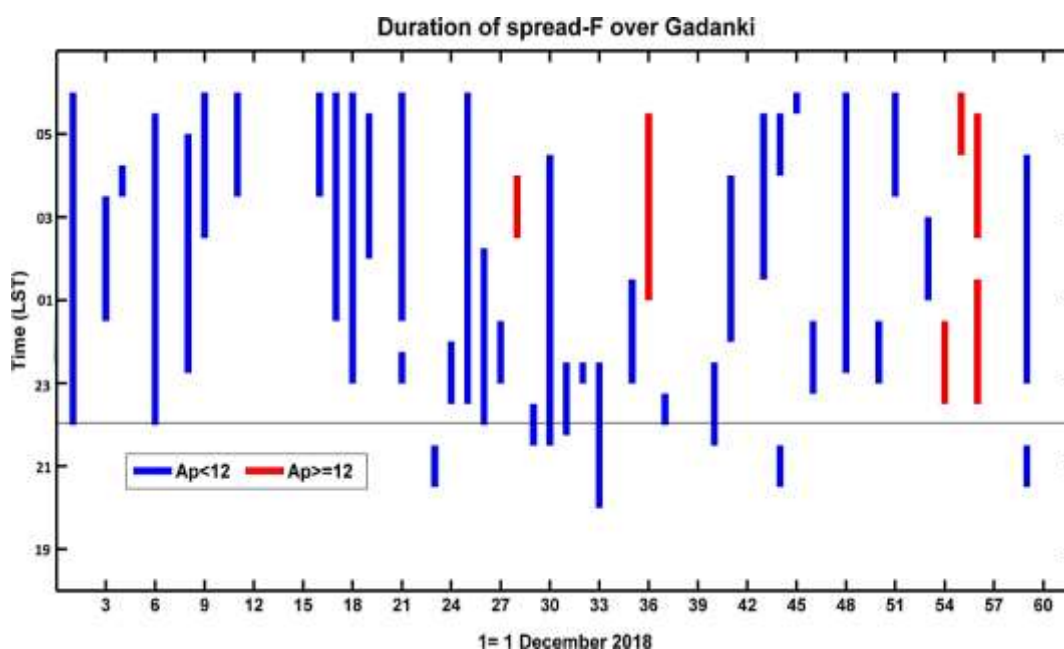
Figure 5.3: Duration of spread-F over Gadanki from 1 December 2018. The red lines denote the disturbed days ($A_p >= 12$)

5.3.4 Monthly mean of hmF$_2$ & hpF over Gadanki during boreal SSW of 2018-19

The monthly mean of hourly averaged hmF$_2$ and hpF over Gadanki during December 2018 and January 2019 is presented in Figure 5.4. There is an uplift of the hmF$_2$ during daytime with maximum value around 300 km at 13:00 LST, secondary maxima at 00:00 LST (300 km) and third maxima at 05:00 LST early morning hours. Similarly, the diurnal variation for hpF shows

that there is an upward drift during daytime with maxima (250 km) at 13:00 LST and another maximum at 00:00 LST (around 300 km). The hpF is a good indicator of the bottom side height of the F layer during nighttime when production of ions will be less due to lack of solar radiation (Maruyama et al., 2007). The F layer (hpF) is lifted to higher heights (above 300 km) during early morning time (at 05:00 LST). The diurnal variation of hmF_2 and hpF has three maxima.

During midnight hours the uplift of the F layer is visible after 22:00 LST with maximum value attained at midnight hours (00:00 LST). The uplift of the F layer around midnight hours will increase growth rate of RTI leading to thegeneration of post-midnight F-region irregularities.
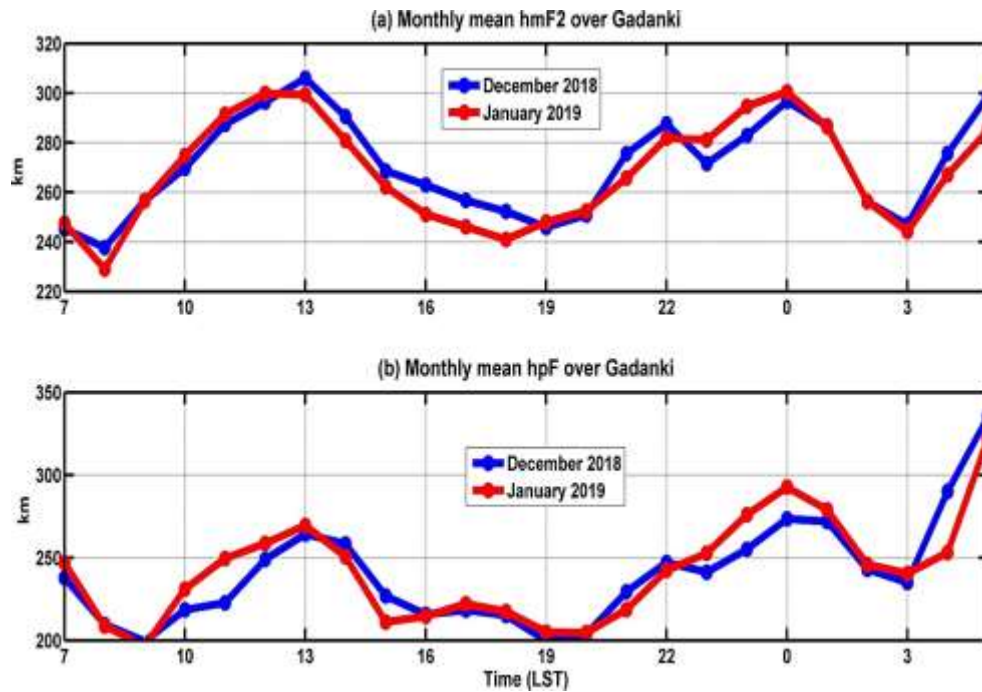
Figure 5.4: Monthly mean of diurnal variation of hmF_2 and hpF over Gadanki during December 2018 and January 2019

Earlier, Sridharan et al. (2009) noted semidiurnal tidal enhancement and reduction in diurnal tidal amplitudes in meteor radar (MF) wind observations over the dip equatorial station, Tirunelveli (8.7°N, 77.8°E) during major Sudden Stratospheric Warming (SSW) events. Sridharan (2019) observed enhancement of SW2 tide during northern hemispheric summer months and related it to similar ozone variations in the stratosphere. These results suggest that both during June–July and during the SSW events, which occur in December–February, SW2

59

tidal amplitudes are larger than DW1. Yizengaw et al. (2013) observed the occurrence of post-midnight irregularities in C/NOFS observations maximizing in June. They noted that the occurrence has longitudinal variations with the maximum over the African sector. Recently, Narayanan et al. (2019) observed post-midnight spread F over Gadanki on day number 69 (February 7, 2008), which they attributed to the electrified traveling ionospheric disturbances. It may be noted that the day number 69 is a peak warming (SSW) day. At middle latitudes, SSWis associated with warming in the lower thermosphere and cooling in the upper thermosphere, with both features exhibiting semidiurnal behaviour (Goncharenko and Zhang, 2008). Strong semi-diurnal variation in the vertical ion drifts are observed at the dip equator during SSW event (Chau et al., 2009).
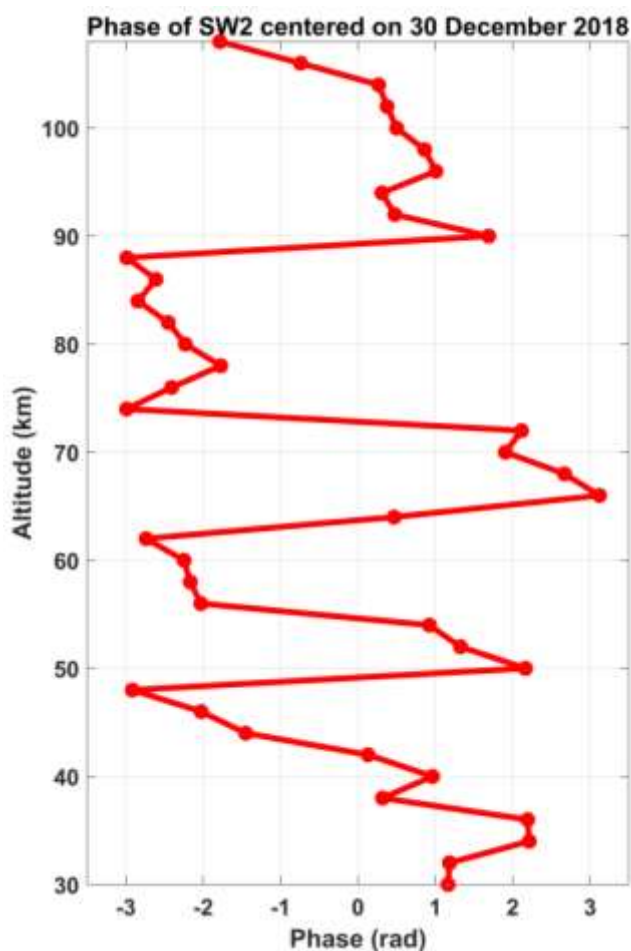
Figure 5.5: Phase of SW2 centered on 30 December 2018

The phase of SW2 centered on 30 December 2018 (boreal SSW of 2018-19) is presented in figure 5.5. The downward phase progression is observed above 90 km. This shows that SW2 can propagate upwards. It has large vertical wavelength therefore it can reach much higher heights without attenuation, having an impact on the zonal electric field in the ionosphere through the dynamo mechanism.

These results suggest that the semidiurnal tide can play a vital role in the formation of post-midnight F-region irregularities. The SW2 enhancement is a common feature during boreal SSW which in turn can affect the F-region irregularities. The increase in the amplitude of semi-diurnal (SW2) tide can impinge semi-diurnal variation in the electric field turning it eastward during midnight hours. Then, the eastward electric field can lift the F layer (hpF) to higher heights as observed during the boreal SSW, which can accelerate the growth rate of RTI during midnight hours.

5.4 Summary and Conclusions

1. The post-midnight F-region irregularities over low latitude stations (Gadanki and Kototabang) are found to be increased during boreal SSW of 2018/19.

2. The F layer is lifted to higher heights during midnight hours favouring the generation of the F-region irregularities.

3. During boreal SSW, the semi-diurnal (SW2) tidal amplitude is observed to be enhanced over the diurnal tide (DW1).The SW2 enhancement observed during boreal SSW can impinge semi-diurnal variation in the electric field which turned eastward in midnight hours thereby lifting F layer to higher altitudes.

Chapter 6:

Austral Sudden Stratospheric Warming impact on the post-midnight F-region irregularities

6.1 Introduction

In Chapter 4, the tidal variabilities investigated during solar minimum year shows that the amplitude of semi-diurnal tide (SW2) and the PO of Post-midnight F-region irregularities maximise during June solstice months. Many studies have been shown that the meteorological processes such as planetary waves, gravity waves, and tides can have direct or indirect effects on the F-region ionosphere (Lastovicka, 2006; Rishbeth, 2006) which are expected to be particularly strong at low latitudes, where the ionospheric plasma is extremely sensitive to the strength of the zonal electric field and the daytime electric field is modulated by tidal winds in the lower thermosphere through the E- region dynamo process. The vertical drift lifts ionospheric plasma to the altitudes of lower recombination rates, thus increasing plasma density.

A large part of variability in the ionosphere-thermosphere system is thought to be associated with lower atmospheric processes. During solar minimum years, the lower atmospheric processes such as sudden stratospheric warming (SSW) can have an impact on the ionosphere (Goncharenko and Zhang, 2008; Chau et al., 2009). Boreal SSW impact on the F-region irregularities is investigated in Chapter 5. SSWs are dynamic events in the polar stratosphere and more common in the northern hemisphere.

However in southern hemisphere SSWs are rare. The planetary waves are weak in southern hemisphere due to comparatively weak land-sea contrast and smaller orography to northern hemisphere. But occasionally the planetary waves can be amplified through atmospheric blocking, specific circulation patterns or other external atmospheric forcing (Shen et al., 2020). Austral SSWs are reported twice since their discovery. One occurred in 2002 which is a solar maximum year and second one in 2019 which is a solar minimum year. The planetary wave forcing in 2019 is small compared to that in 2002 however, it has been most persistent on record

(Shen et al., 2020). The recent austral SSW event in solar minimum year of 2019 gives an opportunity to study its impact on the occurrence of these PMF and their relationship with the mesospheric tides.

6.2 Data and Methodology

6.2.1 F-region observations from EAR, Kototabang

The range time intensity plots of the EAR observations are screened manually to determine the PO of the post-midnight F-region FAI echoes. Only quiet days ($A_p < 12$) are considered while analysing the radar echoes.

6.2.2 Ionosonde observations over Kototabang

The ionosonde at Kototabang is a frequency modulated-continuous wave (FM-CW) one, which operates from 2 to 30 MHz with a peak power of 20 W. The peak height of F_2 layer electron density peak (hmF_2) and the virtual height of the bottom side F-layer (hpF or h'F) obtained from the Kototabang ionosonde observations are used in the present work. These parameters are scaled with 15 min intervals. This ionosonde has been operated by the National Institute of Information and Communications Technology (NICT) as the SEALION project (Maruyama et al., 2007).

6.2.3 TIMED-SABER temperature

The SABER temperature is subjected to space time spectral analysis to determine the amplitudes of the tides for the years 2018 and 2019.

6.2.4 NCEP Reanalysis winds and temperature

In the present work, the reanalysis winds and temperature are used to infer the state of polar stratosphere particularly to identify SSW events.

6.3 Results and Discussions

6.3.1 PO of post-midnight F-Region FAI radar echoes over Kototabang
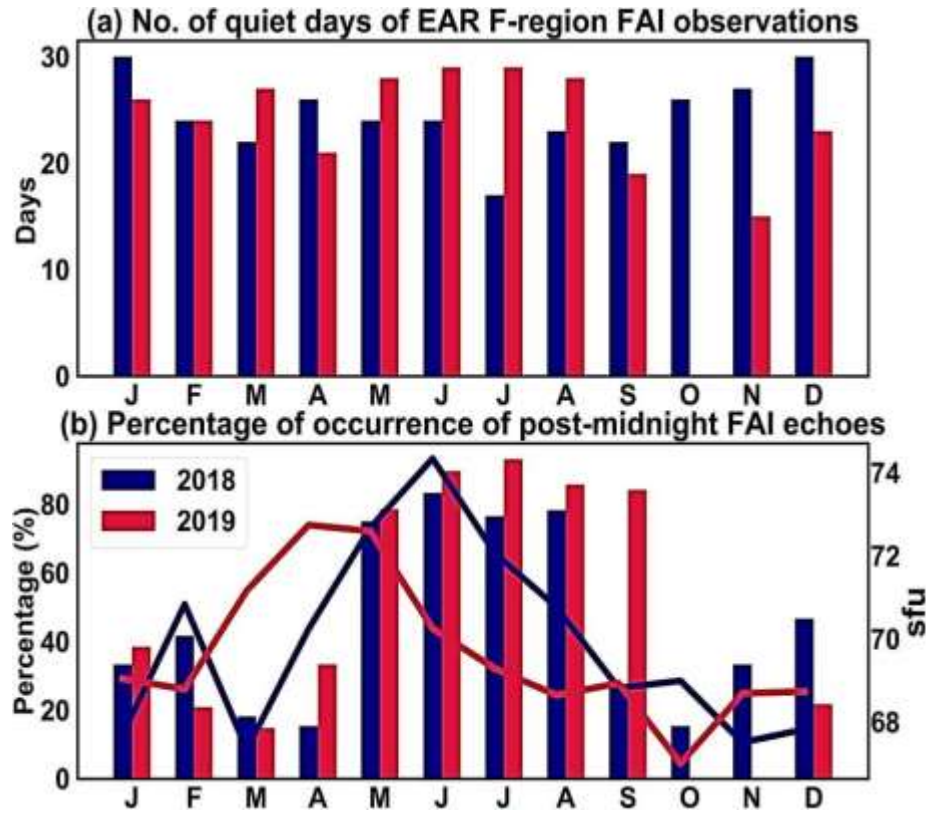
Figure 6.1: (a) Number of quiet days (Ap < 12) for which the F-region observations of Equatorial Atmosphere Radar (EAR) are available for each month of years 2018 and 2019 (b) Monthly variations of the percentage of occurrence (PO) of post-midnight (22:00-06:00 LST) F-region field aligned irregularities (FAI) echoes observed by the EAR for quiet days of the years 2018 and 2019

The PO of post-midnight FAI echo is calculated for every month for years 2018 and 2019. Figure 6.1a shows the number of observations available and 6.1b shows the PO of FAI echoes for quiet days along with solar flux. The PO for June, July, and August 2018 is above 76% whereas it is above 85% in 2019. The PO of September 2019 shows a maximum of 84% compared to 27% of the year 2018. Even after removing the disturbed days, the persistence of the high PO of the post-midnight FAI echoes suggests the probable lower atmospheric wave coupling.

6.3.2 Inter-annual variability of post-midnight F-region FAI echoes in September

The inter-annual variability of the PO of post-midnight FAI echoes in September for the years 2011–2019 is shown in Figure 6.2 along with the annual and monthly (September) mean solar flux.
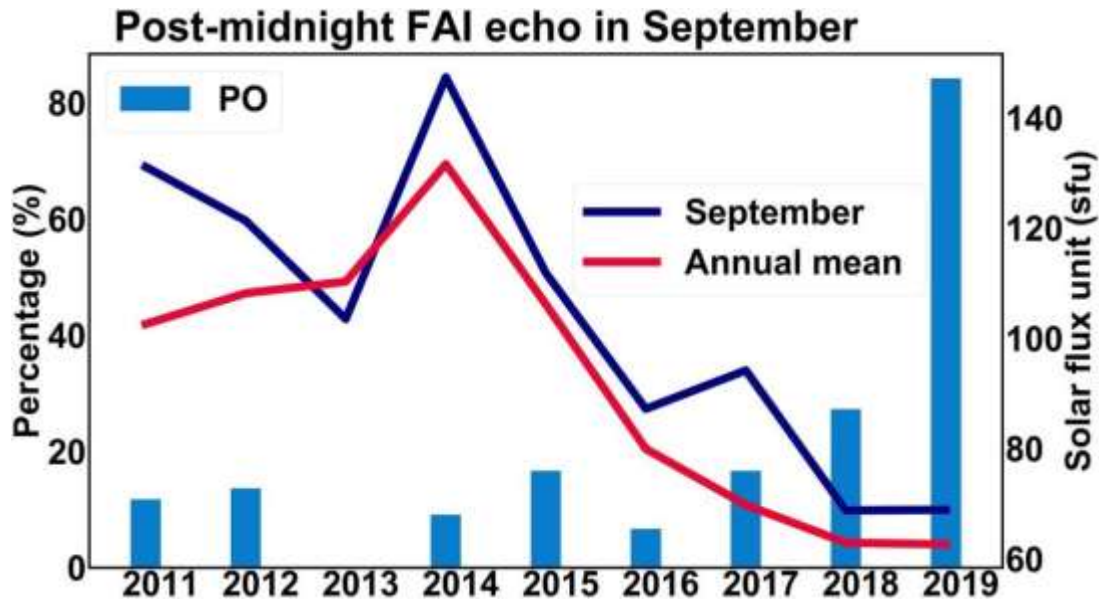
Figure 6.2: Inter-annual variabilities of the (a) solar flux and (b) percentage of occurrence (PO) of post-midnight F-region field aligned irregularities (FAI) echoes during the quiet days $(A_p < 12)$ of September for the years 2011–2019

The PO decreases from 11% in 2011 to 6.6% in 2016 and it again increases to 84% in 2019. The F10.7 cm solar flux downloaded from https://spaceweather.gc.ca/solarflux/sx-5-mavg-en.php is used to determine the annual solar flux and daily averaged solar flux unit (sfu) data from omniweb database is used to investigate the relationship between the PO of post-midnight FAI echoes and solar activity for quiet days. When the F10.7 cm solar flux in September is around 69 sfu in the year 2019, the PO is 84%. When it is around 103 and 147 sfu, the PO is 0% and 9% respectively. However, when it is around 111 sfu, it is 17%. The relationship of PO with solar activity is more apparent, when the solar flux is averaged for the whole year. When the solar flux decreases from 79 sfu to 63 sfu, the PO increases from 6.67% to 84%. The minimum PO is observed in the year 2013, when the annual solar flux is 110 sfu.

6.3.3 Duration of the EAR F-region FAI echoes in September 2018 and 2019
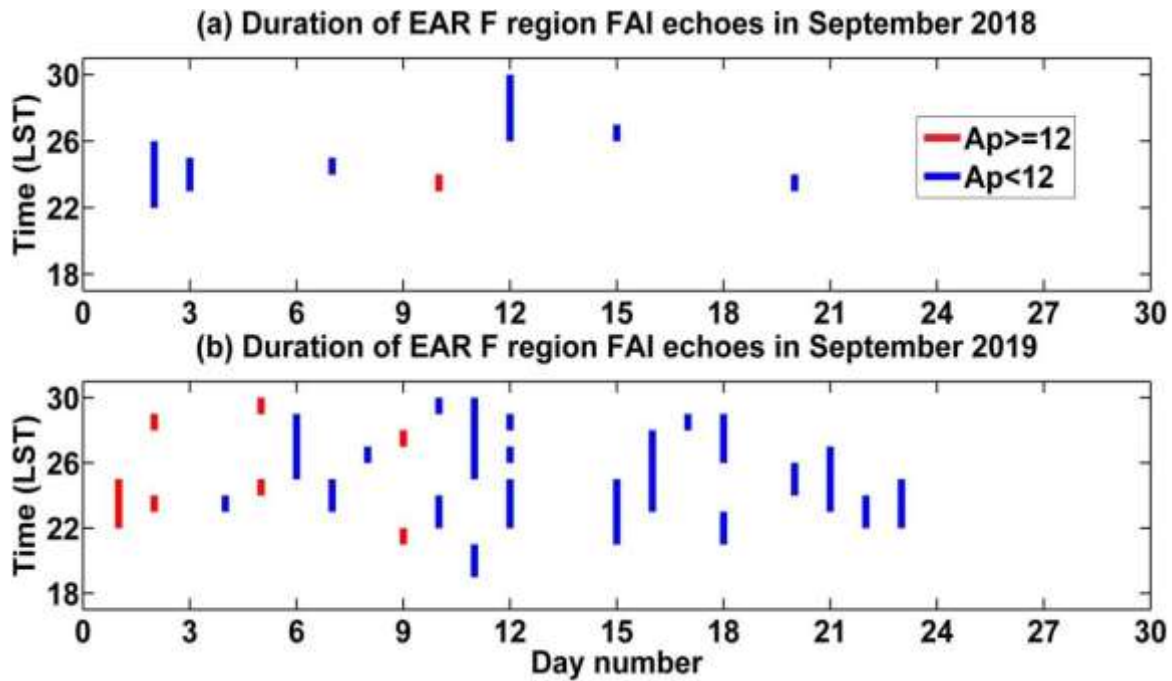
Figure 6.3: Duration of EAR echoes from F-region field aligned irregularities (FAI) during (a) September 2018 and (b) September 2019

Duration of the presence of the FAI echoes for all days of September is shown in Figures 6.3a-b for years 2018 and 2019 respectively. It is found that the FAI echoes are absent for most of the days of September 2018, whereas they are present in almost all the days in September 2019 after 22:00 LST. These results suggest that though the PO of the post-midnight FAI echoes is likely to be more during solar minimum years, it is anomalously large in September 2019, even when compared to September 2018 which is having a similar solar flux value. The large increase in the post-midnight FAI echoes may be related to the tidal variabilities associated with the austral SSW event that occurred during September 2019. To investigate this, TIMED-SABER temperature data are used.

6.3.4 State of southern hemispheric polar stratosphere during 2018 and 2019
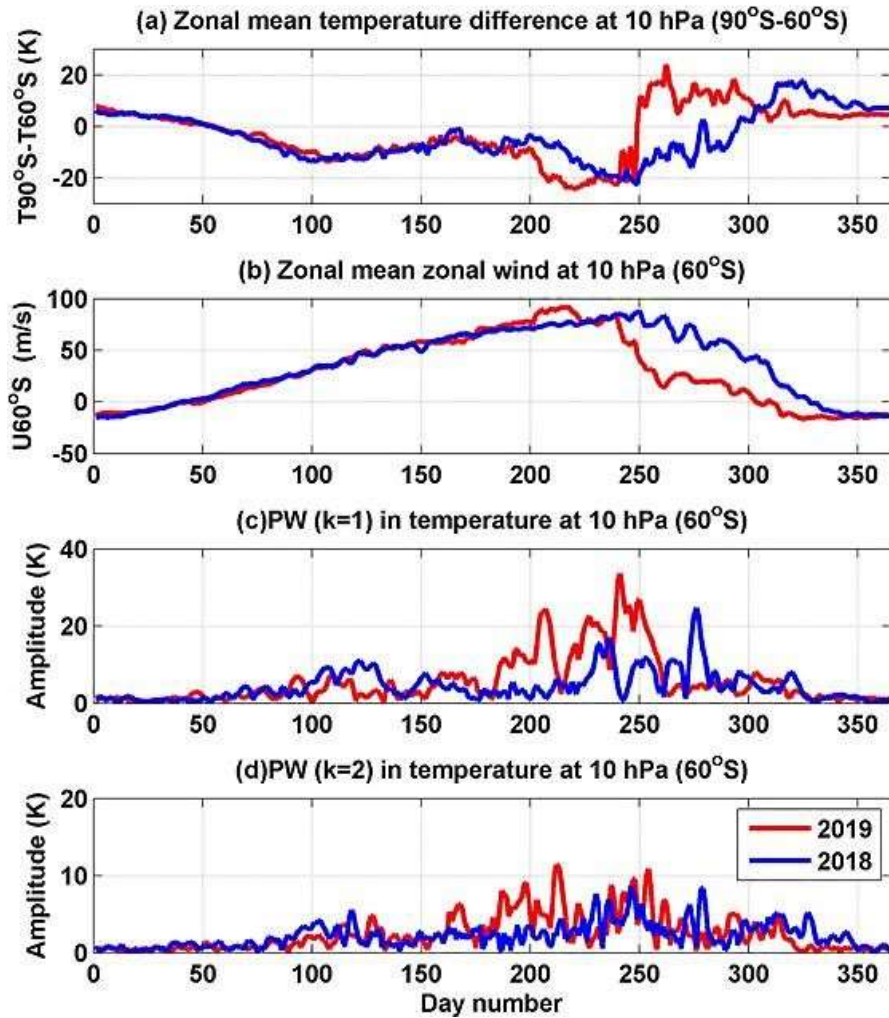
Figure 6.4: Daily variations of (a) zonal mean temperature difference between 90°S and 60°S (ΔT), (b) zonal mean zonal wind (U) at 60°S and (c)–(d) amplitudes of the planetary waves of zonal wavenumbers 1 and 2 in temperature at 10 hPa over 60°S. The temperature and winds are from NCEP NCAR reanalysis data sets

To identify the occurrence of the austral SSW event, the NCEP/NCAR Reanalysis temperature and wind data at 10 hPa for the austral polar latitudes are used. Figures 6.4a-c shows the daily variations of the zonal mean of the temperature difference between the latitude 90°S and 60°S and zonal mean zonal wind at 60°S in the polar mid-stratosphere (10 hPa) and amplitudes of planetary wave (PW) of k = 1 and k = 2 at 10 hPa temperature and at 60°S for the years 2018 and 2019.

In the year 2018, the temperature difference between the latitudes 90°S and 60°S is positive before day number 50 and after day number 300 during the southern hemispheric summer. It is below zero during the southern hemispheric winter. It is close to zero and slightly positive (below 3 K) during day numbers 278–280. In the year 2018, though deceleration of zonal mean zonal wind occurs after day number 250, the rate of deceleration is less and it becomes westward only after day number 300. However, in the year 2019, the polar temperature difference between the latitude 90°S and 60°S becomes positive after day number 248 and reaches a maximum on day number 264 (22 K) and it remains positive, but with fluctuations until the day number 314. The zonal mean zonal wind shows sudden deceleration from 84 m/s (day number 234) to 16 m/s (day number 262). After day number 262, the wind slowly decreases and become westward after day number 305.

The amplitude of PW of k = 1 at 60°S enhances to about 30 K prior to the austral SSW event in the year 2019 followed by a drastic decrease simultaneously with the sudden rise in the temperature difference between the latitudes 90°S and 60°S. In the year 2018, PW activity is relatively weaker. The amplitude of PW of k = 2 is relatively much weaker when compared to PW of k = 1, though it has also shown increased amplitudes prior to the SSW event. Earlier observations showed that there could be an accumulation of ozone molecules over equatorial latitudes during the boreal SSW events (Sridharan et al., 2012). To see whether similar ozone enhancement is there during the austral SSW events, TIMED-SABER ozone vmr is analysed.

6.3.5 Ozone mixing ratio

The height-time cross-sections of zonally averaged daily mean TIMED-SABER ozone vmr over the equator (5°N–5°S) and 10°N (5°N–15°N) are shown in Figure 6.5 for the heights 30–50 km and the years 2018 and 2019. From the Figure, we can infer that the ozone vmr over the equator is larger (>12 ppmv) during 239–293 in the year 2019, which includes the austral SSW event. However, the ozone vmr is only around 10 ppmv during the same period in the year 2018. It is, in general, less in 2018 than in 2019 at 32 km. Particularly, during day numbers 100–200, the ozone vmr in 2018 is only around 9 ppmv, whereas it is 11 ppmv in the year 2019. Over 10°N also, though the ozone vmr is less than 10 ppmv during day numbers 130–200 of the year 2019, it starts increasing after day number 217 and the enhanced ozone vmr persists until day number

302. A similar enhancement is not observed in the year 2018 during the same period of time.
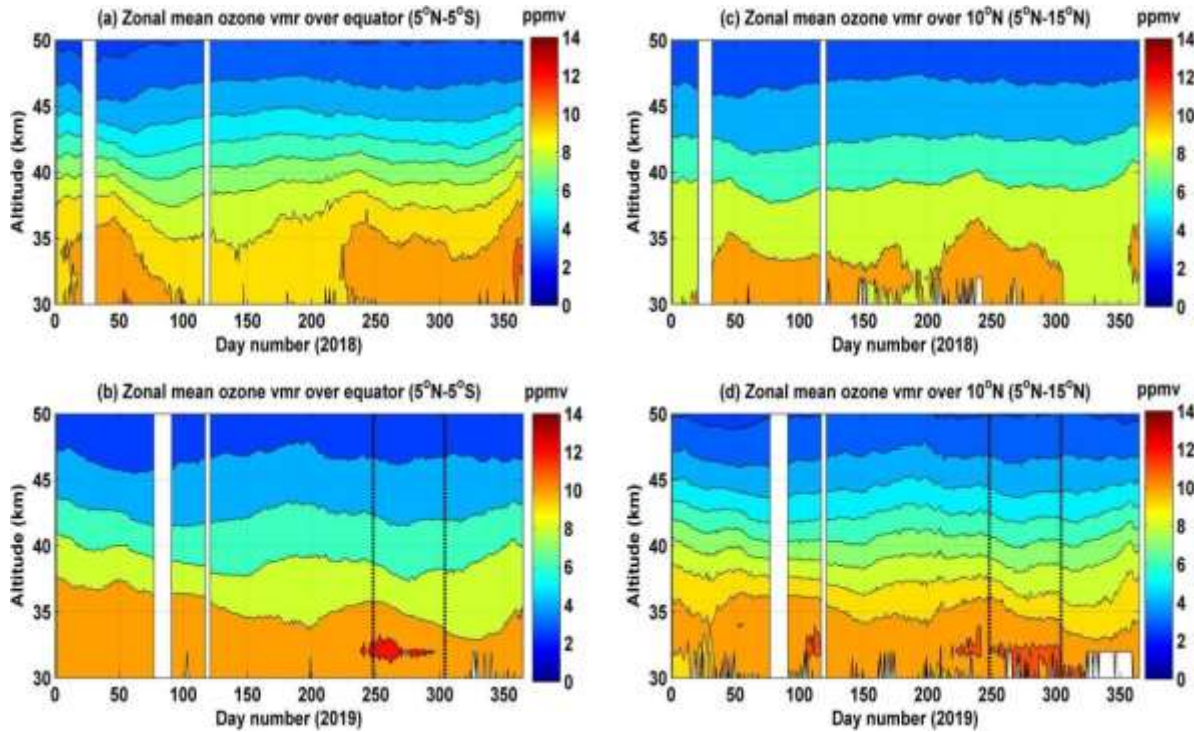
Figure 6.5: Time height cross-section of the zonal mean TIMED-Sounding of the Atmosphere by Broadband Emission Radiometry (SABER) ozone volume mixing ratio (vmr) over (a–b) equator and over (c–d) 10°N for the years 2018 and 2019. The vertical dotted lines denote the duration of the austral Sudden Stratospheric Warming (SSW) 2019

6.3.6 Tidal variabilities in the upper mesospheric region

The time variations of the migrating diurnal (DW1) and semi-diurnal (SW2) tidal amplitudes over 10°N are shown in Figure 6.6 for the years 2018 and 2019. From the Figure, we can infer that in the year 2018, the DW1 tides show semi-annual variation with a maximum (greater than 15 K) during day numbers 50–150 (March-May) and 200–300 (August–October) and it shows a minimum during day numbers 150–200 (June and July), when the SW2 tidal amplitudes are larger than DW1. Both DW1 and SW2 tidal amplitudes are comparable in April and September of 2018. In the year 2019, though DW1 shows maximum during March–May as in the year 2018, the expected maximum during September and October is nearly absent. It shows a minimum (7 K) around day number 250 and lower amplitudes (<10 K) until day number 280. The SW2 tidal amplitudes are larger (~10 K) during day numbers 130–270 with a maximum on day

70

numbers 211 (18 K) and 261 (15 K). Though SW2 tidal amplitude in the year 2018 also shows larger amplitudes during day numbers 260–270, the DW1 is also much larger (18–20 K) during this time. The DE3 tidal amplitude shows a broad maximum (>10 K) during day numbers 150–270, whereas the diurnal stationary DS0) tidal amplitude shows significant enhancement (>10 K) during day numbers 250–300, which include the austral SSW event of 2019.
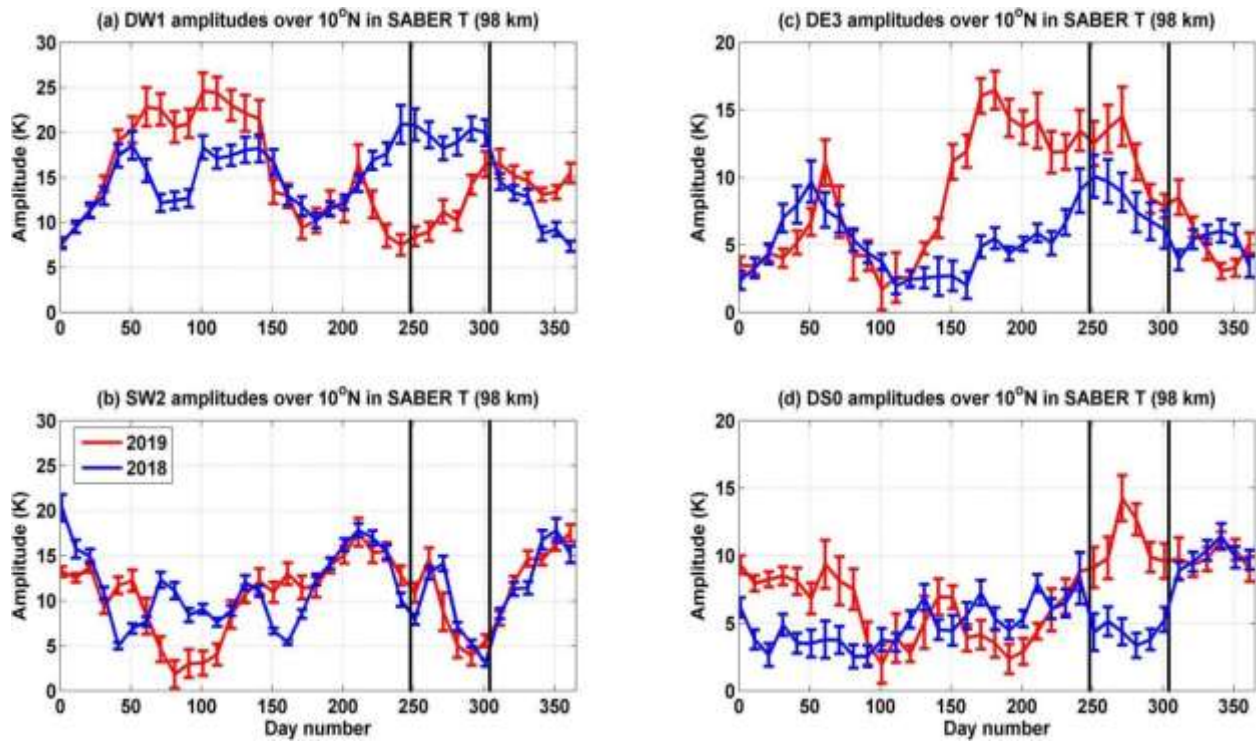
Figure 6.6: Time variations of DW1, SW2, DE3 and DS0 tidal amplitudes in TIMED-Sounding of the Atmosphere by Broadband Emission Radiometry (SABER) temperature at 98 km for the years 2018 and 2019. The vertical black lines denote the duration of the austral Sudden Stratospheric Warming (SSW) 2019

The tidal variations presented here are over 10°N, which is near to the dip equator over the Indonesian sector; it appears that the tidal coupling of the neutral atmosphere with the equatorial ionosphere takes place through dynamo mechanism, which is more effective at the dip equator. The global tidal variations and the local geomagnetic geometry play a major role in the neutral ion coupling at a particular sector. The dominant semi-diurnal tidal variation in the electric field becomes eastward at later hours near midnight and it can lift the F-layer to higher heights, which may favour the growth of the RTI leading to F-region irregularities. To investigate this, ionosonde observations are used.

6.3.7 hmF$_2$ variations over Kototabang

The hmF$_2$ variations are obtained from the ionosonde observations over Kototabang for September and October 2019, which include the austral SSW event. The hmF$_2$ averaged for the quiet days of September and October of 2019 are shown in Figures 6.7a and 6.7b.

(a) Mean hmF2 variation in September 2019

(b) Mean hmF2 variation in October 2019
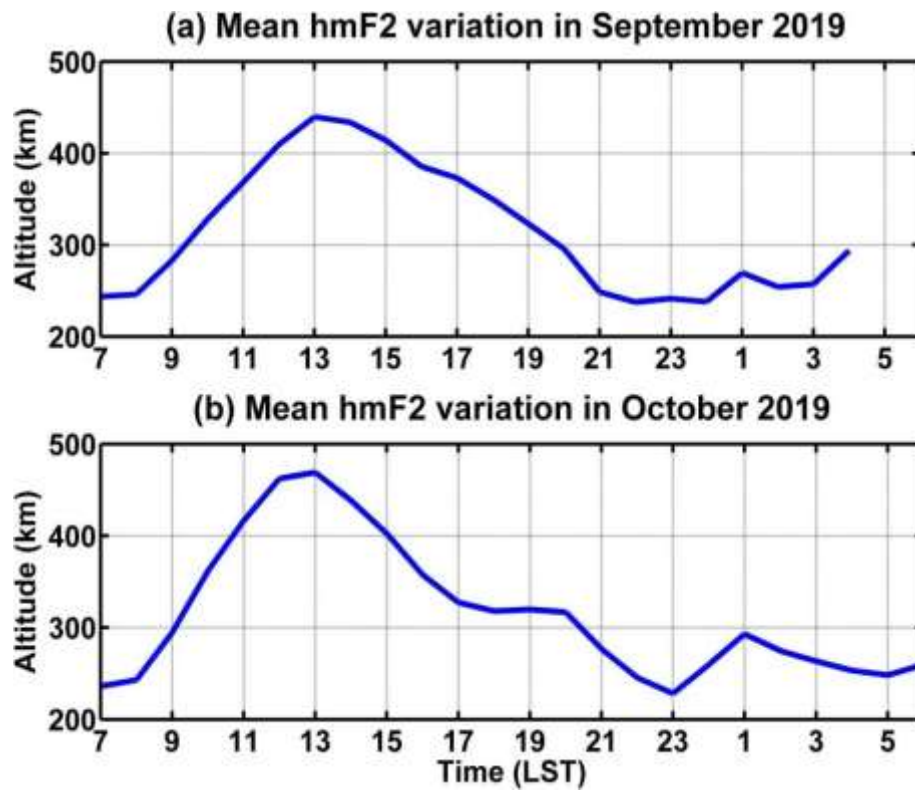
Figure 6.7: Mean diurnal variations of hmF$_2$ over Kototabang during the quiet days of (a) September and (b) October 2019

The mean hmF$_2$ shows a maximum (~450 km) at 13:00 LST in September and October. After midnight a small increase in hmF$_2$ can be observed in September to above 250 km. In October, the hmF$_2$ decreases to about 200 km and at later hours it increases to 290 km around 01:00 LST. The large increase in the hmF$_2$ around noontime is due to the large $E \times B$ vertical drift, which shows longitudinal variations. In particular, the vertical drift shows a wavenumber 4 structure around the globe with upward peaks near 10°E, 100°E, 200°E, and 280°E with maximum upward drift over the Indonesian/western Pacific sector (Kil et al., 2007 for example).

6.3.8 Wavelet spectrum of hmF$_2$ over Kototabang

To infer the connection between tidal oscillation and the ionosonde parameters, the hourly hmF$_2$ values for September 2019–November 2019 are subjected to wavelet analysis which can be used to identify localized variations of power within a time series.

Wavelet spectrum of hmF2 over Kototabang
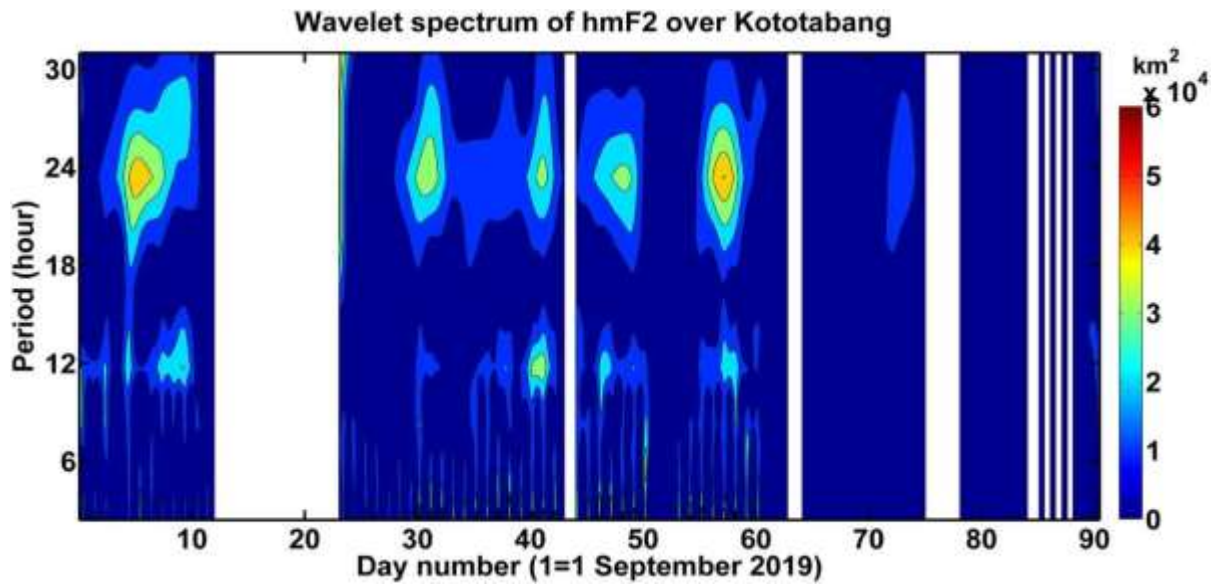
Figure 6.8: Wavelet spectrum of hmF$_2$ (24 h variation removed) over Kototabang from September 1, 2019–November 30, 2019

As the hmF$_2$ variation over Kototabang is dominated by larger $\mathbf{E} \times \mathbf{B}$ drift during daytime as a part of wavenumber-4 structure observed commonly in many ionospheric parameters (Kil et al., 2007), the composite diurnal variation is removed from the hourly variation of hmF$_2$ before subjecting it to wavelet analysis with morlet wavelet function as mother wavelet. By decomposing a time series into time-frequency space, both the dominant modes of variability and how those modes vary in time can be determined (Torrence and Compo, 1998). The wavelets are localized functions, which can resolve frequency changes in short time periods. From the wavelet spectrum shown in Figure 6.8, we can infer that the diurnal (24 h) and semi-diurnal (12 h) variations are dominant during September and October 2019, whereas the semi-diurnal variations are completely absent in November 2019. This reveals that the hmF$_2$ is influenced by semi-diurnal tide during the austral SSW.

6.3.9 Mean hpF and vertical drift variations over Kototabang
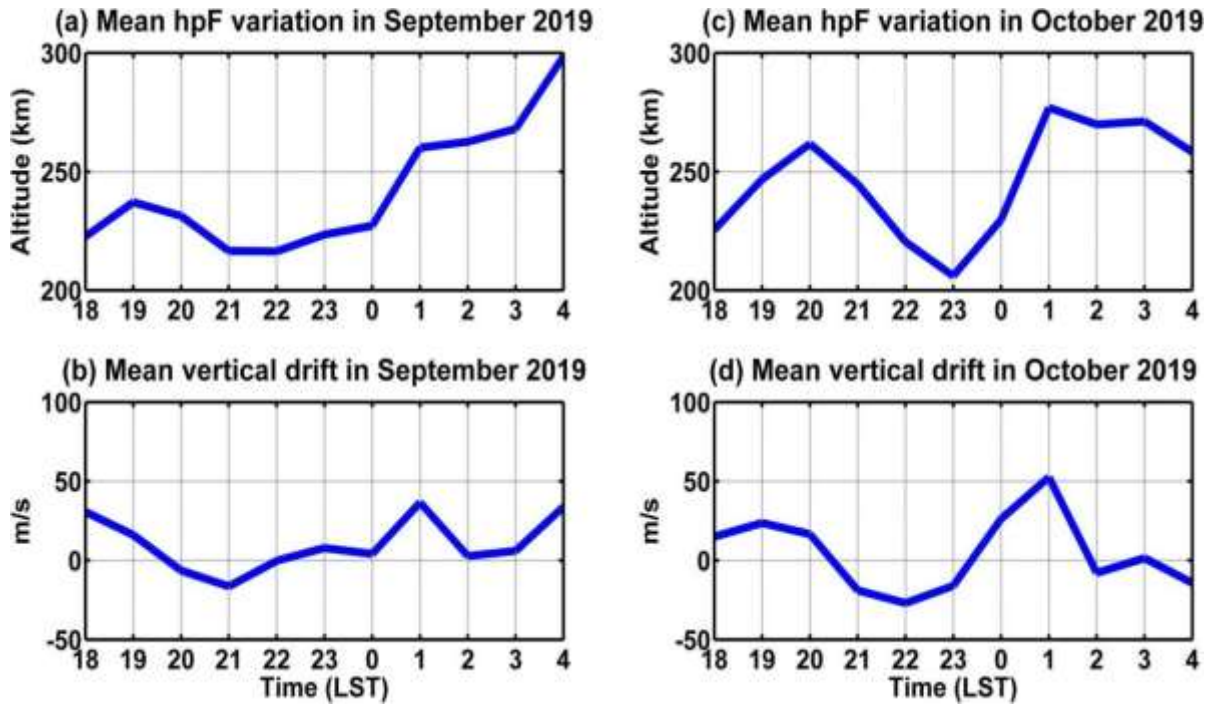
Figure 6.9: Mean night-time variations of (a), (c) hpF and (b), (d) vertical drift over Kototabang during the quiet days of September and October 2019

The hpF with higher altitude will provide information regarding the dynamic processes particularly the vertical $\mathbf{E} \times \mathbf{B}$ drift after sunset (Maruyama et al., 2007). However, when hpF is below 300 km the upward motion due to recombination is not negligible (Bittencourt and Abdu, 1981). The hpF can be still be used to determine the vertical motion of the bottomside F-region qualitatively (Saito and Maruyama, 2006). The hpF variations averaged over quiet days of September and October 2019 is shown in Figures 6.9a and 6.9c. The hpF is found to increase above 250 km after 00:00 LST in both September and October 2019. After midnight, the hpF tends to increase further in September, whereas it decreases in October.

The vertical drift velocity is estimated from the time derivative of hpF at each hour of all quiet days and the diurnal variation is averaged for all the quiet days of September and October 2019 to obtain its mean diurnal variation which is shown in Figures 6.9b and 6.9d. The vertical drift is

observed to be upward in September and October till 20:00 LST after which it turned downward. The drift turned upward again after 22:00 LST and 23:00 LST in September and October respectively. These results suggest that the vertical drift can be upward near midnight hours.

The F-region FAI observations of EAR reveal an anomalous increase in the PO (84%) of the post-midnight radar echoes during September 2019 when compared to only 27% during September 2018. It is the highest PO in September during the years 2011–2019. Coincidentally, the SSW event has occurred in the austral polar stratosphere during September 2019. The mesospheric tidal variabilities are investigated for the years 2018 and 2019. It is found that the DW1 tidal amplitude shows the expected semi-annual variation with maxima during equinox months in the year 2018. However, in the year 2019, the secondary maximum is almost absent. In particular, the DW1 amplitude decreases further during September 2019. Though there is a large stratospheric ozone vmr observed at equatorial latitudes during the austral SSW 2019, significant increase in the semi-diurnal tidal amplitude has not been observed. The SW2 tidal amplitudes in 2019 are only slightly enhanced compared to that of 2018 probably due to the reason that the austral SSW 2019 is a minor one. It is also possible that the DW1 tide may have interacted with the planetary wave (PW) of zonal wavenumber 1 to generate DS0 (Truskowski et al., 2014). The enhancement of DS0 and reduction of DW1 during and after the austral SSW 2019 confirm this. The interaction between SW2 and PW of k = 1 generating SW1 and SW3 has been observed through observations and modeling (for example: Forbes and Wu, 2006; Pancheva and Mukhtarov, 2012; Yamashita et al., 2002). In the year 2019, the DE3 tide also shows large amplitudes (>10 K) for an extended period of day numbers 150–280, whereas the large amplitude of DE3 is limited to day numbers around 50 and 250 in 2018. As the PO of post-midnight FAI echoes is nearly the same in both 2018 and 2019 during June-August months, DE3 is less likely to be the reason for the formation of these echoes. However, it needs further investigation. The suppression of DW1 during September 2019 may also be due to the generation of the DW1 tides with opposite phases due to the solar insolation absorption by the accumulation of ozone in the stratosphere and water vapour in the troposphere, as noted in the global scale wave model (GSWM) simulations (Hagan, 1996).
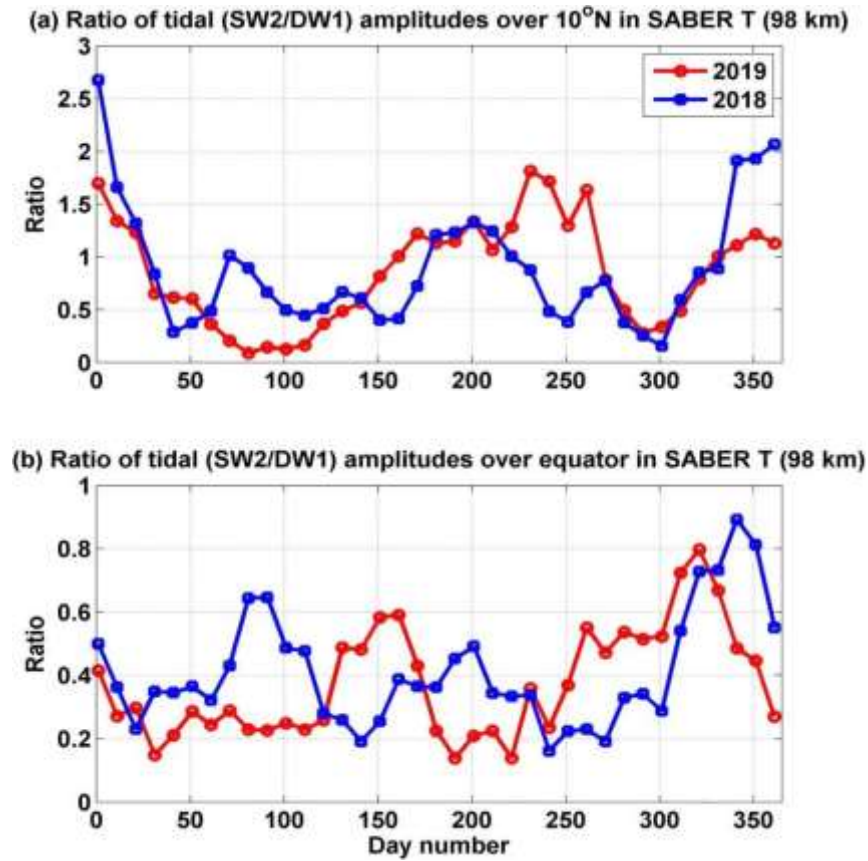
Figure 6.10: Ratio of tidal (semi-diurnal tide [SW2]/diurnal tide [DW1]) amplitudes in TIMED-Sounding of the Atmosphere by Broadband Emission Radiometry (SABER) temperature at 98 km over (a) 10°N and (b) equator

In both years, the tidal amplitudes of SW2 are comparatively larger than those of DW1 during June–September. Figure 6.10 shows the ratio of SW2 to DW1 tidal amplitudes over 10°N and equator. From the Figure 6.10, we can infer that the ratio is larger than 1 during day number 210–270 of 2019, whereas it is less than 1 during the same time period of the year 2018. After day number 330, the ratio again increases to 2 probably due to the major boreal SSW event. The PO of the post-midnight FAI echoes is also more in December 2018, when compared to December 2019. The DW1 tidal amplitude is very less in September 2019 than September 2018; the SW2 amplitude is much larger than DW1 in September 2019. It appears from the present results that the enhancement of SW2 relative to DW1 favours the formation of post-midnight FAI echoes. Chakrabarty et al. (2014) observed the shift of the F_2 layer around midnight and attributed it to be due to the influence of the thermospheric semi-diurnal tide.

76

They attributed it to the enhancement of mesospheric SW2 during June solstice. The post-midnight spread F could also be due to the enhanced semi-diurnal tide, which has consistently been observed during the SSW events. Earlier, Sridharan et al. (2009) reported enhancement in the semi-diurnal tidal amplitudes along with a reduction in diurnal tidal amplitudes in the MF radar winds over Tirunelveli (8.7°N, 77.8°E). Further Sridharan et al. (2012) demonstrated that the enhanced semi-diurnal tides could be due to the accumulation of ozone molecules over the equatorial latitudes during the SSW events. Sridharan (2017) noted that the enhanced semi-diurnal tide during the SSW event is mostly the migrating SW2 and the contribution from the non-migrating semi-diurnal tide is relatively less. The dominant semi- diurnal tide could be the reason for the large occurrence of post-midnight FAI echoes during boreal summer months, particularly June–July and during the polar SSW events, which normally occur during boreal winter and very rarely during austral winter (September).

6.4 Summary and Conclusions

The results can be summarized as follows:

1. The post-midnight F-region FAI echoes occurrence is larger during September 2019, when compared to the same month of other years. The large PO of post-midnight F-region FAI echoes is related to the occurrence of the Austral SSW event, which occurred in September 2019.

2. Enhancement of the ozone vmr is observed at equatorial latitudes during September 2019, when compared to the same in September 2018.The expected SW2 tidal amplitude enhancement is not observed at the upper mesospheric heights during September 2019. However, the DW1 tidal amplitudes get suppressed during September 2019.

3. The suppression of DW1 may either be due to non-linear interaction with the large planetary wave activity preceding the austral SSW or it could be due to the generation of the DW1 by water vapour and ozone with opposite phases.

4. Though SW2 has not shown any significant enhancement during September 2019, when compared to September 2018, the DW1 is suppressed leading to relative enhancement of SW2 during September 2019. In September 2018, DW1 is larger than SW2.

5. Therefore, it can be concluded that the relative dominance of the semi-diurnal tide over the diurnal tide have impinged semi-diurnal variation in the ionospheric parameters like hmF_2 thereby, lifting the F layer to higher heights leading to the growth of F-region irregularities around midnight hours.

Chapter 7:

Longitudinal variation in the post-midnight F-region irregularities during Austral SSW of 2019

7.1 Introduction

There are many causative mechanisms suggested for the formation of the post-midnight spread- F (PMSF). The maximum occurrence of the PMSF during solar minimum years indicates the role of lower atmosphere on the generation of these irregularities. The impact of the atmospheric tides on the PMF is studied in Chapter 4. The role of SSWs are analysed in Chapter 5 and Chapter 6. In Chapter 6 we have discussed the influence of the austral SSW on the occurrence rate of post-midnight F-region FAI echoes over Kototabang. The PO of post-midnight F-region FAI echoes have increased over Kototabang in September 2019 when an austral SSW has occurred. The occurrence of the PMF shows longitudinal variability with maximum occurrence over African sector (Yizengaw et al., 2013). The longitudinal variability in the occurrence of the PMF during Austral SSW of 2019 is investigated in this Chapter.

7.2 Data and Methodology

7.2.1 Digisonde observations from Jicamarca and Ascension Island

The digisonde data over Ascension Island (7.9°S, 14.4°W geographic; dip latitude: 16°S) and Jicamarca (11.95°S, 76.87°W, dip latitude: 1.10°N) are obtained from the ftp site: ftp.ngdc.noaa.gov. The ionograms are scaled using SAO explorer software package (http://umlcar.um.edu) to obtain the vertical electron density profile, and various ionospheric characteristics like the ionospheric F_2 layer peak plasma frequency (foF$_2$), peak height (hmF$_2$) and minimum virtual height of the F layer (hpF) (Reinisch, 1996). The derivative of hpF with time can be used as vertical $\mathbf{E} \times \mathbf{B}$ drift velocity (Abdu et al., 1981).

7.2.2 TIMED-SABER temperature

SABER temperature observations are utilized to obtain tidal amplitudes. Amplitudes of migrating semi-diurnal tide with zonal wavenumber 2 (SW2), migrating westward propagating diurnal tides with zonal wavenumber 1 (DW1) and non-migrating eastward propagating diurnal tide (DE3) are determined from the SABER temperature.

7.3 Results and Discussions

7.3.1 Inter-annual variability of spread F over Jicamarca and Ascension Island
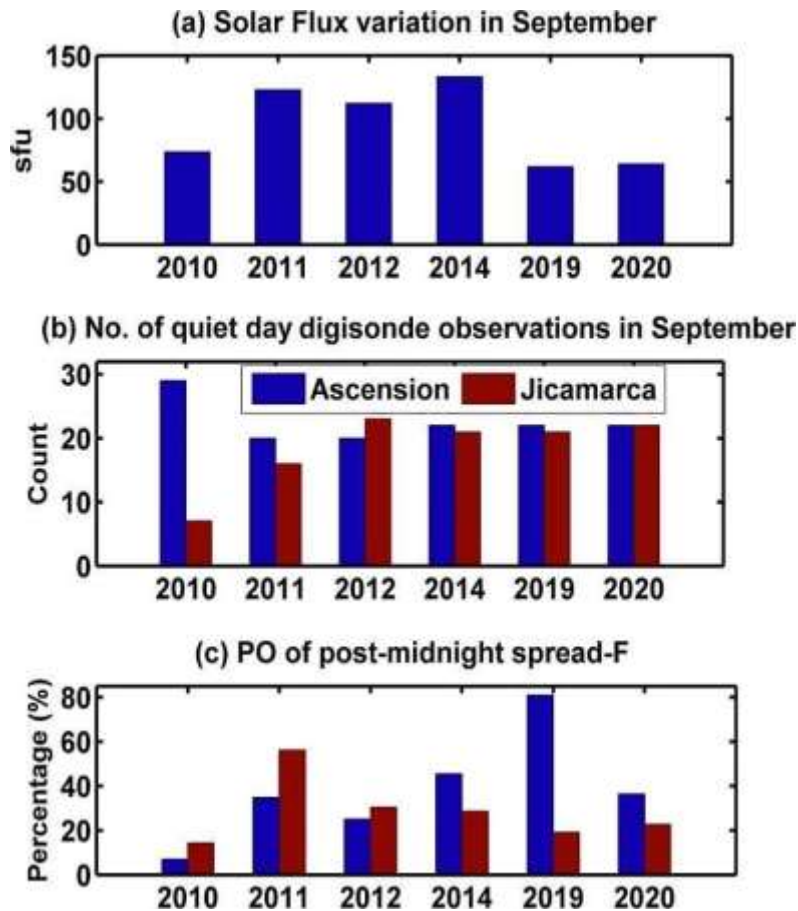
Figure 7.1: Inter-annual variabilities of (a) the monthly averaged solar flux, (b) The number of quiet days for which the digisonde observations are available and (c) the PO of the Post-Midnight spread F over Ascension Island and Jicamarca (PMSF-ASC and PMSF-JIC) for the quiet days (Ap < 12) of September of years 2010, 2011, 2012, 2014, 2019 and 2020

The monthly averaged solar flux unit (sfu) for September of the years 2010, 2011, 2012, 2014, 2019 and 2020 is shown in Figure 7.1a. These years are chosen depending on the availability of observations. The years 2011, 2012 and 2014 have sfu more than 100 whereas the years 2010, 2019 and 2020 have sfu below 75.

Figure 7.1b shows the number of quiet days digisonde observations are available and the inter-annual variability of post-midnight spread-F (PMSF) in September of all the above years. Over Jicamarca, the observations are available only for 7 days in the year 2010. In the year 2019, the observations are available for 22 and 21 days over Ascension Island and Jicamarca respectively. The PO of post-midnight spread-F over Ascension Island (PMSF-ASC) (81%) is found to be maximum in 2019 and minimum (6.9%) in 2010. The maximum PO of post-midnight spread-F over Jicamarca (PMSF-JIC) (56.3%) is observed in 2011 and minimum PO (14.3%) in 2010.

7.3.2 Duration of the spread F during September 2019
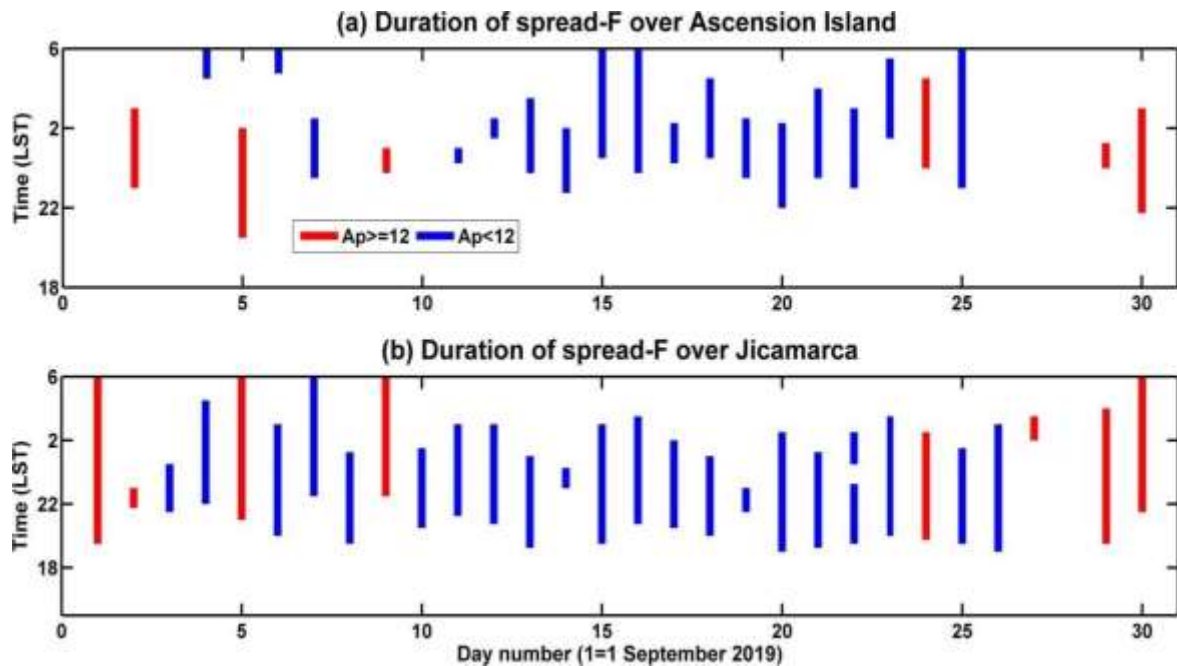
Figure 7.2: (a-b) Duration of the spread-F over Ascension Island and Jicamarca in September 2019. The red lines denote disturbed days ($A_p >= 12$)

Figure 7.2a-b shows the duration of spread-F obtained by manually screening the ionograms over Ascension Island and Jicamarca in September 2019. The red lines denote disturbed days ($A_p >= 12$). Over Ascension Island, the spread-F is formed mainly after 22:00 LST. The post-

81

sunset spread-F (PSSF) is almost absent in September 2019. However, the PSSF is found to be dominant over Jicamarca. The PMSF is observed only on 4th, 7th, 14th and 22nd September 2019 among the quiet days.

7.3.3 hmF$_2$ variations and their wavelet spectra

Figure 7.3a-b shows hourly mean hmF$_2$ variation over Ascension Island and Jicamarca in September 2019. There are data gaps for the day numbers 13–15 over Ascension Island and for day numbers 11–12 over Jicamarca. The hmF$_2$ is observed to be at higher heights (> 300 km) during midnight hours over Ascension Island.
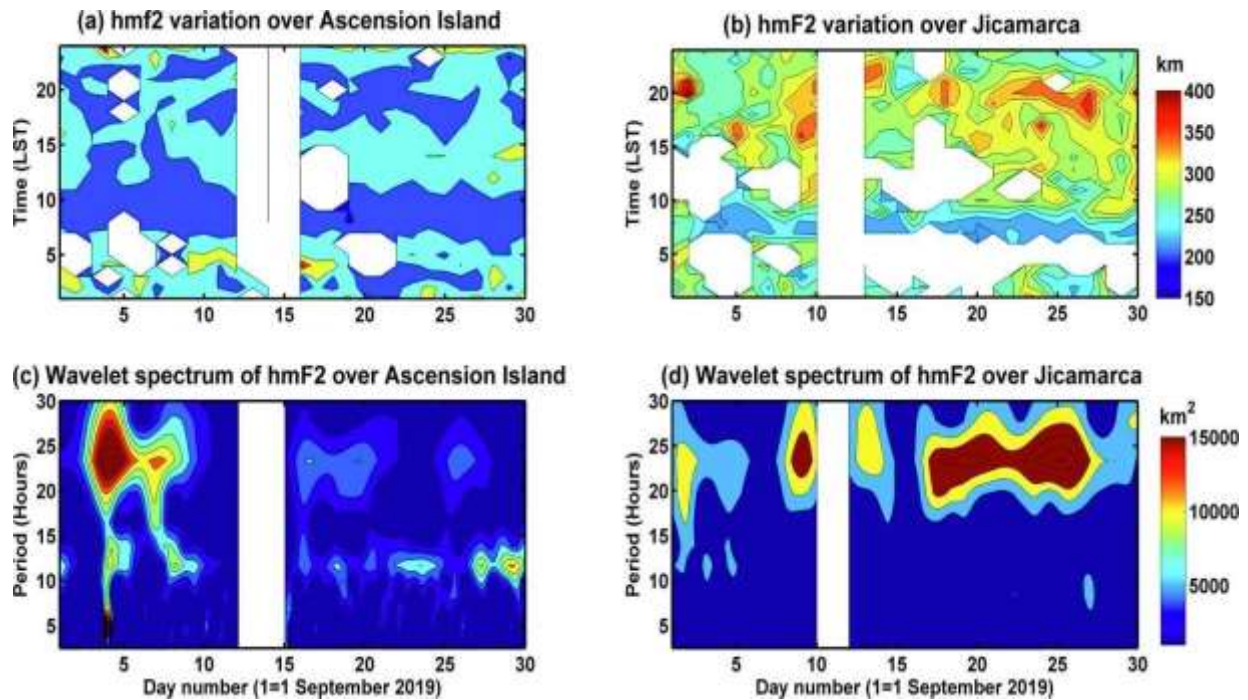
Figure 7.3: (a-b) Hourly mean variations of the hmF$_2$ over Ascension Island and Jicamarca and (c-d) Wavelet spectra of the hmF$_2$ over Ascension Island and Jicamarca in September 2019

Compared to Ascension Island, the hmF$_2$ is found to be at much higher heights from 13:00 LST over Jicamarca. In order to find the dominant periodicities in the hmF$_2$ variation, the hourly mean hmF$_2$ data over Ascension Island and Jicamarca for September 2019 are subjected to wavelet analysis with Morlet wavelet function as mother wavelet (Torrence and Compo, 1998). By decomposing a time series into time–frequency space, both the dominant modes of variability

and how those modes vary in time can be determined. The wavelets are localized functions, which can resolve frequency changes in short time periods. The wavelet spectra of the hourly mean hmF_2 variations over Ascension Island and Jicamarca are shown in Figure 7.3c-d. Both diurnal (24 h) and semi-diurnal (12 h) periodicities are observed over Ascension Island on day numbers 2–10, with relatively dominant diurnal periodicity. The semi-diurnal periodicity is observed to be more dominant during day numbers 18 to 30 of September 2019. However, the wavelet spectrum of the hmF_2 over Jicamarca reveals the presence of only diurnal periodicity and the semi-diurnal periodicity is almost absent.

7.3.4 Monthly mean diurnal variation of hmF_2 in September 2019
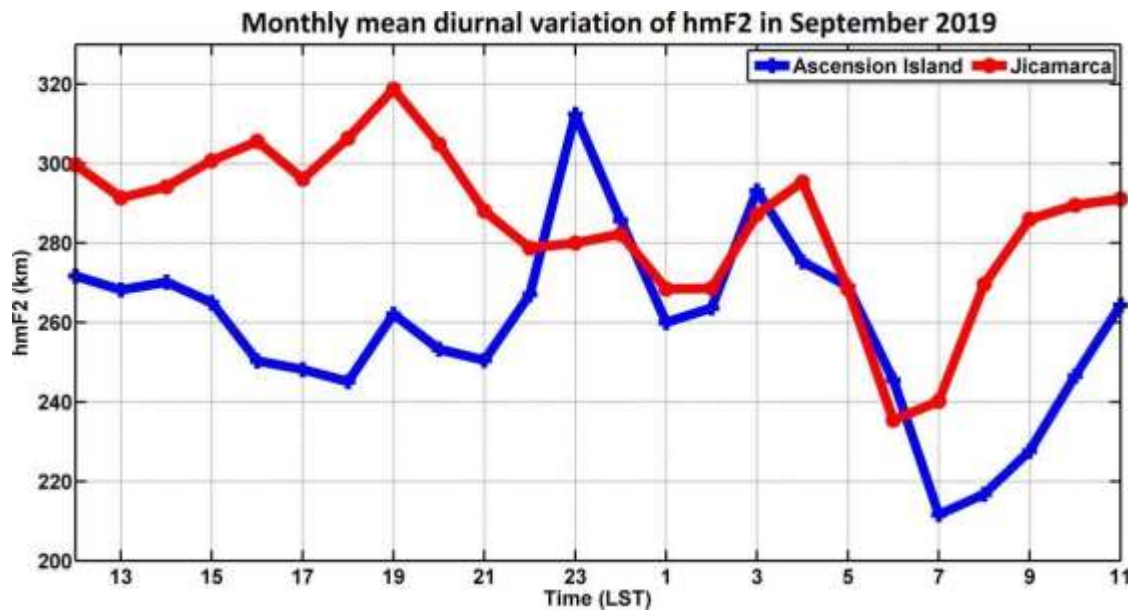
Figure 7.4: Monthly mean diurnal variations of hourly averaged hmF_2 over Ascension Island and Jicamarca in September 2019

The monthly mean diurnal variations of hmF_2 over Ascension Island and Jicamarca in September 2019 are shown in Figure 7.4. The hmF_2 over Jicamarca is found to be much higher (above 280 km) during 07:00–22:00 LST. The hmF_2 over Ascension Island is found to be lifted to higher heights (above 300 km) between 22:00 and 00:00 LST when PMSF is initiated. Similar lifting of the hmF_2 is not visible over Jicamarca. During the rest of the time (01:00–06:00 LST), the hmF_2 is at comparable heights over both Ascension Island and Jicamarca.

7.3.5 Monthly mean night-time variations of hpF and vertical drifts in September 2019

The monthly mean nighttime (18:00–06:00 LST) variations of hourly averaged hpF in September 2019 over Ascension Island and Jicamarca are shown in Figure 7.5a. The hpF is normally used for deducing the dynamic processes particularly, $\mathbf{E} \times \mathbf{B}$ drift after sunset (Maruyama et al., 2007). The hpF is found to be at higher heights (above 240 km) from 18:00 to 23:00 LST over Jicamarca whereas it is found to at lower heights (below 220 km) over Ascension Island. However, after 23:00 LST, the hpF over Ascension Island is at higher heights compared to that over Jicamarca and it reaches a maximum height (293 km) at 00:00 LST.
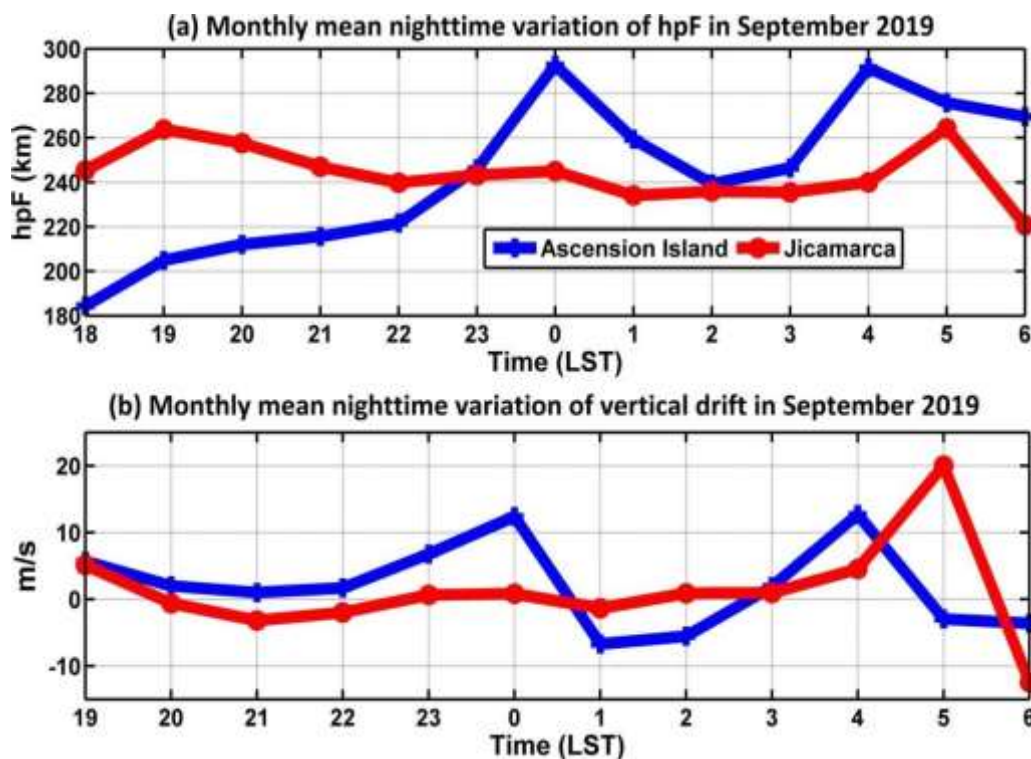
Figure 7.5: (a-b) Monthly mean nighttime (18:00–06:00 LST) variations of hourly averaged hpF and vertical drifts (m/s) over Ascension Island and Jicamarca in September 2019

The vertical drift of plasma is determined from the time derivative of hpF. The monthly mean diurnal variation of the vertical drift is obtained by averaging the diurnal variation of the vertical drift for all the quiet days. Thus obtained monthly mean diurnal variations of vertical drift over Ascension Island and Jicamarca for the month September 2019 are shown in Figure 7.5b. The

vertical drift over Ascension Island is upward (positive) before midnight (19:00–00:00 LST). The maximum vertical drift over Ascension Island is observed to be 12.4 m/s attained at midnight, whereas the vertical drift is nearly zero (0.8 m/s) over Jicamarca at midnight hours. Another upward drift is observed over Ascension Island after 03:00 LST. Over Jicamarca, the vertical drift continues to be close to zero even after midnight. The large increase in the PMSF echoes may be related to the tidal variabilities associated with the austral SSW event that occurred in September 2019 (Rao et al., 2020). To investigate this, TIMED-SABER temperature data are used.

7.3.6 Tidal variabilities in the upper mesospheric region
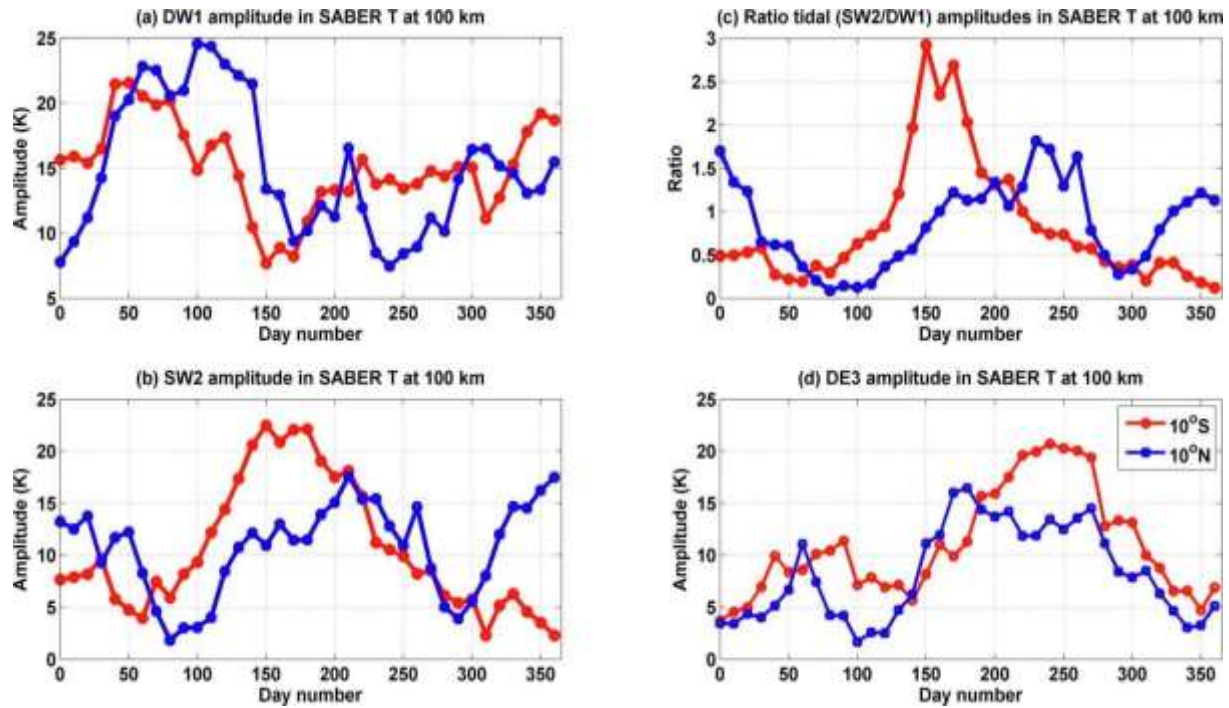
Figure 7.6: (a-d) Time variations of DW1, SW2, Ratio of tidal amplitudes (SW2/DW1) and DE3 in TIMED-SABER temperature at 98 km for the year 2019

The time variations of the migrating diurnal (DW1) and semi-diurnal (SW2) tidal amplitudes over 10°N and 10°S are shown in Figure 7.6 for the year 2019. The tidal variations presented here are at 10°N and 10° S, near to which, the dip equator is located in the respective longitudes of Ascension Island and Jicamarca. It appears that the tidal variations in the neutral atmosphere

couple with the equatorial ionospheric parameters through the dynamo mechanism, which is effective more at the dip equator, where the magnetic field is horizontal. The DW1 tide shows large amplitude in March equinox with amplitudes (>20 K) during day numbers 50–140. It shows multiple peaks with amplitudes greater than 15 K around day numbers 210, 300 and 360. At 10°S, the DW1 shows primary maximum in March equinox with larger amplitude around 20 K during day numbers 40–50 and 17 K on day number 60. It shows a broad secondary maximum with amplitude close to 15 K during day numbers 220–300 and it further increases to 20 K during day numbers 330–360. The SW2 at 10°N shows maximum amplitude during boreal summer (day numbers 140–260) and winter months (day numbers before 50 and after 320) with amplitudes greater than 10 K and minimum amplitudes below 5 K during day numbers 70–120 and around day number 290. At 10°S, the SW2 amplitude is greater than 10 K during day numbers 110–240 with amplitude increasing to more than 20 K during day numbers 140–180. To show the relative dominance of SW2 over DW1 the ratio of SW2 over DW1 is determined. The ratio is greater than 1 during day numbers 130–210 and even reaches 2 during day numbers 150–170 and it decreases to 0.5 on day number 270 and decreases further at 10°S. It is also greater than 1 during December-January. At 10°N, the ratio of SW2 to DW1 is around 1 during day numbers 160–210 and greater than 1 during 230–260 (mainly August-September) at 10°N. From these results, we can infer that the semi-diurnal tidal (SW2) amplitude is larger than DW1 during September 2019, when a major austral SSW has occurred. The eastward propagating diurnal tide with wavenumber 3 (DE3) shows almost similar variability at both 10°N and 10°S. It shows amplitudes greater than 10 K, however with slightly extended maximum and larger amplitudes at 10°S, where the amplitude is greater than 10 K during day numbers 180–300 and with amplitude of 20 K extending to the day numbers 200–270. This extended maximum with larger amplitudes is absent at 10°N. However, the DE3 amplitude at 10°N is greater than 10 K for the day numbers 160–280 with a maximum of 16 K around day number 180.

In the present study, the analysis of the digisonde observations over Ascension Island shows a high PO of PMSF in the quiet days of September 2019, when there is an onset of an austral SSW event. However, Jicamarca digisonde observations do not show any significant increase in the PO of the PMSF. In Chapter 4, it is suggested that the SW2 tide could dominate over DW1 tide during summer months, when the PMSF occurrence is maximum, whereas the DW1 could

dominate during equinox months (March-April and September-October) when the PSSF is normally observed to be more frequent. They also indicated the large PO of PMSF echoes observed normally during May-August; however the large PO extended further to the equinox month of September in the year 2019. Though large PO of PMSF is observed over Kototabang and Ascension Island, it is not observed over Jicamarca. In the present study, the wavelet spectrum of the hmF_2 shows a strong semi-diurnal periodicity (12 h) over Ascension Island and diurnal periodicity (24 h) over Jicamarca during September 2019. The high PO of PMSF and the semi-diurnal variation of hmF_2 indicate the lower atmospheric tidal forcing. The two-dimensional spectral analysis of the TIMED-SABER temperature measurement shows that the migrating semi-diurnal (SW2) tidal amplitude exceeds the migrating diurnal (DW1) tidal amplitude at 10°N, which is close to the dip equator in the Ascension Island longitude, whereas the DW1 dominates at 10°S over Jicamarca, which itself is dip equatorial station. In the year 2019, the DE3 tidal amplitudes are significantly larger during June-September at 10°S than at 10°N. Though the DW1 amplitude is less, the DE3 tidal amplitude at 10°S could be the reason for the dominant diurnal variation. Besides, it is also possible that non-linear interaction between DE3 and DW1 can generate eastward propagating semi-diurnal tide with wavenumber 2 (SE2) (Pancheva and Mukhtarov, 2012) which may reduce the amplitude of the semi-diurnal tidal variation due to phase cancellation with SW2. Pancheva et al. (2010) studied the climatology of the SE2 tide in the TIMED-SABER temperature and indicated that the SE2 tide is one of the dominant semidiurnal non-migrating tides. The present study reveals a strong semi-diurnal periodicity in hmF_2 over Ascension Island and dominant diurnal periodicity in hmF_2 over Jicamarca. It also reveals that the hpF over Jicamarca is at higher height during post-sunset hours, whereas the hpF over Ascension Island increases to higher heights around midnight hours during September 2019. Besides, the upward vertical plasma drift over Ascension Island is maximum around midnight hours, while the Jicamarca vertical drift is weaker in these hours. In Chapter 4, it is shown that the hmF_2 variations show semi-annual variation with higher heights during equinox months at post-sunset hours and they show annual variation with higher heights during June solstice at midnight hours. They attributed it to the enhancement of mesospheric SW2 during June solstice. As semi-diurnal tide has larger vertical wavelength, it can reach the thermosphere without much attenuation (Truskowski et al., 2014) and can cause semi-diurnal variation in the electric field through dynamo mechanism.

Stoneback et al. (2011) suggested that the semi-diurnal variation in the $\mathbf{E} \times \mathbf{B}$ drift could cause an upward drift near midnight. Consistent with their results, the results presented here also show the dominant semi-diurnal variations in the hmF_2 and the presence of upward drift close to or after midnight hours over Ascension Island in September 2019, whereas these features are absent over Jicamarca. This indicates that the migrating semi-diurnal tide plays a major role in the occurrence of the PMSF. The global tidal variations and the local geomagnetic geometry play a major role in the neutral ion coupling at a particular sector. However, more investigations are needed to understand how the neutral atmosphere–ionosphere coupling takes place.

7.4 Summary and Conclusions

The results obtained can be summarized as follows:

1. The PO of PMSF is observed to be high (around 81%) over Ascension Island during September 2019, when compared to the same month of other years. However, the high PO is not observed over Jicamarca.

2. The wavelet spectrum of hmF_2 shows a strong semidiurnal variation over Ascension Island, whereas diurnal variation is dominant over Jicamarca.

3. The high PO of PMSF and the semi-diurnal variation of hmF_2 indicate the lower atmospheric tidal forcing. It is observed that the migrating semi-diurnal (SW2) tidal amplitude exceeds the migrating diurnal (DW1) tidal amplitude in TIMED-SABER temperature at 10°N, which is close to the dip equator in the Ascension Island longitude, whereas the DW1 dominates at 10°S over Jicamarca, where the dip equator passes.

4. The PO of PMSF over each longitude is determined by the tidal variations over the latitude where the dip equator crosses through the longitude.

Chapter 8:

Role of thermospheric winds in the generation of post-midnight F-region irregularities

8.1 Introduction

Thermospheric winds play a major role in the electrodynamics of the Ionosphere-thermosphere coupled system. The thermospheric winds are generally generated due to pressure gradient forces that are driven by absorption of solar EUV radiation (Brum et al., 2012). They exhibit spatial and temporal variation which affects the thermosphere composition, ionosphere density, temperature and electrodynamics. The winds can move the F-region plasma along the magnetic field lines at the middle latitudes thereby changing the peak number density of the electrons (NmF$_2$) and the peak height of the F-region (hmF$_2$) (Rishbeth, 1972). These winds generate dynamo electric fields and hence influence the F-region electron density (Heelis, 2004). At high latitudes thermospheric winds are highly influenced by collisions with ions which are drifting under the electric and magnetic field (Richmond et al. 2003). Due to the momentum transfer the neutrals move similar way with the ions especially above 200 km (Richmond et al., 2003). The winds play important role in plasma transport as well. They generate dynamo electric fields and thereby influence the plasma instabilities as well (Kelley, 2009).

The thermospheric winds are one of the most significant as well as the least sampled contributing factor towards the Ionospheric dynamics. The pre-reversal enhancement (PRE) of the dynamo eastward electric field plays a key role in the generation of the F-region irregularities during the post-sunset hours. The eastward F-region neutral wind is considered to be the main driver of the PRE (Eccles et al., 2015). Model results have shown that E-region neutral wind can modulate PRE (Millward et al., 2001). The F-region eastward neutral winds during sunset can trigger the post-sunset equatorial spread-F (Kudeki et al., 2007). The F-region irregularities observed during the midnight hours (post-midnight F-region irregularities) are also expected to be influenced by the thermospheric winds. Rayleigh Taylor Instability (RTI) is the widely accepted mechanism for the generation of the F-region irregularities. Huba and Krall (2013) have investigated the effect of meridional winds on the growth rate of the RTI using SAMI3/ESF

89

model. The equatorward winds at low latitudes (non-zero magnetic inclination) can destabilize the bottom of the F-region (Maruyama et al., 2009). The thermospheric winds are important inputs in many ionospheric models hence more statistical information regarding thermospheric winds could be helpful in better prediction of the thermosphere-ionosphere system. The study of thermospheric winds is also significant for understanding the global variation in thermospheric composition. Most of the climatological studies have been conducted over the American, Asian longitudinal sectors as well as the European mid-to-high latitude regions (e.g., Fisher et al., 2015, Yu et al., 2014, Xu et al., 2019). However, routine observations of the thermosphere globally were limited. Ground based measurements from Fabry Perot Interferometer (FPI) located at various places have contributed to our understanding of the upper atmospheric dynamics. However, these optical measurements are limited to cloud free nights and the places with such instruments are also limited over the globe (Drob et al., 2008). Interferometric measurements of winds can be done from satellites as well (Shepherd et al., 1993); Space born accelerometers (Liu et al., 2006) and spectrometers (Spencer et al., 1982) can also give wind observations. Information regarding winds can be obtained from ionospheric measurements (Miller et al., 1986). But the errors are comparatively large to the direct wind measurements due to the assumptions made and the uncertainties in the model parameters (Buonsanto et al., 1997; Buonsanto and Witasse, 1999). Models also exist which can be used to determine the thermospheric winds like the empirical series of wind models (HMWs) (Drob et al., 2008) which uses ground and space-based data and then interpolate between data gaps. Models like TIEGCM, TGCM, and WAM can estimate the thermospheric winds after coupling several models of different parts of the atmosphere (Richmond et al., 1992, Ma and Schunk, 1995, Akmaev et al., 2008). However, the propagation of errors can give rise to unreliable results.

The Ionospheric Connection Explorer (ICON) satellite recently launched by NASA has Michelson Interferometer for Global High-resolution Thermospheric Imaging (MIGHTI) aboard which provides the thermospheric wind observations. The ICON also has an Ion Velocity Meter (IVM) which measures the plasma drift. In the present study, these are analysed to investigate the seasonal and inter-annual variations of the winds and the plasma drifts for solar minimum years 2020 and 2021.

8.2 Data and Methodology

8.2.1 ICON-MIGHTI thermospheric winds

We have used thermospheric neutral winds from the MIGHTI (Englert et al., 2017) onboard NASA's ICON (Immel et al., 2018) satellite. We are analysing only red line emission of MIGHTI level 2.2 data products. We have used component of the wind in the magnetic meridional and zonal direction for the years 2020 and 2021.

8.2.2 ICON-IVM plasma drifts

From ICON-IVM for the present study we have utilised the parameters 'Equatorial meridional ion velocity' and 'Equatorial zonal ion velocity'. They are the plasma velocity along local magnetic meridional direction, perpendicular to geomagnetic field and within local magnetic meridional plane, field-line mapped to apex/dip equator.

8.3. Results and Discussions

8.3.1 Zonal mean of thermospheric meridional winds

The diurnal variation of the zonally averaged meridional winds of good wind quality data (ICON_L22_Wind_Quality is equal to one) in the northern geomagnetic low latitudes (10ºN-20ºN) for the years 2021 and 2020 averaged from 200 km to 250 km are shown in Figure 8.1a-b. Both 2020 and 2021 are solar minimum years with the solar flux units of 66.3475 sfu and 73.6867 sfu respectively. From October to December 2020 and 2021, the winds are positive (poleward) with magnitude greater than 20 m/s. In 2021 poleward winds are observed from January to April, whereas from January to April 2020, the winds are weakly poleward after 20:00 LST and they change to equatorward (negative) after 22:00 LST. In 2020, the magnetic meridional winds are equatorward from May to August. However in 2021 the winds are equatorward during 10:00-20:00 LST and they become poleward after 20:00 LST with values ranging from 0 to 10 m/s. In 2021 the winds are more positive (strongly poleward) compared to 2020.

Figure 8.1: Zonal mean of ICON-MIGHTI magnetic meridional winds over northern geomagnetic low latitude 10ºN-20ºN for the years 2020 and 2021

8.3.2 Longitudinal variability of thermospheric meridional winds

The longitudinal variabilities of magnetic meridional winds for summer (May-July), winter (November-February), spring equinox (February-April) and fall equinox months (August-October) are depicted in Figures 8.2 and 8.3. The wind data are binned for every 20º longitudes like 0º-20ºE, 15º-35ºE, 30º-50ºE…to obtain winds centered at 10ºE, 25ºE,40ºE…etc and then the local time hourly mean is determined for different longitudes for each season.

Comparison of the longitudinal variation of magnetic meridional winds from 10:00 to 05:00 LST over low geomagnetic latitudes (10ºN-20ºN) during the summer and winter of solar minimum years 2020 and 2021 is shown in Figure 8.2. In the summer 2020, the magnetic meridional winds

are equatorward (-ve) from 11:00 to 23:00 LST with magnitudes greater than 30 m/s from 15:00 to17:00 LST. After 23:00 LST, the winds are poleward but with magnitudes less than 10 m/s. The meridional winds in summer 2021 are equatorward from 11:00 to 18:00 LST irrespective of the longitudes and after 19:00 LST, the winds are weakly poleward. However, in winter, the winds are poleward with magnitudes greater than 40 m/s.
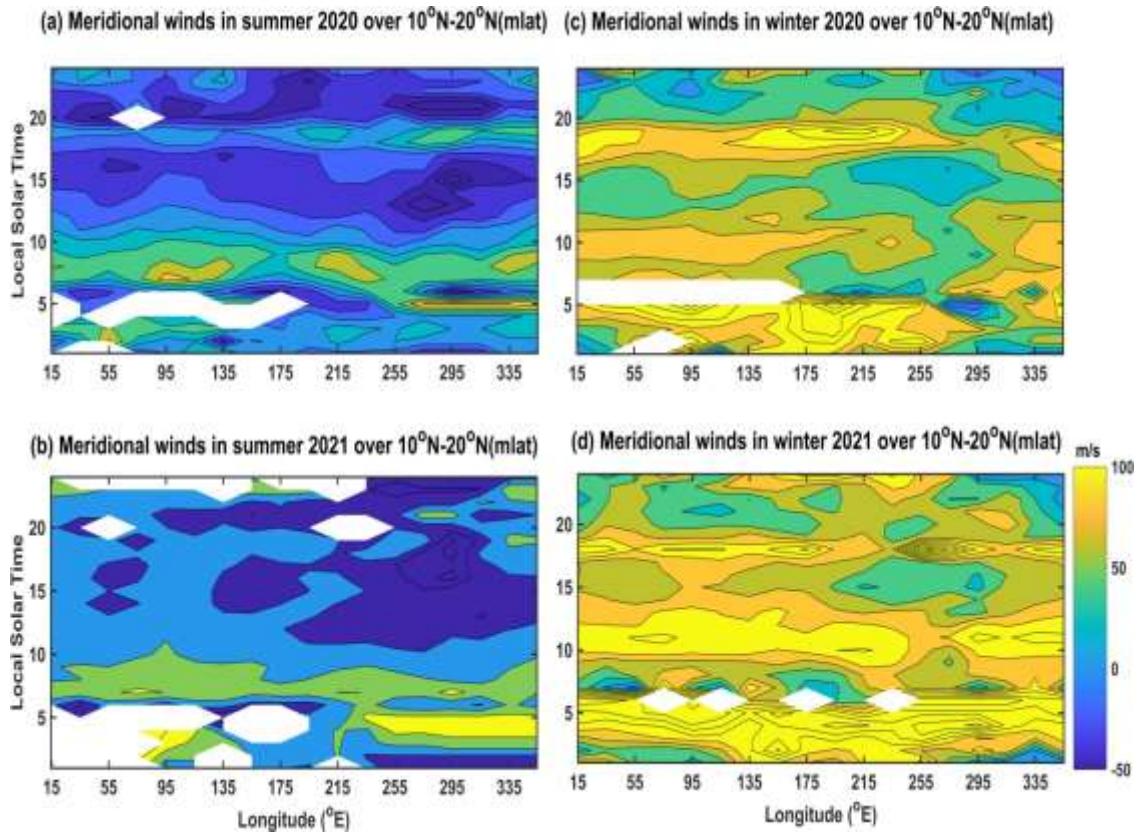
Figure 8.2: Longitudinal variability in ICON-MIGHTI magnetic meridional winds over northern geomagnetic low latitudes 10ºN-20ºN for the summer (May-June-July) and winter (November - December-January) months of years 2020 and 2021

Magnetic meridional winds in the spring and fall equinox months are compared in Figure 8.3. The meridional winds in longitude band 10ºE - 190ºE are weakly poleward (< 10m/s) from 10:00 to 19:00 LST in the spring equinox of 2020. After 19:00 LST, the winds turn equatorward and persist till 23:00 LST. In the longitude band 190ºE -360ºE, the meridional winds are equatorward from 10:00 LST to 17:00 LST and weakly poleward later. The meridional winds are poleward in 2021 irrespective of local solar time and longitudes in spring equinox. In all longitudes equatorward winds are observed in fall equinox season from 13:00 LST to 17:00 LST in 2020

and 15:00 LST to 17:00 LST in 2021. After 17:00 LST weak poleward winds are present in 2020 whereas winds are comparatively strong in 2021. In short, although there is an inter-annual variability, the meridional winds are less poleward or equatorward in summer and strongly poleward in winter.
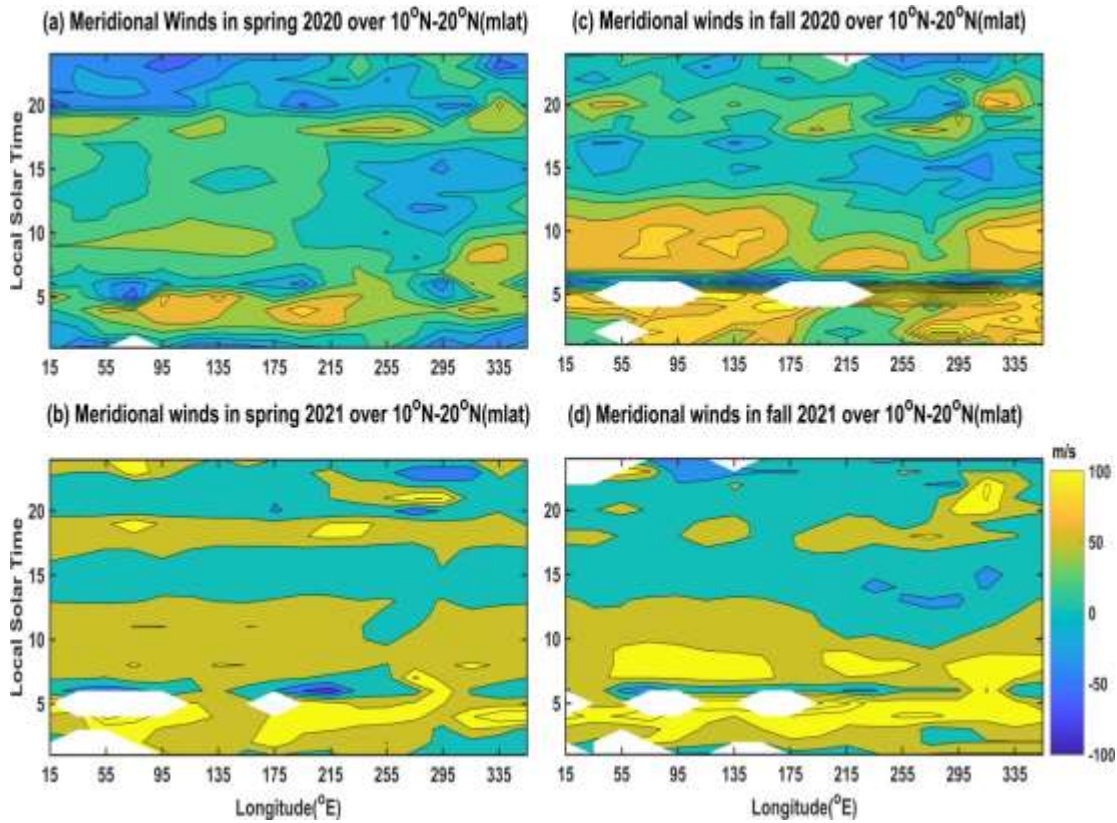
Figure 8.3: Longitudinal variability in ICON-MIGHTI magnetic meridional winds over northern geomagnetic low latitudes 10ºN-20ºN for the spring equinox (February -March-April) and fall equinox (August-September-October) months of years 2020 and 2021

8.3.3 Zonal mean of thermospheric zonal winds

In Figure 8.4a-b, the hourly averaged zonal mean of zonal winds over the northern geomagnetic low latitudes (10ºN-20ºN) is shown for the years 2020 and 2021. The winds are westward during 10:00-16:00 LST and eastward during 19:00-05:00 LST in October-April 2020. From June to September 2020, the winds turn westward earlier from 02:00 LST. In 2021, the zonal wind variations are more or less similar to the year 2020. However, the zonal winds are less eastward in January to March 2021 (magnitude ~ 70m/s) during 22:00-05:00 LST, compared to the year

2020, when the winds have magnitude ~100 m/s. October to April months the eastward winds during nighttime are stronger (50-100m/s) whereas during summer months (May to July) the winds are weakly eastward or even turned westward after 20:00 LST. These results suggest that the zonal wind, in general, is westward during daytime and eastward during nighttime.
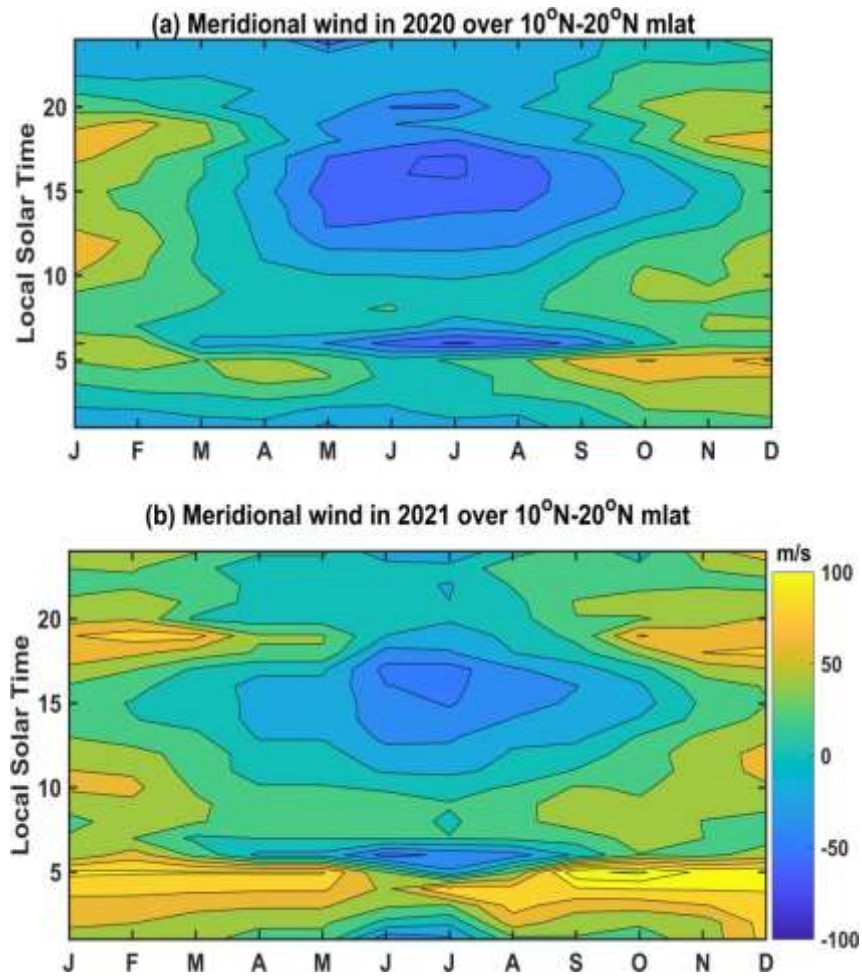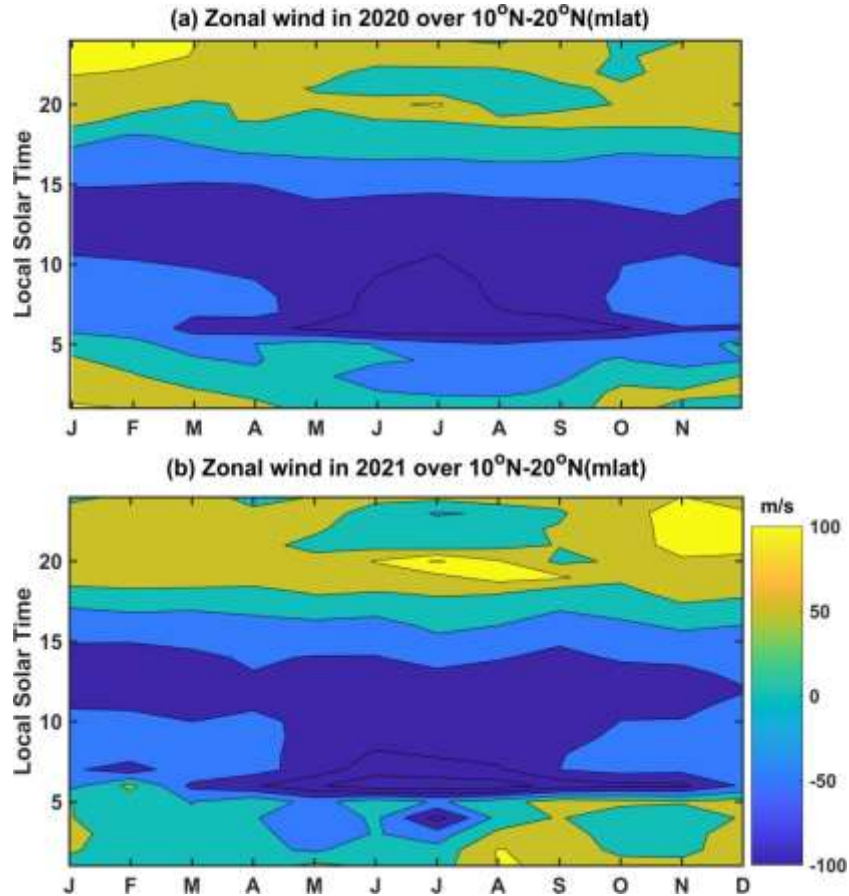

Figure 8.4: Zonal mean of ICON-MIGHTI magnetic zonal winds over northern geomagnetic low latitude 10ºN-20ºN for the years 2020 and 2021

8.3.4 Zonal mean of vertical plasma drifts

The hourly averaged the zonal mean of the ICON - IVM equatorial ion vertical drifts at an altitude of ~600 km for the years 2020 and 2021 over the dip equator (5ºN-5ºS) are shown in Figure 8.5. We have selected IVM data with good quality (IVM_L27_DM_Flag <1 and IVM_L27_RPA_Flag<1) and geomagnetically quiet days ($A_p < 12$). During 06:00-10:00 LST, the observations are not available. During the daytime (10:00-15:00 LST), the drift is upward (positive) for all the months with a maximum magnitude of around 50 m/s at 12:00 LST. In

January-February 2020, the drift is upward during 22:00-02:00 LST with a maximum of 15 m/s at 00:00 LST. However, in March-May 2020, the drift is downward during 16:00-05:00 LST. In June-July 2020, the drift is upward throughout the local time except during 03:00-05:00 LST, when the drift is downward.
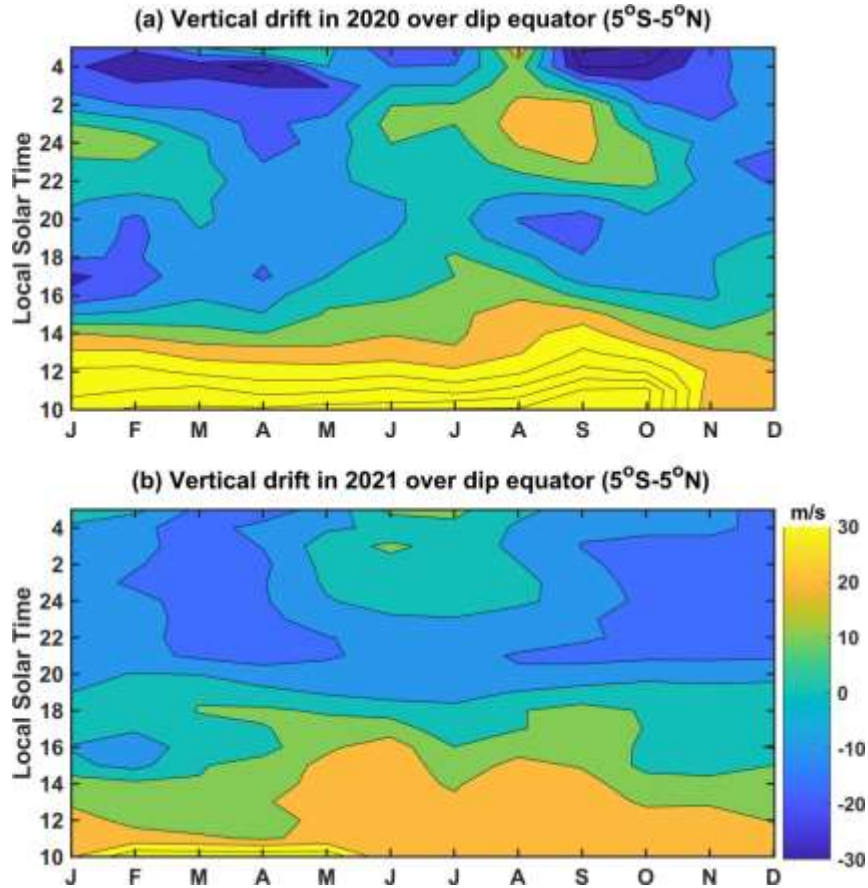
Figure 8.5: Zonal mean of ICON-IVM equator ion vertical drifts for quiet days with Ap < 12 over dip equator (5ºS-5ºN) for the years 2020 and 2021

In August-September 2020, the drift is upward from 22:00 to 02:00 LST with maximum magnitude of 24 m/s at 01:00 LST. In October to December, the drift is downward (negative) after 16:00 LST. In all the months of 2021, the drift is upward during 10:00-18:00LST. However, the upward drifts, which are observed during 22:00-02:00 LST in January-February 2020, are not observed in 2021. After 18:00 LST the drift is downward till 05:00 LST during January-April and September-December of 2021. In May to August 2021, the drift is upward between 00:00 LST and 05:00 LST. The upward drift after 22:00 LST is a common feature in summer 2020 and 2021. Downward drifts over the dip equator is also prevalent after 19:00 LST

during November-December of 2020 and 2021.To summarize, the vertical drifts are upward during night-time in summer, whereas it is downward in winter. Daytime vertical drifts are upward in all seasons of 2020 and 2021.

8.3.5 Longitudinal variability of vertical plasma drifts
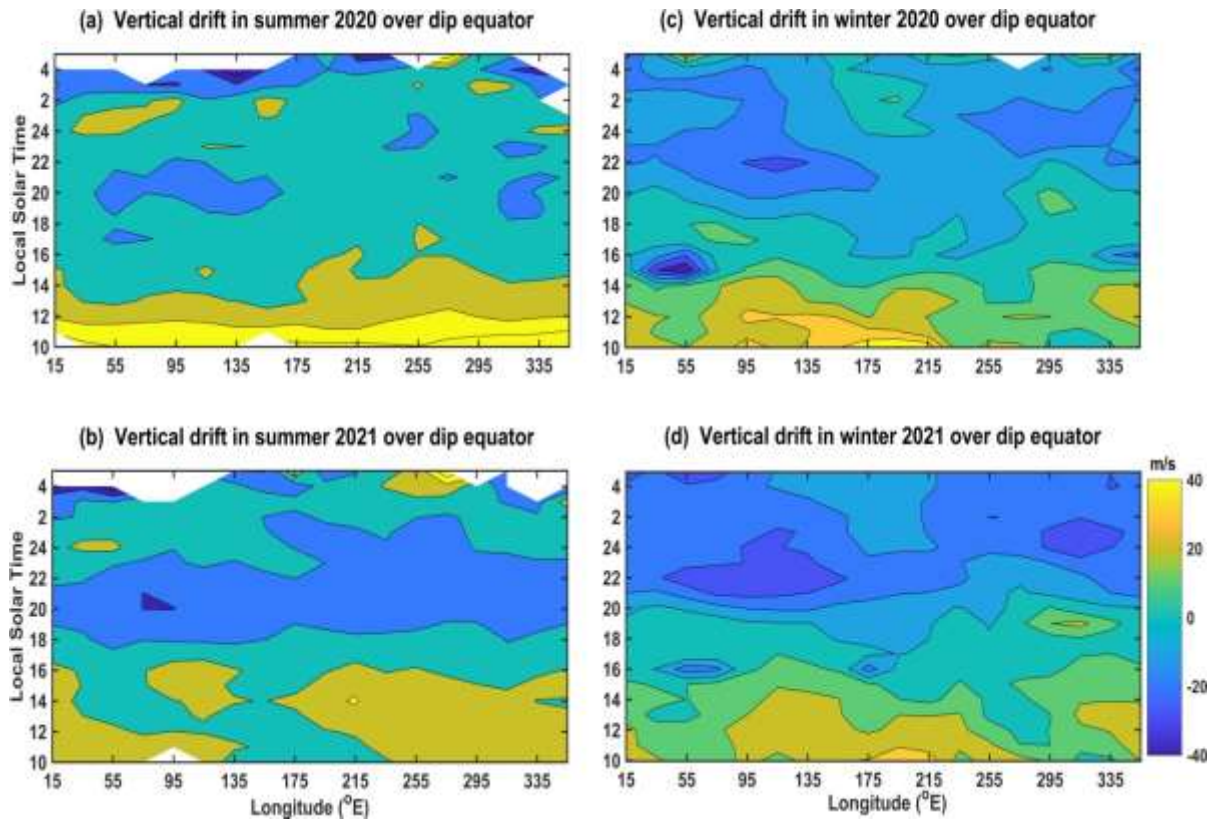
Figure 8.6: Longitudinal variability in ICON-IVM equator ion vertical drifts for quiet days (Ap < 12) over dip equator (5ºS-5ºN) for the summer (May-June-July) and winter (November - December-January) months of years 2020 and 2021

The seasonal variations in the vertical drifts over the dip equator (5ºN-5ºS) are investigated as done for the ICON-MIGHTI winds. In Figure 8.6, the longitudinal variation of vertical drifts in the quiet days (A_p < 12) of summer and winter are shown. In summer 2020, the vertical drift is upward during daytime between 10:00 LST and 02:00 LST with a maximum velocity during 10:00-14:00 LST in all the longitudes. In longitudes from 40ºE to 190ºE the drift is downward (negative) from 19:00 LST to 22:00 LST. Upward drift is common in summer of solar minimum years. In 2021, the vertical drift is upward from 10:00 to 18:00 LST during summer and winter.

The vertical drifts are upward after midnight hours (after 23:00 LST) in summer 2021.
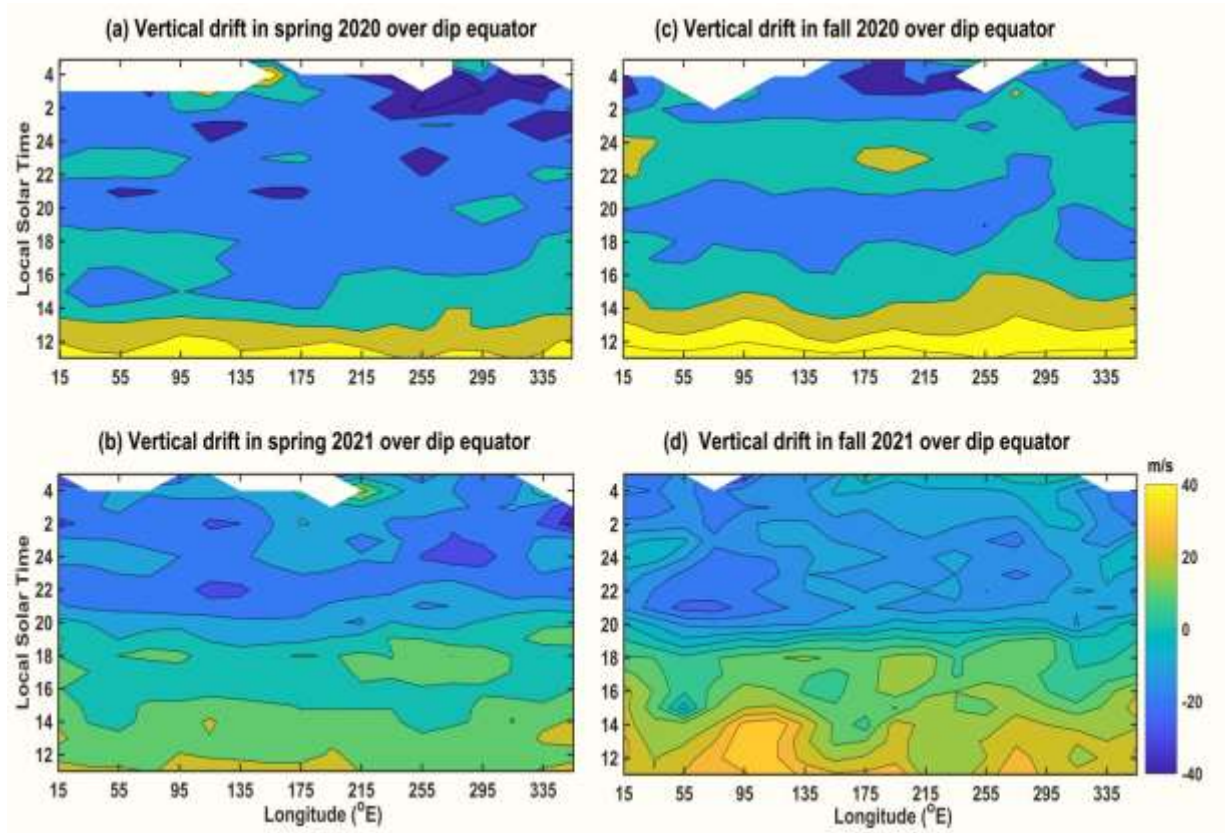
Figure 8.7: Longitudinal variability in ICON-IVM equator ion vertical drifts for quiet days (Ap < 12) over dip equator (5ºS-5ºN) for the spring equinox (February-March-April) and fall equinox (August-September-October) months of years 2020 and 2021

In winter upward drifts are common during 10:00-16:00 LST in 2020 and 2021 in all longitudes. Maximum upward drifts are present between 10:00 LST and 13:00 LST after which the vertical drift is reduced and turned negative (downward) after 19:00 LST. Longitudinal variation of the vertical plasma drifts for equinox months are presented in Figure 8.7. Upward (positive) drifts are present in 10:00-15:00 LST during spring equinox of 2020 whereas upward drifts is extended till 19:00 LST in 2021. Downward drifts are present after 19:00 LST in spring 2020 and 2021 in all longitudes.

In 2020 and 2021, vertical drifts are positive (upward) during 11:00-19:00 LST irrespective of the longitude. However, an exceptional upward drift is present during 22:00-01:00 LST in fall equinox of 2020. The vertical drifts are negative during night-time (19:00-05:00 LST)

in the fall equinox of 2021. Longitudinal variability generally exists in the upward vertical drifts during night-time.

8.3.6 Zonal mean of zonal plasma drifts
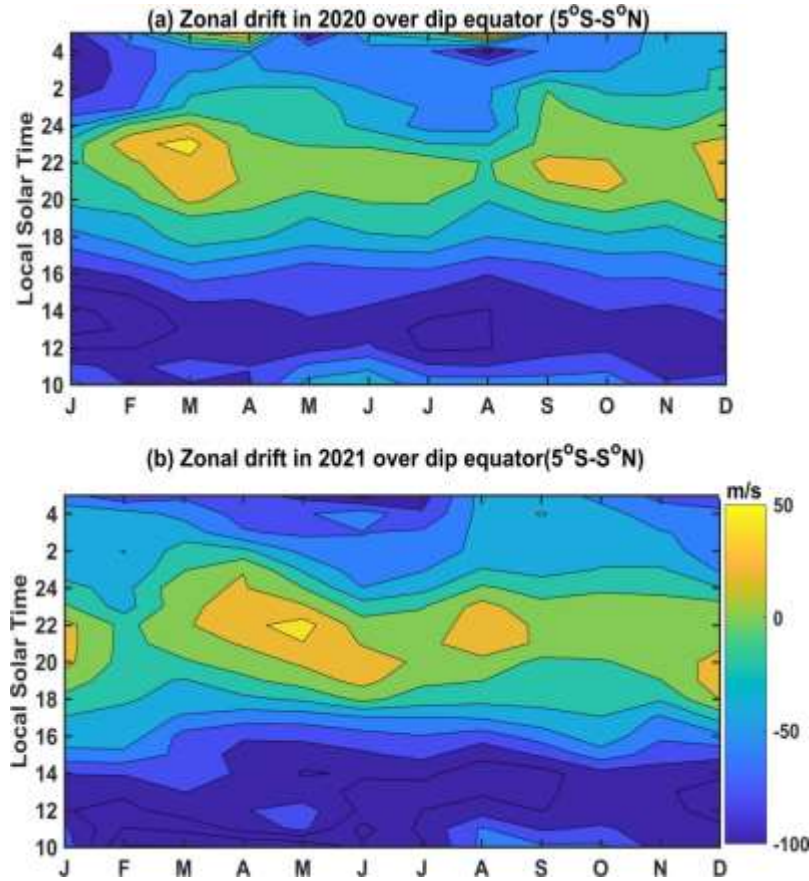
Figure 8.8: Zonal mean of ICON-IVM equator ion zonal drifts for quiet days (Ap < 12) over the dip equator (5ºS-5ºN) for the years 2020 and 2021

The ICON-IVM zonal drifts at ~600 km for the years 2020 and 2021 are investigated for the geomagnetically quiet days ($A_p < 12$). The zonal mean of the zonal drifts over the dip equator (5ºS-5ºN) is shown in Figure 8.8a-b. From the Figure, we can infer that the variations of the zonal drifts are similar in both 2020 and 2021. They are much stronger than vertical drifts with magnitudes in the range 50-100 m/s.

In 2020 from 10:00 LST to 19:00 LST and 00:00 LST to 05:00 LST strong westward drifts are observed with magnitude greater than 50 m/s. From 20:00 LST to 23:00 LST, the drifts turn

eastward but with magnitude much less compared to the westward drifts. These results suggest that the westward drifts (>50m/s) are larger than eastward drifts (<40m/s).

In the present study, the F-region winds and ion drift measurements from the ICON-MIGHTI ICON-IVM are used to study their seasonal and inter-annual variations. The seasonal variation of the F-region neutral winds at 200-250 km altitude over northern geomagnetic low latitudes (10ºN-20ºN) for the solar minimum years 2020 and 2021 show that during nighttime, the meridional winds are equatorward in summer months and consistently poleward in winter months. The meridional winds show large inter-annual variability. The poleward winds are dominant in the spring and fall equinox seasons in the year 2021, but they are weaker in the year 2020 after 22:00 LST. This could be due to the relatively higher solar flux in the year 2021. The zonal winds are westward in summer and winter during day time. However, during nighttime, weak eastward winds are observed in summer and they become westward after midnight hours. In winter, the winds are eastward during nighttime. The westward zonal winds are dominant during daytime hours irrespective of the season or longitudes. The zonal winds do not show any noticeable inter-annual variability except that the winds are westward throughout the day at some longitudes in summer 2020, whereas they are eastward between 19:00 LST and 22:00 LST at all longitudes in summer 2021. Consistent with the results presented here, using CHAMP satellite accelerometer measurements, Liu et al. (2016) reported that the zonal winds were eastward throughout the night except around the June solstice, where it even decreased to zero or turned westward in the post-midnight sector at solar minimum conditions.

Corresponding ICON-IVM vertical and zonal drifts for quiet days ($A_p < 12$) are analysed over the dip equator for the solar minimum years of 2020 and 2021. It is observed that the vertical drifts are upward during daytime irrespective of the season. The nighttime vertical drifts are downward (negative) in winter and spring equinox. However, in fall equinox, they show inter-annual variability with upward drifts in 2020 and downward drifts in 2021. Unlike thermospheric winds, the vertical drifts show large longitudinal variations. The upward drift due to the PRE, observed normally during the post-sunset hours (18:00-19:30 LST) in digisonde and incoherent scatter radar measurements, is not detected by the IVM. It could be because both 2020 and 2021 are solar minimum years and the measurements are made at an altitude of ~600 km. Vertical plasma drifts display semi-diurnal variation in summer and fall equinox of

2020, whereas they exhibit diurnal variation in winter and spring equinox. The zonal winds and zonal plasm drifts exhibit diurnal variation irrespective of the season.

Many earlier studies have shown the importance of the thermospheric winds in the generation of the ionospheric irregularities, which have a significant impact on the communication and navigation systems. Delayed occurrences of these irregularities (post-midnight F-region irregularities) are observed during the June solstice months of solar minimum years (e.g., Patra et al., 2009; Otsuka et al., 2009; Li et al., 2012; Yizengaw et al., 2013). The abatement of the poleward winds or equatorward winds is considered to be behind the enhanced chemical recombination and the horizontal plasma flux (Nicolls et al., 2006) which further uplifted the F layer to higher heights at midnight hours leading to the post-midnight F-region irregularities.

Thermospheric winds may play a key role in both formation as well as suppression of these irregularities. The F-region eastward neutral winds during sunset can trigger the post-sunset ESF (Kudeki et al., 2007). Krall et al. (2009) using SAMI3/ESF model showed that a constant meridional wind of 60 m/s can stabilize ESF. Using model simulations, Huba et al. (2010) have shown that post-midnight enhancement of the upward $\mathbf{E} \times \mathbf{B}$ drift can be the result of strong eastward winds between 150 km and 250 km. In the present study, the MIGHTI wind observations reveal that the thermospheric winds are indeed equatorward during June solstice months of solar minimum years when the PO of the post-midnight F-region irregularities is maximum. The upward drift of the plasma can generate irregularities in the F-region. The ICON-IVM plasma drifts are also observed to be upward during nighttime (after 22:00 LST). The zonal winds are westward or weakly eastward in the nighttime for summer season (2020 and 2021) as well as during the fall equinox season of 2020. Upward drifts are also observed in theses seasons. The daytime zonal wind is found to be consistently westward than the nighttime zonal wind.

Dao et al. (2017) have demonstrated that equatorward winds could be responsible for the generation of the post-midnight plasma bubbles. They suggested that the eastward electric current driven by the equatorward winds could also contribute to the generation of post-midnight F-region irregularities. Huba and Krall (2013) also found that the equatorward winds could destabilize the F-region generating favourable conditions for the growth of plasma bubbles. The parallel component of the neutral wind along the magnetic field carries the plasma to higher

heights thereby reducing the Pedersen conductivity and destabilizing the bottomside F-region. Eastward Pedersen current induced by the equatorward winds can increase the growth rate of the RTI.

These results along with the results obtained in the present study suggest the potential role of equatorward winds particularly on the generation of the post-midnight F-region irregularities. However, more observations are required to understand the role of zonal winds on the F-region irregularities.

8.4 Summary and Conclusions

The results obtained can be summarized as follows.

1. ICON-MIGHTI meridional winds are equatorward (negative) or weakly poleward (positive) in summer 2020 and 2021. Poleward (positive) winds are predominantly present in winter. The meridional winds are poleward throughout the day in both spring and fall equinoxes of 2021. However, in the year 2020, the winds are weakly poleward and even changed to equatorward during midnight hours.

2. The ICON-IVM vertical ion drifts over the dip equator are upward (positive) during daytime irrespective of season. The nighttime vertical drifts are upward in summer and downward in winter. The vertical drifts are downward during nighttime in equinox except in the fall equinox of 2020, when the drifts are observed to be upward after 22:00 LST.

3. Zonal winds are westward (negative) during daytime hours (10:00-17:00 LST) in all seasons. During nighttime, eastward winds are observed in winter and equinox. After midnight hours, zonal winds are weakly eastward and even turned to westward in summer.

4. As expected, the zonal winds and zonal drifts show similar variations, as the zonal plasma drifts are mainly driven by the thermospheric zonal winds.

5.   The vertical drifts exhibit semi-diurnal variation only in summer of both 2020 and 2021 and fall equinox of 2020, whereas diurnal variation is dominant in zonal drifts irrespective of the season.

6.   The equatorward winds during nighttime can lift the plasma to higher heights thereby the ion neutral collision frequency is reduced and hence the growth rate of RTI will increase leading to the generation of the post-midnight F-region irregularities. Moreover during midnight hours of boreal summer months the vertical plasma drifts are found to be upward when the PO of PMF is observed to be maximum.

The longitudinal variation of the equatorial ionosphere can be attributed to the thermospheric winds as well as the tides propagating from the lower atmosphere. The thermospheric wind patterns can be influenced by the upward propagating tides as well.

Chapter 9:

Summary and Scope for future work

9.1 Summary

The F-region irregularities are crucial part of the ionospheric investigations as they can impact the communication and navigation systems. Equatorial plasma bubbles (EPBs) are considered to be the cause of the F-region irregularities. These anomalies are generated due to the Rayleigh Taylor Instability (RTI). They are called post-sunset (PSF) and post-midnight F-region irregularities (PMF) depending on the time when they are observed. These post-midnight F-region irregularities are generated usually around midnight hours (after 22:00LST). The PMF have different occurrence characteristics compared to the PSF. The EAR observations of the F-region irregularities show that the percentage of occurrence (PO) of these irregularities maximises during June solstice months of solar minimum years. They have inverse relationship with solar activity whereas PO of post-sunset irregularities increases during solar maximum years. The PO of the PSF maximises during equinox months and PMF maximises during June solstice months of solar minimum year over Jicamarca (a dip equatorial station). Over Ascension Island, where magnetic declination is negative, the PO of post-midnight spread-F maximises during November to February (austral summer months).

The possible generation mechanisms or conditions under which the growth rate of the RTI increases during midnight hours which can lead to these post-midnight F-region irregularities are investigated. The occurrence of these irregularities is a common feature of solar minimum years, which can indicate lower atmospheric forcing. The height of the peak electron density of the F-region (hmF_2) obtained from ionosonde is found to be at higher heights during post-midnight hours over Kwajalein Island (a dip equatorial station) in June solstice months of solar minimum years. In equinox months, when the PO of post-sunset irregularities is large, the uplift of hmF_2 is between 18:00 LST and 19:30 LST. The lifting of the F-region during midnight hours in boreal summer will create conditions favourable for the generation of the RTI.

The interaction between various layers of atmosphere is facilitated by the atmospheric tides, which are periodic oscillations of the atmosphere. It is investigated how these tides can contribute to the generation of the post-midnight F-region irregularities. The study revealed that migrating westward propagating semi-diurnal tide (SW2) is dominant during boreal summer months (June solstice months) when the PO of the post-midnight F-region irregularities are large and migrating westward propagating diurnal tidal (DW1) amplitude is maximum during equinox months when the post-sunset irregularities are predominant. The SW2 tidal amplitude is also found to be enhanced during Sudden Stratospheric Warming (SSW) events.

The occurrence of these irregularities during SSW is further investigated to examine the effect of the lower atmosphere processes on the ionospheric irregularities. During SSW, the SW2 tidal amplitudes are observed to increase and are reported to be due to increase in the ozone concentration. The PO of the post-midnight F-region irregularities from EAR Kototabang is observed to increase during SSW which confirms the influence of semi-diurnal tide (SW2) on the generation of these irregularities. Austral SSWs are rare compared to the Arctic SSWs. However, recent austral SSW event in September 2019 gives an opportunity to investigate their impact on the F-region irregularities.

The PO of post-midnight F-region irregularities over Kototabang from 2010 to 2019 revealed an anomalous increase in their occurrence during September 2019 when an austral SSW has occurred. Inter-annual variability also showed that PO is the largest in September 2019. The tidal variabilities are investigated during austral SSW at 10°N (where dip equator passes over Kototabang longitude sector). Enhancement in the amplitude of SW2 is not observed in September 2019 at 10°N because the austral SSW was a minor event. Generally, DW1 amplitude has two equinoctial maxima however; there has been a reduction in the amplitude of the DW1 during September 2019. The relative enhancement of SW2 over DW1 is noted during Austral SSW. Moreover, the wavelet spectrum of hmF_2 shows semi-diurnal (12 hr) periodicity. The F layer (hpF) is also observed to be lifted to higher heights during midnight hours in September 2019. Hence, the relative enhancement of the SW2 over DW1 could have turned the electric field eastward during midnight hours thereby lifting the F layer to higher heights and creating conditions favourable for RTI to develop post-midnight F-region irregularities.

Longitudinal variability in the occurrence of the post-midnight F-region irregularities is investigated using ionosonde observations over Ascension Island and Jicamarca during austral SSW of 2019. The PO of post-midnight spread-F is showing maximum occurrence in September 2019 over Ascension Island (80%) whereas over Jicamarca the PO is very small. Tidal variabilities at 10°N and 10°S (Jicamarca latitude) are examined. During midnight hours, the F layer is lifted to higher heights over Ascension Island whereas F layer is at lower heights over Jicamarca. The wavelet spectrum of hmF_2 over Ascension Island also shows dominant semi-diurnal periodicity (12 hr) whereas; over Jicamarca diurnal (24 hr) variation is dominant. The amplitude of SW2 has enhanced at 10°N whereas at 10°S such an enhancement is not observed during September 2019. Moreover, DW1 amplitude has decreased at 10°N during austral SSW. The increase in the amplitude of SW2 at 10°N has led to large PO of post-midnight F-region irregularities over Ascension Island. Longitudinal variabilities in the occurrence of post-midnight F-region irregularities can be attributed to tides.

Apart from tides other generation mechanisms for post-midnight F-region irregularities are investigated. Thermospheric winds play a key role in ion-neutral coupling. The thermospheric wind variations during solar minimum years (2020 and 2021) are analysed using ICON-MIGHT. The study shows that the thermospheric meridional winds are equatorward (negative) or weakly poleward (positive) in boreal summer over northern low geomagnetic latitudes (10°N-20°N) whereas strong poleward winds are observed in winter. Thermospheric winds show inter-annual variability for equinox months. In 2020, the night-time meridional winds are weakly poleward and even turned equatorward during post-midnight hours however, in equinox 2021 the winds are poleward throughout the local time. Thermospheric zonal winds have relatively consistent variation. They are mainly westward (negative) during daytime regardless of season or longitudes. During night-time the zonal winds are eastward in winter and equinox months. However, the zonal winds in the night-time are weakly eastward and even turned westward during post-midnight hours. Zonal winds are much stronger than meridional winds. With increasing solar flux the meridional winds are found to more poleward (more positive).

The F-region plasma drifts obtained from the Ion Velocity Meter (IVM) onboard ICON are analysed to determine the seasonal variation of the vertical and zonal plasma drifts over the dip equator (5°N-5°S) for solar minimum years 2020 and 2021. The daytime drifts are upward (positive) irrespective of season and longitudes. The vertical drifts during night-time are showing seasonal as well as longitudinal variations. During summer, the night-time drifts are upward however, in winter they are downward (negative). In equinox of 2021, the vertical drifts are downward during night-time. In fall equinox of 2020, upward vertical drifts are observed in all longitudes from 22:00 LST to 01:00 LST whereas in fall equinox of 2021 the drifts are downward. The zonal drifts and zonal winds behave in a similar way. They are westward (negative) during daytime regardless of season and longitudes. From 19:00 LST to 23:00 LST eastward (positive) drifts are observed in all seasons. In summer, these eastward drifts are weaker compared to other seasons. Moreover during summer 2020, in certain longitude bands (0°E-40°E and 330°E-360°E) zonal drifts are westward throughout. Westward drifts during daytime are stronger than the night-time eastward drifts.

The equatorward or weakly poleward winds and upward drifts observed during night-time in summer may contribute to the large occurrence rate of the post-midnight F-region irregularities given that the PO of these irregularities maximises during June solstice (boreal summer) of solar minimum years. The eastward zonal winds weakens and even turned westward in the post-midnight hours in summer. However the impact of zonal winds on the post-midnight F-region irregularities needs to be studied further.

From this study, we can summarise that the lower atmospheric forcing through tides (SW2) can induce vertical F-region plasma drifts during the midnight hours. The uplift of the F layer during midnight hours can lead to the post-midnight F-region irregularities. Moreover, the equatorward or weakly poleward meridional winds over northern low geomagnetic latitudes can be a favourable condition for uplifting the F layer during night-time in boreal summer of solar minimum years. Other factors like seeding mechanisms have to be investigated further to explain the day to day variability in the occurrence of these irregularities.

9.2 Scope for future work

The ionosphere is a complex system which is an interface between the outer space and the lower neutral atmosphere. The dynamics and variations in the ionosphere are still difficult to predict. In this thesis, the impact of the atmospheric tides on the F-region irregularities is investigated. The lower atmospheric processes such as the Sudden Stratospheric Warming events are also observed to have a major impact on the generation of the post-midnight F-region irregularities. Moreover, the background thermospheric winds also need to be favourable for the growth of theses irregularities.

The vertical coupling between the lower atmosphere and ionosphere requires further experimental measurements from ground based remote sensing techniques as well as space born instruments. Detailed investigations are required on how the tidal interactions can alter the electrodynamics of the ionosphere.

Additionally, there is a need to address the day to day variability in the occurrence of the F-region irregularities. It is necessary to look into the seeding from atmosphere gravity waves, MSTIDs...etc. Even in the middle and high latitudes, the F-region irregularities are generated. The possible underlying mechanisms can be studied. The F-region irregularities can be freshly generated during post-midnight hours or can be drifting type. Methods need to be developed to clearly distinguish between them. So far we have analysed the occurrence of the F-region irregularities during quiet conditions. The occurrence of the F-region irregularities during geo-magnetic disturbances needs to be investigated.

To understand the upward propagating and in-situ generated tides in the upper atmosphere, a thorough investigation of the thermospheric tides from the ICON-MIGHTI winds observations is necessary.

Simulations and modelling studies can be conducted for determining the background conditions for the generation of post-midnight F-region irregularities.

The electric field measurements are required to ascertain the semi-diurnal tidal impact on it and to look into how it contributes to the formation of the post-midnight F-region irregularities.

The future twin aeronomy satellite mission called, Disturbed and quiet time Ionosphere-Thermosphere System at High Altitude (DISHA) of ISRO will give opportunities to study the ionosphere as well as the space weather. DISHA-H satellite will be placed at an 85-degree high inclination from the Earth's equator and DISHA-L will be placed at 25-degree low inclination at an altitude of 400 km. DISHA is meant to study the physics as well as the chemistry of the upper atmosphere. It will have more latitudinal coverage hence the irregularities over the high latitude can be studied as well. Using the electron density measurements by the Electron Temperature Analyser (ETA) onboard DISHA, the irregularities can be identified and the corresponding drift measurement from Ion Drift Meter (IDM) will give an insight into the background plasma conditions required to generate these irregularities. In order to identify the prevailing tidal mode and whether there are seasonal variations as well, the tidal influence on the vertical and zonal drifts can also be investigated.

References

Abdu, M. (2001). Outstanding problems in the equatorial ionosphere–thermosphere electrodynamics relevant to spread F. Journal of Atmospheric and Solar-Terrestrial Physics, 63(9), 869–884

Abdu, M. (2005). Equatorial ionosphere–thermosphere system: Electrodynamics and irregularities. Advances in Space Research, 35(5), 771–787

Abdu, M. (2012). Equatorial spread F/plasma bubble irregularities under storm time disturbance electric fields. Journal of Atmospheric and Solar-Terrestrial Physics, 75, 44–56

Abdu, M., Batista, I., & Bittencourt, J. (1981). Some characteristics of spread F at the magnetic equatorial station Fortaleza. Journal of Geophysical Research: Space Physics, 86(A8), 6836–6842

Abdu, M., De Medeiros, R., & Sobral, J. (1982). Equatorial spread F instability conditions as determined from ionograms. Geophysical Research Letters, 9(6), 692–695

Ajith, K. K., Tulasi Ram, S., Yamamoto, M., Otsuka, Y., & Niranjan, K. (2016). On the fresh development of equatorial plasma bubbles around the midnight hours of June solstice. Journal of Geophysical Research: Space Physics, 121(9), 9051-9062

Akmaev, R. A., Wu, F., Fuller-Rowell, T. J., Wang, H., & Iredell, M. D. (2010). Midnight density and temperature maxima, and thermospheric dynamics in Whole Atmosphere Model simulations. Journal of Geophysical Research: Space Physics, 115(A8)

Akmaev, R., Fuller-Rowell, T., Wu, F., Forbes, J., Zhang, X., Anghel, A., et al. (2008). Tidal variability in the lower thermosphere: Comparison of Whole Atmosphere Model (WAM) simulations with observations from TIMED. Geophysical Research Letters, 35(3).

Baker, W., & Martyn, D. (1952). Conductivity of the ionosphere. Nature, 170(4339), 1090–1092

Baker, W., & Martyn, D. F. (1953). Electric currents in the ionosphere-the conductivity. Philosophical Transactions of the Royal Society of London. Series A, Mathematical and Physical Sciences, 246(913), 281–294

Baldwin, M. (2003). Major stratospheric warming in the Southern Hemisphere in 2002: Dynamical aspects of the ozone hole split. SPARC Newsletter, 20, 24–26.

Baldwin, M. (2020). The Arctic Polar Vortex and Its Impacts. In 100th American Meteorological Society Annual Meeting. AMS

References

Baldwin, M. P., Ayarzagüena, B., Birner, T., Butchart, N., Butler, A. H., Charlton-Perez, A. J., et al. (2021). Sudden stratospheric warmings. Reviews of Geophysics, 59(1), e2020RG000708.

Bancala, S., Krüger, K., & Giorgetta, M. (2012). The preconditioning of major sudden stratospheric warmings. Journal of Geophysical Research: Atmospheres, 117(D4)

Barriopedro, D., & Calvo, N. (2014). On the relationship between ENSO, stratospheric sudden warmings, and blocking. Journal of Climate, 27(12), 4704–4720

Bates, D. R. (1982). Applied Atomic Collision Physics: Atmospheric physics and chemistry (Vol. 1). Academic Press

Bittencourt, J., & Abdu, M. (1981). A theoretical comparison between apparent and real vertical ionization drift velocities in the equatorial F-region. Journal of Geophysical Research: Space Physics, 86(A4), 2451–2454

Booker, H. G., & Wells, H. W. (1938). Scattering of radio waves by the F-region of the ionosphere. Terrestrial Magnetism and Atmospheric Electricity, 43(3), 249-256

Brum, C. G. M., Tepley, C. A., Fentzke, J. T., Robles, E., dos Santos, P. T., & Gonzalez, S. A. (2012). Long-term changes in the thermospheric neutral winds over Arecibo: Climatology based on over three decades of Fabry-Perot observations. Journal of Geophysical Research: Space Physics, 117(A2)

Buonsanto, M., & Witasse, O. (1999). An updated climatology of thermospheric neutral winds and F-region ion drifts above Millstone Hill. Journal of Geophysical Research: Space Physics, 104(A11), 24675–24687.

Buonsanto, M., Starks, M., Titheridge, J., Richards, P., & Miller, K. (1997). Comparison of techniques for derivation of neutral meridional winds from ionospheric data. Journal of Geophysical Research: Space Physics, 102(A7), 14477–14484

Candido, C. M. N., Batista, I. S., Becker-Guedes, F., Abdu, M. A., Sobral, J. H. A., & Takahashi, H. (2011). Spread F occurrence over a southern anomaly crest location in Brazil during June solstice of solar minimum activity. Journal of Geophysical Research: Space Physics, 116(A6)

Candido, C., Shi, J., Batista, I. S., Becker-Guedes, F., Correia, E., Abdu, M. A., ... & Liu, Z. (2019, July). Postmidnight equatorial plasma irregularities on the June solstice during low solar activity–a case study. In Annales Geophysicae (Vol. 37, No. 4, pp. 657-672). Copernicus GmbH

References

Chakrabarty, D., Fejer, B., Gurubaran, S., Pant, T. K., Abdu, M., & Sekar, R. (2014). On the pre-midnight ascent of F-layer in the June solstice during the deep solar minimum in 2008 over the Indian sector. Journal of Atmospheric and Solar-Terrestrial Physics, 121, 177–187

Chapman, S. (1931). The absorption and dissociative or ionizing effect of monochromatic radiation in an atmosphere on a rotating earth. Proceedings of the Physical Society, 43(1), 26

Chapman, S. (1956). The electrical conductivity of the ionosphere: A review. Il Nuovo Cimento (1955-1965), 4(4), 1385–1412

Chau, J. L., Goncharenko, L. P., Fejer, B. G., & Liu, H.-L. (2012). Equatorial and low latitude ionospheric eCffects during sudden stratospheric warming events. Space Science Reviews, 168(1), 385–417

Chau, J., Fejer, B., & Goncharenko, L. (2009). Quiet variability of equatorial E× B drifts during a sudden stratospheric warming event. Geophysical Research Letters, 36(5)

Chen, P.-R. (1992). Two-day oscillation of the equatorial ionization anomaly. Journal of Geophysical Research: Space Physics, 97(A5), 6343–6357

Cohen, J., & Jones, J. (2011). Tropospheric precursors and stratospheric warmings. Journal of Climate, 24(24), 6562–6572

Coley, W. R., Stoneback, R. A., Heelis, R. A., & Hairston, M. R. (2014, February). Topside equatorial zonal ion velocities measured by C/NOFS during rising solar activity. In Annales Geophysicae (Vol. 32, No. 2, pp. 69-75). Copernicus GmbH

Dao, T., Otsuka, Y., Shiokawa, K., Nishioka, M., Yamamoto, M., Buhari, S. M., et al. (2017). Coordinated observations of postmidnight irregularities and thermospheric neutral winds and temperatures at low latitudes. Journal of Geophysical Research: Space Physics, 122(7), 7504–7518.

Dawkins, E. C. M., Feofilov, A., Rezac, L., Kutepov, A. A., Janches, D., Höffner, J., ... & Russell III, J. (2018). Validation of SABER v2. 0 operational temperature data with ground-based lidars in the mesosphere-lower thermosphere region (75–105 km). Journal of Geophysical Research: Atmospheres, 123(17), 9916-9934

Domeisen, D. I., Butler, A. H., Charlton-Perez, A. J., Ayarzagüena, B., Baldwin, M. P., Dunn-Sigouin, E., et al. (2020). The role of the stratosphere in subseasonal to seasonal prediction: 2. Predictability arising from stratosphere-troposphere coupling. Journal of Geophysical Research: Atmospheres, 125(2), e2019JD030923.

References

Drob, D., Emmert, J., Crowley, G., Picone, Jm., Shepherd, G., Skinner, W., et al. (2008). An empirical model of the Earth's horizontal wind fields: HWM07. Journal of Geophysical Research: Space Physics, 113(A12)

Eccles, J. V. (1998). Modeling investigation of the evening prereversal enhancement of the zonal electric field in the equatorial ionosphere. Journal of Geophysical Research: Space Physics, 103(A11), 26709–26719

Eccles, J., St. Maurice, J., & Schunk, R. (2015). Mechanisms underlying the prereversal enhancement of the vertical plasma drift in the low-latitude ionosphere. Journal of Geophysical Research: Space Physics, 120(6), 4950–4970

Englert, C. R., Harlander, J. M., Brown, C. M., Marr, K. D., Miller, I. J., Stump, J. E., ... & Immel, T. J. (2017). Michelson interferometer for global high-resolution thermospheric imaging (MIGHTI): instrument design and calibration. Space science reviews, 212(1), 553-584

Farley, D., Bonelli, E., Fejer, B. G., & Larsen, M. (1986). The prereversal enhancement of the zonal electric field in the equatorial ionosphere. Journal of Geophysical Research: Space Physics, 91(A12), 13723–13728

Fejer, B. G. (1993). F-region plasma drifts over Arecibo: Solar cycle, seasonal, and magnetic activity effects. Journal of Geophysical Research: Space Physics, 98(A8), 13645–13652

Fejer, B. G., & Kelley, M. (1980). Ionospheric irregularities. Reviews of Geophysics, 18(2), 401–454

Fejer, B., Olson, M., Chau, J., Stolle, C., Lühr, H., Goncharenko, L., et al. (2010). Lunar-dependent equatorial ionospheric electrodynamic effects during sudden stratospheric warmings. Journal of Geophysical Research: Space Physics, 115(A8)

Fejer, J. (1953). Semidiurnal currents and electron drifts in the ionosphere. Journal of Atmospheric and Terrestrial Physics, 4(4), 184–203

Fesen, C. (1996). Simulations of the low-latitude midnight temperature maximum. Journal of Geophysical Research: Space Physics, 101(A12), 26863–26874

Fisher, D. J., Makela, J. J., Meriwether, J. W., Buriti, R. A., Benkhaldoun, Z., Kaab, M., & Lagheryeb, A. (2015). Climatologies of nighttime thermospheric winds and temperaturesfrom Fabry-Perot interferometer measurements: From solar minimum to solar maximum.Journal of Geophysical Research: Space Physics, 120(8), 6679–6693

References

Forbes, J. M. (1981). The equatorial electrojet. Reviews of Geophysics, 19(3), 469–504

Forbes, J. M. (1982a). Atmospheric tide: 2. The solar and lunar semidiurnal components. Journal of Geophysical Research: Space Physics, 87(A7), 5241–5252

Forbes, J. M. (1982b). Atmospheric tides: 1. Model description and results for the solar diurnal component. Journal of Geophysical Research: Space Physics, 87(A7), 5222–5240

Forbes, J. M., & Wu, D. (2006). Solar tides as revealed by measurements of mesosphere temperature by the MLS experiment on UARS. Journal of the Atmospheric Sciences, 63(7), 1776–1797

Fukao, S., Hashiguchi, H., Yamamoto, M., Tsuda, T., Nakamura, T., Yamamoto, M. K., ... & Yabugaki, Y. (2003). Equatorial Atmosphere Radar (EAR): System description and first results. Radio Science, 38(3)

Goncharenko, L. P., Harvey, V. L., Greer, K. R., Zhang, S.-R., Coster, A. J., & Paxton, L. J. (2021). Impact of September 2019 Antarctic sudden stratospheric warming on mid-latitude ionosphere and thermosphere over North America and Europe. Geophysical Research Letters, 48, e2021GL094517. https://doi.org/10.1029/2021GL094517

Goncharenko, L., & Zhang, S.-R. (2008). Ionospheric signatures of sudden stratospheric warming: Ion temperature at middle latitude. Geophysical Research Letters, 35(21)

Guozhu, Li., Ning, B., Liu, L., Wan, W., Hu, L., Zhao, B., & Patra, A. (2012). Equinoctial and June solstitial F-region irregularities over Sanya. 94.20. Dj; 94.20. Vv

Haerendel, G., Eccles, J., & Cakir, S. (1992). Theory for modeling the equatorial evening ionosphere and the origin of the shear in the horizontal plasma flow. Journal of Geophysical Research: Space Physics, 97(A2), 1209–1223

Hagan, M. (1996). Comparative effects of migrating solar sources on tidal signatures in the middle and upper atmosphere. Journal of Geophysical Research: Atmospheres, 101(D16), 21213–21222.

Hagan, M., & Forbes, J. M. (2003). Migrating and nonmigrating semidiurnal tides in the upper atmosphere excited by tropospheric latent heat release. Journal of Geophysical Research: Space Physics, 108(A2)

Hagan, M., Maute, A., & Roble, R. (2009). Tropospheric tidal effects on the middle and upper atmosphere. Journal of Geophysical Research: Space Physics, 114(A1)

Hagan, M., Maute, A., Roble, R., Richmond, A., Immel, T., & England, S. (2007). Connections between deep tropical clouds and the Earth's ionosphere. Geophysical Research Letters, 34(20)

Hamilton, K. (1981). Latent heat release as a possible forcing mechanism for atmospheric tides. Monthly Weather Review, 109(1), 3–17

Harding, B. J., Makela, J. J., Englert, C. R., Marr, K. D., Harlander, J. M., England, S. L., & Immel, T. J. (2017). The MIGHTI wind retrieval algorithm: Description and verification. Space Science Reviews, 212(1), 585-600

Hargreaves, J. K. (1992). The solar-terrestrial environment: an introduction to geospace-the science of the terrestrial upper atmosphere, ionosphere, and magnetosphere. Cambridge university press

Heelis, R. (2004). Electrodynamics in the low and middle latitude ionosphere: A tutorial. Journal of Atmospheric and Solar-Terrestrial Physics, 66(10), 825–838

Heelis, R. A., Stoneback, R. A., Perdue, M. D., Depew, M. D., Morgan, W. A., Mankey, M. W., ... & Holt, B. J. (2017). Ion velocity measurements for the ionospheric connections explorer. Space Science Reviews, 212(1), 615-629

Heelis, R., Kendall, P., Moffett, R., Windle, D., & Rishbeth, H. (1974). Electrical coupling of the E-and F-regions and its effect on F-region drifts and winds. Planetary and Space Science, 22(5), 743–756

Herrero, F. A., & Spencer, N. W. (1982). On the horizontal distribution of the equatorial thermospheric midnight temperature maximum and its seasonal variation. Geophysical Research Letters, 9(10), 1179-1182

Hirono, M. (1952). A theory of diurnal magnetic variations in equatorial regions and conductivity of the ionosphere E-region. Journal of Geomagnetism and Geoelectricity, 4(1), 7–21

Huang, C. S., & Kelley, M. C. (1996). Nonlinear evolution of equatorial spread F: 1. On the role of plasma instabilities and spatial resonance associated with gravity wave seeding. Journal of Geophysical Research: Space Physics, 101(A1), 283-292

Huba, J., & Krall, J. (2013). Impact of meridional winds on equatorial spread F: Revisited. Geophysical Research Letters, 40(7), 1268–1272

References

Huba, J., Joyce, G., Krall, J., Siefring, C., & Bernhardt, P. (2010). Self-consistent modeling of equatorial dawn density depletions with SAMI3. Geophysical Research Letters, 37(3)

Immel, T. J., England, S., Mende, S., Heelis, R., Englert, C., Edelstein, J., et al. (2018). The ionospheric connection explorer mission: Mission goals and design. Space Science Reviews, 214(1), 1–36

Immel, T., Sagawa, E., England, S., Henderson, S., Hagan, M., Mende, S., et al. (2006). Control of equatorial ionospheric morphology by atmospheric tides. Geophysical Research Letters, 33(15)

Jones Jr, M., Forbes, J. M., Hagan, M. E., & Maute, A. (2013). Non-migrating tides in the ionosphere-thermosphere: In situ versus tropospheric sources. Journal of Geophysical Research: Space Physics, 118(5), 2438-2451

Kalnay, E., Kanamitsu, M., Kistler, R., Collins, W., Deaven, D., Gandin, L., ... & Joseph, D. (1996). The NCEP/NCAR 40-year reanalysis project. Bulletin of the American meteorological Society, 77(3), 437-472

KATO, S. (1956). Horizontal Wind Systems in the ionospheric E-region Deduced from the Dynamo Theory of the Geomagnetic Sq variation Part II. Rotating Earth. Journal of Geomagnetism and Geoelectricity, 8(1), 24–37

Kelley, M.C. (1989) The Earth's Ionosphere, Plasma Physics and Electrodynamics. Academic Press, Inc., San Diego, California

Kelley, M. (2009). E-region dynamo theory and the daytime equatorial electrojet. The Earth's Ionosphere, 89–99

Kil, H., Oh, S.-J., Kelley, M., Paxton, L., England, S., Talaat, E., et al. (2007). Longitudinal structure of the vertical E$\times$ B drift and ion density seen from ROCSAT-1. Geophysical Research Letters, 34(14)

Krall, J., Huba, J., Joyce, G., & Zalesak, S. (2009). Three-dimensional simulation of equatorial spread-F with meridional wind effects. In Annales Geophysicae (Vol. 27, pp. 1821–1830). Copernicus GmbH

Kudeki, E., Akgiray, A., Milla, M., Chau, J. L., & Hysell, D. L. (2007). Equatorial spread-F initiation: Post-sunset vortex, thermospheric winds, gravity waves. Journal of Atmospheric and Solar-Terrestrial Physics, 69(17–18), 2416–2427

References

L'Heureux, M. (2021). On the Sudden Stratospheric Warming and Polar Vortex of Early 2021. NOAA Climate. Gov, January, 28

Labitzke, K. (1981). Stratospheric-mesospheric midwinter disturbances: A summary of observed characteristics. Journal of Geophysical Research: Oceans, 86(C10), 9665–9678

Laštovička, J. (2006). Forcing of the ionosphere by waves from below. Journal of Atmospheric and Solar-Terrestrial Physics, 68(3–5), 479–497

Li, G., Ning, B., Abdu, M. A., Yue, X., Liu, L., Wan, W., and Hu, L. (2011), On the occurrence of postmidnight equatorial F-region irregularities during the June solstice, J. Geophys. Res., 116, A04318, doi:10.1029/2010JA016056

Lim, E.-P., Hendon, H. H., Boschat, G., Hudson, D., Thompson, D. W., Dowdy, A. J., & Arblaster, J. M. (2019). Australian hot and dry extremes induced by weakenings of the stratospheric polar vortex. Nature Geoscience, 12(11), 896–901.

Lindzen, R. S. (1978). Effect of daily variations of cumulonimbus activity on the atmospheric semidiurnal tide. Monthly Weather Review, 106(4), 526–533

Link, R., & Cogger, L. L. (1988). A reexamination of the OI 6300-Å nightglow. Journal of Geophysical Research: Space Physics, 93(A9), 9883-9892

Liu, A. Z., Guo, Y., Vargas, F., & Swenson, G. R. (2016). First measurement of horizontal wind and temperature in the lower thermosphere (105–140 km) with a Na Lidar at Andes Lidar Observatory. Geophysical Research Letters, 43(6), 2374–2380

Liu, G., Huang, W., Shen, H., Aa, E., Li, M., Liu, S., & Luo, B. (2019). Ionospheric response to the 2018 sudden stratospheric warming event at middle-and low-latitude stations over China sector. Space Weather, 17(8), 1230–1240

Liu, H., Lühr, H., Watanabe, S., Köhler, W., Henize, V., and Visser, P. (2006), Zonal winds in the equatorial upper thermosphere: Decomposing the solar flux, geomagnetic activity, and seasonal dependencies, J. Geophys. Res., 111, A07307, doi:10.1029/2005JA011415

Liu, H.-L., Wang, W., Richmond, A., & Roble, R. (2010). Ionospheric variability due to planetary waves and tides for solar minimum conditions. Journal of Geophysical Research: Space Physics, 115(A6)

Lu, Q., Rao, J., Liang, Z., Guo, D., Luo, J., Liu, S., et al. (2021). The sudden stratospheric warming in January 2021. Environmental Research Letters, 16(8), 084029

References

Ma, T.-Z., & Schunk, R. (1995). Effect of polar cap patches on the polar thermosphere. Journal of Geophysical Research: Space Physics, 100(A10), 19701–19713

Maeda, H. (1955). Horizontal Wind Systems in the Ionospheric E-region Deduced from the Dynamo Theory of the Geomagnetic Sq Variation Part I. Non-rotating Earth. Journal of Geomagnetism and Geoelectricity, 7(4), 121–132

Makela, J. J., Baughman, M., Navarro, L. A., Harding, B. J., Englert, C. R., Harlander, J. M., et al. (2021). Validation of ICON-MIGHTI thermospheric wind observations: 1. Nighttime red-line ground-based fabry-perot interferometers. Journal of Geophysical Research: Space Physics, 126(2), e2020JA028726

Makela, J. J., Navarro, L., Harding, B. J., Englert, C. R., & Immel, T. J. (2020, December). Traveling Atmospheric Disturbances in the Midlatitude Thermosphere: Coordinated Ground-and Space-Based Observations. In AGU Fall Meeting Abstracts (Vol. 2020, pp. SA003-04)

Maruyama, T. (1996). Modeling study of equatorial ionospheric height and spread F occurrence. Journal of Geophysical Research: Space Physics, 101(A3), 5157-5163

Maruyama, T., Kawamura, M., Saito, S., Nozaki, K., Kato, H., Hemmakorn, N., et al. (2007). Low latitude ionosphere-thermosphere dynamics studies with inosonde chain in Southeast Asia. In Annales Geophysicae (Vol. 25, pp. 1569–1577). Copernicus GmbH

Maruyama, T., Saito, S., Kawamura, M., Nozaki, K., Krall, J., & Huba, J. (2009). Equinoctial asymmetry of a low-latitude ionosphere-thermosphere system and equatorial irregularities: evidence for meridional wind control. In Annales geophysicae (Vol. 27, pp. 2027–2034). Copernicus GmbH

McInturff, R. M. (1978). Stratospheric warmings: Synoptic, dynamic and general-circulation aspects

Miller, E. S., Makela, J. J., & Kelley, M. C. (2009). Seeding of equatorial plasma depletions by polarization electric fields from middle latitudes: Experimental evidence. Geophysical Research Letters, 36(18)

Miller, K., Torr, D., & Richards, P. (1986). Meridional winds in the thermosphere derived from measurement of F 2 layer height. Journal of Geophysical Research: Space Physics, 91(A4), 4531–4535

References

Millward, G., Müller-Wodarg, I., Aylward, A., Fuller-Rowell, T., Richmond, A., & Moffett, R. (2001). An investigation into the influence of tidal forcing on F-region equatorial vertical ion drift using a global ionosphere-thermosphere model with coupled electrodynamics. Journal of Geophysical Research: Space Physics, 106(A11), 24733–24744

Miyahara, S., & Miyoshi, Y. (1997). Migrating and non-migrating atmospheric tides simulated by a middle atmosphere general circulation model. Advances in Space Research, 20(6), 1201–1207

Narayanan, V., Patra, A., Gurubaran, S., Pavan Chaitanya, P., & Emperumal, K. (2019). Coincident airglow, VHF radar, and ionosonde observations of electrified medium-scale traveling ionospheric disturbances in the equatorial latitudes. Geophysical Research Letters, 46(13), 7173–7181

Nicolls, M., Kelley, M., Vlasov, M., Sahai, Y., Chau, J., Hysell, D., et al. (2006). Observations and modeling of post-midnight uplifts near the magnetic equator. In Annales geophysicae (Vol. 24, pp. 1317–1331). Copernicus GmbH

Niranjan, K., Brahmanandam, P. S., & Srivani, B. (2006). Signatures of equatorial midnight temperature maximum as observed from in situ and ground-based ionospheric measurements in the Indian sector. Journal of Geophysical Research: Space Physics, 111(A7)

Nishioka, M., Otsuka, Y., Shiokawa, K., Tsugawa, T., Supnithi, P., Nagatsuma, T., & Murata, K. (2012). On post-midnight field-aligned irregularities observed with a 30.8-MHz radar at a low latitude: Comparison withF-layer altitude near the geomagnetic equator. Journal of Geophysical Research: Space Physics, 117(A8)

Oberheide, J., Hagan, M., Roble, R., & Offermann, D. (2002). Sources of nonmigrating tides in the tropical middle atmosphere. Journal of Geophysical Research: Atmospheres, 107(D21), ACL-6

Otsuka, Y. (2018). Review of the generation mechanisms of post-midnight irregularities in the equatorial and low-latitude ionosphere. Progress in Earth and Planetary Science, 5(1), 1–13

Otsuka, Y., & Ogawa, T. (2009). VHF radar observations of nighttime F-region field-aligned irregularities over Kototabang, Indonesia. Earth, planets and space, 61(4), 431-437

Otsuka, Y., Shiokawa, K., & Nishioka, M. (2012). VHF radar observations of post-midnight F-region field-aligned irregularities over Indonesia during solar minimum. 94.20. dj; 94.20. Vv; 96.60. qd

Otsuka, Y., Shiokawa, K., Ogawa, T., & Wilkinson, P. (2004). Geomagnetic conjugate observations of medium-scale traveling ionospheric disturbances at midlatitude using all-sky airglow imagers. Geophysical research letters, 31(15)

Pancheva, D., & Mukhtarov, P. (2011). Stratospheric warmings: The atmosphere–ionosphere coupling paradigm. Journal of Atmospheric and Solar-Terrestrial Physics, 73(13), 1697–1702

Pancheva, D., & Mukhtarov, P. (2012). Global response of the ionosphere to atmospheric tides forced from below: Recent progress based on satellite measurements. Space Science Reviews, 168(1), 175–209

Pancheva, D., Mukhtarov, P., & Andonov, B. (2010). Global structure, seasonal and interannual variability of the eastward propagating tides seen in the SABER/TIMED temperatures (2002–2007). Advances in Space Research, 46(3), 257–274

Patra, A. K., Phanikumar, D. V., & Pant, T. K. (2009). Gadanki radar observations of F-region field-aligned irregularities during June solstice of solar minimum: First results and preliminary analysis. Journal of Geophysical Research: Space Physics, 114(A12). https://doi.org/10.1029/2009JA014437

Patra, A., Pavan Chaitanya, P., Sripathi, S., & Alex, S. (2014). Ionospheric variability over Indian low latitude linked with the 2009 sudden stratospheric warming. Journal of Geophysical Research: Space Physics, 119(5), 4044–4061

Pedatella, N., Liu, H.-L., Richmond, A., Maute, A., & Fang, T.-W. (2012). Simulations of solar and lunar tidal variability in the mesosphere and lower thermosphere during sudden stratosphere warmings and their influence on the low-latitude ionosphere. Journal of Geophysical Research: Space Physics, 117(A8)

Picone, J., Hedin, A., Drob, D. P., & Aikin, A. (2002). NRLMSISE-00 empirical model of the atmosphere: Statistical comparisons and scientific issues. Journal of Geophysical Research: Space Physics, 107(A12), SIA-15

Rao, J., Garfinkel, C. I., White, I. P., & Schwartz, C. (2020). The Southern Hemisphere minor sudden stratospheric warming in September 2019 and its predictions in S2S models. Journal of Geophysical Research: Atmospheres, 125(14), e2020JD032723

Rao, J., Ren, R., Chen, H., Liu, X., Yu, Y., Hu, J., & Zhou, Y. (2019). Predictability of stratospheric sudden warmings in the Beijing Climate Center forecast system with statistical error corrections. Journal of Geophysical Research: Atmospheres, 124(15), 8385–8400

References

Reddy, C. A. (1991). Equatorial Middle Atmosphere. Journal of geomagnetism and geoelectricity, 43(Supplement2), 695-708

Reinisch, B. (1996). Ionosonde, Upper Atmosphere edited by W. Dieminger, GK Hartmann, R. Leitinger. Springer

Reinisch, B. W., & Xueqin, H. (1983). Automatic calculation of electron density profiles from digital ionograms: 3. Processing of bottomside ionograms. Radio Science, 18(3), 477-492

Reinisch, B., Huang, X., Galkin, I., Paznukhov, V., & Kozlov, A. (2005). Recent advances in real-time analysis of ionograms and ionospheric drift measurements with digisondes. Journal of Atmospheric and Solar-Terrestrial Physics, 67(12), 1054–1062

Richmond, A. D. (1983). Thermospheric dynamics and electrodynamics. In Solar-terrestrial physics (pp. 523–607). Springer

Richmond, A., Lathuillere, C., & Vennerstrøm, S. (2003). Winds in the high-latitude lower thermosphere: Dependence on the interplanetary magnetic field. Journal of Geophysical Research: Space Physics, 108(A2)

Richmond, A., Matsushita, S., & Tarpley, J. (1976). On the production mechanism of electric currents and fields in the ionosphere. Journal of Geophysical Research, 81(4), 547–555

Richmond, A., Ridley, E., & Roble, R. (1992). A thermosphere/ionosphere general circulation model with coupled electrodynamics. Geophysical Research Letters, 19(6), 601–604

Rishbeth, H. (1971a). The F-layer dynamo. Planetary and Space Science, 19(2), 263–267

Rishbeth, H. (1971b). Polarization fields produced by winds in the equatorial F-region. Planetary and Space Science, 19(3), 357–369

Rishbeth, H. (1972). Thermospheric winds and the F-region: A review. Journal of Atmospheric and Terrestrial Physics, 34(1), 1–47

Rishbeth, H. (1981). The F-region dynamo. Journal of Atmospheric and Terrestrial Physics, 43(5–6), 387–392

Rishbeth, H. (2002). Ionosphere: High above the Earth. Nature, 418(6893), 23–23

Rishbeth, H. (2006), F-region links with the lower atmosphere? J. Atmos. Sol. Terr. Phys., **68**, 469– 478, doi:10.1016/j.jastp.2005.03.017

Rishbeth, H., & Garriott, O. K. (1969). Introduction to ionospheric physics. Introduction to Ionospheric Physics

Rishbeth, H., & Mendillo, M. (2001). Patterns of F2-layer variability. Journal of Atmospheric and Solar-Terrestrial Physics, 63(15), 1661–1680

Russell III, M., MG, G., & LL, T. (n.d.). J., & Esplin, R.(1999). An overview of the SABER experiment and preliminary calibration results. In SPIE Conference on Optical Spectroscopic Techniques and Instrumentation for Atmospheric and Space Research III (Vol. 3756)

Saito, S., & Maruyama, T. (2006). Ionospheric height variations observed by ionosondes along magnetic meridian and plasma bubble onsets. In Annales Geophysicae (Vol. 24, pp. 2991–2996). Copernicus GmbH

Sasi, M. N., Ramkumar, G., & Deepa, V. (2001, August). Tidal wind oscillations in the tropical lower atmosphere as observed by Indian MST Radar. In Annales Geophysicae (Vol. 19, No. 8, pp. 991-999). Copernicus GmbH

Sastri, J. H. (1999). Letter to the editor Post-midnight onset of spread-F at Kodaikanal during the June solstice of solar minimum. In Annales Geophysicae (Vol. 17, pp. 1111–1115). Springer

Shen, X., Wang, L., & Osprey, S. (2020). The Southern Hemisphere sudden stratospheric warming of September 2019. Science Bulletin, 65(21)

Shepherd, G. G., Thuillier, G., Gault, W., Solheim, B., Hersom, C., Alunni, J., et al. (1993). WINDII, the wind imaging interferometer on the upper atmosphere research satellite. Journal of Geophysical Research: Atmospheres, 98(D6), 10725–10750

Shiokawa, K., Otsuka, Y., & Ogawa, T. (2006). Quasiperiodic southward moving waves in 630-nm airglow images in the equatorial thermosphere. Journal of Geophysical Research: Space Physics, 111(A6)

Shiokawa, K., Ihara, C., Otsuka, Y., and Ogawa, T. (2003), Statistical study of nighttime medium-scale traveling ionospheric disturbances using midlatitude airglow images, J. Geophys. Res., 108, 1052, doi:10.1029/2002JA009491, A1

Sibanda, P. (2006). Particle Precipitation Effects on the South African Ionosphere (PhD Thesis). Rhodes University

Siebert, M. (1961). Atmospheric tides. In Advances in geophysics (Vol. 7, pp. 105–187). Elsevier

References

Smith, A. K. (2012). Global dynamics of the MLT. Surveys in Geophysics, 33(6), 1177–1230

Sobral, J., Abdu, M., Zamlutti, C., & Batista, I. (1980). Association between plasma bubble irregularities and airglow disturbances over Brazilian low latitudes. Geophysical Research Letters, 7(11), 980–982

Spencer, N., Wharton, L., Carignan, G., & Maurer, J. (1982). Thermosphere zonal winds, vertical motions and temperature as measured from Dynamics Explorer. Geophysical Research Letters, 9(9), 953–956

Sridharan, S. (2017). Variabilities of low-latitude migrating and nonmigrating tides in GPS-TEC and TIMED-SABER temperature during the sudden stratospheric warming event of 2013. Journal of Geophysical Research: Space Physics, 122(10), 10–748

Sridharan, S. (2019). Seasonal variations of low-latitude migrating and non migrating diurnal and semidiurnal tides in TIMED-SABER temperature and their relationship with source variations. Journal of Geophysical Research: Space Physics, 124(5), 3558–3572

Sridharan, S., Sathishkumar, S., & Gurubaran, S. (2009). Variabilities of mesospheric tides and equatorial electrojet strength during major stratospheric warming events. In Annales Geophysicae (Vol. 27, pp. 4125–4130). Copernicus GmbH

Sridharan, S., Sathishkumar, S., & Gurubaran, S. (2012). Variabilities of mesospheric tides during sudden stratospheric warming events of 2006 and 2009 and their relationship with ozone and water vapour. Journal of Atmospheric and Solar-Terrestrial Physics, 78, 108–115

Sripathi, S., Bose, S., Patra, A., Pant, T., Kakad, B., & Bhattacharyya, A. (2008). Simultaneous observations of ESF irregularities over Indian region using radar and GPS. In Annales geophysicae (Vol. 26, pp. 3197–3213). Copernicus GmbH

Stoneback, R., Heelis, R., Burrell, A., Coley, W., Fejer, B., & Pacheco, E. (2011). Observations of quiet time vertical ion drift in the equatorial ionosphere during the solar minimum period of 2009. Journal of Geophysical Research: Space Physics, 116(A12)

Subbarao, K., & Murthy, B. K. (1994). Post-sunset F-region vertical velocity variations at magnetic equator. Journal of Atmospheric and Terrestrial Physics, 56(1), 59–65

Takahashi, H., Wrasse, C. M., Figueiredo, C. A. O. B., Barros, D., Abdu, M. A., Otsuka, Y., & Shiokawa, K. (2018). Equatorial plasma bubble seeding by MSTIDs in the ionosphere. Progress in Earth and Planetary Science, 5(1), 1-13

References

Tesema, F. (2010). Night Time Spread F and Associated GPS L-band

Thompson, D. W., Baldwin, M. P., & Solomon, S. (2005). Stratosphere–troposphere coupling in the Southern Hemisphere. Journal of the Atmospheric Sciences, 62(3), 708–715

Torrence, C., & Compo, G. P. (1998). A practical guide to wavelet analysis. Bulletin of the American Meteorological Society, 79(1), 61–78

Tripathi, O. P., Charlton-Perez, A., Sigmond, M., & Vitart, F. (2015). Enhanced long-range forecast skill in boreal winter following stratospheric strong vortex conditions. Environmental Research Letters, 10(10), 104007

Truskowski, A. O., Forbes, J. M., Zhang, X., & Palo, S. E. (2014). New perspectives on thermosphere tides: 1. Lower thermosphere spectra and seasonal-latitudinal structures. Earth, Planets and Space, 66(1), 1–17

Tsunoda, R. T. (1980). Magnetic-field-aligned characteristics of plasma bubbles in the nighttime equatorial ionosphere. Journal of Atmospheric and Terrestrial Physics, 42(8), 743–752

Vincent, R., Kovalam, S., Fritts, D., & Isler, J. (1998). Long-term MF radar observations of solar tides in the low-latitude mesosphere: Interannual variability and comparisons with the GSWM. Journal of Geophysical Research: Atmospheres, 103(D8), 8667–8683

Vincent, R., Tsuda, T., & Kato, S. (1988). A comparative study of mesospheric solar tides observed at Adelaide and Kyoto. Journal of Geophysical Research: Atmospheres, 93(D1), 699–708

Vineeth, C., Pant, T., Sumod, S., Kumar, K., Gurubaran, S., & Sridharan, R. (2011). Planetary wave-tidal interactions over the equatorial mesosphere-lower thermosphere region and their possible implications for the equatorial electrojet. Journal of Geophysical Research: Space Physics, 116(A1)

Woodman, R. F., & La Hoz, C. (1976). Radar observations of F-region equatorial irregularities. Journal of Geophysical Research, 81(31), 5447–5466

Xu, H., Shiokawa, K., Oyama, S., & Nozawa, S. (2019a). High-latitude thermospheric wind study using a Fabry–Perot interferometer at Tromsø in Norway: averages and variations during quiet times. Earth, Planets and Space, 71(1), 1–8

Xu, H., Shiokawa, K., Oyama, S., & Nozawa, S. (2019b). High-latitude thermospheric wind study using a Fabry–Perot interferometer at Tromsø in Norway: averages and variations during quiet times. Earth, Planets and Space, 71(1), 1–8

References

Yamashita, K., Miyahara, S., Miyoshi, Y., Kawano, K., & Ninomiya, J. (2002). Seasonal variation of non-migrating semidiurnal tide in the polar MLT region in a general circulation model. Journal of Atmospheric and Solar-Terrestrial Physics, 64(8–11), 1083–1094

Yamazaki, Y., & Maute, A. (2017). Sq and EEJ—A review on the daily variation of the geomagnetic field caused by ionospheric dynamo currents. Space Science Reviews, 206(1), 299–405

Yizengaw, E., Retterer, J., Pacheco, E., Roddy, P., Groves, K., Caton, R., & Baki, P. (2013). Postmidnight bubbles and scintillations in the quiet-time June solstice. Geophysical Research Letters, 40(21), 5592–5597

Yu, T., Huang, C., Zhao, G., Mao, T., Wang, Y., Zeng, Z., et al. (2014). A preliminary study of thermosphere and mesosphere wind observed by Fabry-Perot over Kelan, China. Journal of Geophysical Research: Space Physics, 119(6), 4981–4997